IAEA nuclear fusion

SPECIAL TOPIC

The H-Mode of ASDEX

To cite this article: ASDEX Team 1989 *Nucl. Fusion* **29** 1959

View the article online for updates and enhancements.

Related content

- Effect of bootstrap and beam driven currents on current profile and ballooning stability in ASDEX L- and H-mode plasmas
  G. Becker
- Confinement studies in L and H-type Asdex discharges
  M Keilhacker, G Becker, K Bernhardi et al.
- Major results from the stellarator Wendelstein 7-AS
  M Hirsch, J Baldzuhn, C Beidler et al.

Recent citations

- On the possibility of limit-cycle-state of peeling mode near stability boundary in the quiescent H-mode
  Kimitaka Itoh *et al*
- Plasma performance improvement with favourable B_t relative to unfavourable B_t in RF-heated H-mode plasmas in EAST
  X. Lin *et al*
- Sandpile modelling of dual location fuelling in fusion plasmas
  C A Bowie and M J Hole

IOP ebooks™

Bringing together innovative digital publishing with leading authors from the global scientific community.

Start exploring the collection−download the first chapter of every title for free.

This content was downloaded from IP address 172.8.128.60 on 22/05/2021 at 07:08

SPECIAL TOPIC

THE H-MODE OF ASDEX

ASDEX Team
Max-Planck-Institut für Plasmaphysik,
Euratom-IPP Association,
Garching bei München,
Federal Republic of Germany

ABSTRACT. The paper is a review of investigations of the H-mode on ASDEX performed since its discovery in 1982. The topics discussed are: (1) the development of the plasma profiles, with steep gradients in the edge region and flat profiles in the bulk plasma, (2) the MHD properties resulting from the profile changes, including an extensive stability analysis, (3) the impurity development, with special emphasis on the MHD aspects and on neoclassical impurity transport effects in quiescent H-phases, and (4) the properties of the edge plasma, including the evidence of three-dimensional distortions at the edge. The part on confinement includes scaling studies and the results of transport analysis. The power threshold of the H-mode is found to depend weakly on the density, but there is probably no dependence on the toroidal field or the current. For the operational range of the H-mode, new results for the limiter H-mode on ASDEX and the development of the H-mode under beam current drive conditions are included. A number of experiments are described which demonstrate the crucial role of the edge electron temperature in the L–H transition. New results of magnetic and density fluctuation studies at the plasma edge within the edge transport barrier are presented. Finally, the findings on ASDEX are compared with results obtained on other machines and are used to test various H-mode theories.

GENERAL INTRODUCTION

The aim of fusion-oriented plasma research is the study and understanding of the behaviour of hot plasma, with the ultimate goal of providing the conditions for a burning plasma. The parameter values which have to be achieved are well known: the product of density and energy confinement time has to be 3×10^{14} cm$^{-3}\cdot$s and the average plasma temperature has to be 10 keV. The target values of these two parameters have been obtained separately; however, in experiments where the temperature was adequate, the confinement product was inadequate, and vice versa. Simultaneous achievement of the two values was found to be difficult. The use of auxiliary heating to increase the plasma temperature in a tokamak gave rise to severe degradation of the confinement, with the net result of no effective approach to break-even conditions. The operational regime of tokamak plasmas characterized by a confinement time that decreases strongly with increasing auxiliary heating power is termed the L-regime.

The energy confinement time in the present generation of large tokamaks with auxiliary heating is determined by conductive heat transport. In the edge region and in low density discharges, convective losses may prevail. Both the ion and the electron heat transport coefficients are considerably larger than those calculated on the basis of classical scattering processes. The actual heat conductivity in a tokamak plasma is dominated by the increased transport due to fluctuating electric and magnetic fields that are caused by plasma instabilities. The exploration of the mechanisms which give rise to the anomalously enhanced transport is one of the main topics of tokamak research. The lack of understanding these mechanisms makes it impossible to reach well-founded predictions of the performance of future experimental devices and is the main reason for the still existing uncertainty about the feasibility of a burning plasma.

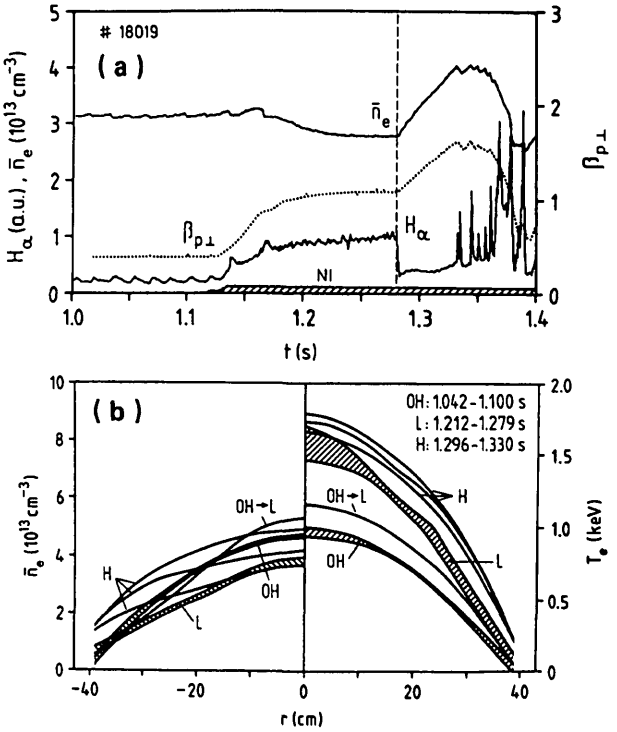

FIG. 2. (a) Electron density $\bar{n}_e$, $\beta_{p\perp}$ and H_α radiation in the divertor chamber; the L-H transition is indicated by the dashed vertical line. (b) Development of the electron temperature and density profiles from the Ohmic phase to the L- and H-phases.

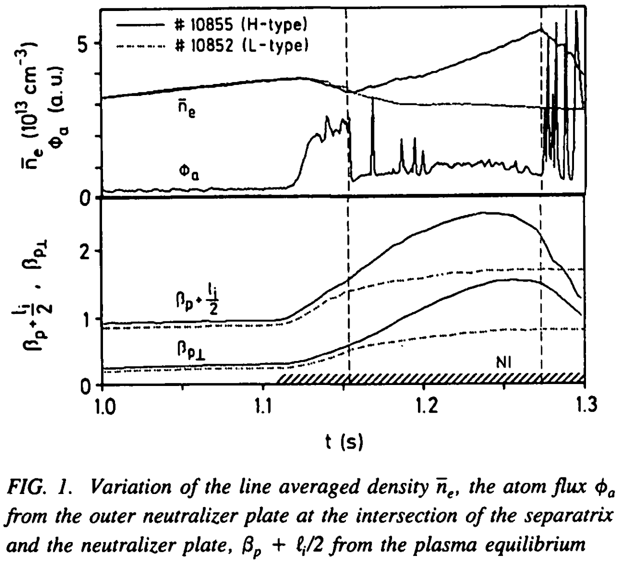

FIG. 1. Variation of the line averaged density $\bar{n}_e$, the atom flux ϕ_a from the outer neutralizer plate at the intersection of the separatrix and the neutralizer plate, $\beta_p + \ell_i/2$ from the plasma equilibrium and $\beta_{p\perp}$ from the diamagnetic signal, during a neutral injection (NI) pulse (hatched area). Compared are an H-discharge (solid lines) and an L-discharge (dotted lines). The L-H transition is indicated by the dashed vertical line. The two discharges differ only in the current, which is 300 kA in the L-discharge and 275 kA in the H-discharge.

This report deals with the investigation of a plasma confinement regime in which the severe deterioration of the confinement quality at high heating power is avoided. This regime is called the H-mode because of its high confinement characteristics, and the regime of low confinement is called the L-mode. There is evidence that the L-mode characteristics will not lead to sufficient confinement for successful plasma burning. The H-mode was observed for the first time on ASDEX. At present it is considered to be the confinement regime with the best prospects for future tokamak operation.

However, the study of both H-mode and L-mode confinement physics has increased our understanding of energy transport in tokamaks.

1. INTRODUCTION AND OVERVIEW OF THE H-MODE

The difference in energy confinement is the most important aspect of an H-mode plasma compared with an L-mode plasma [1, 2]. The improvement of the global energy confinement time is due to a reduction of the electron heat diffusivity and the particle diffusion coefficient. The different energy and particle confinement properties of L- and H-discharges are evident from the differences in the plasma beta β_p and in the line averaged density $\bar{n}_e$ during neutral injection (NI). Figure 1 compares L- and H-discharges that have the same density in the OH phase and the same heating power. Plotted are the line averaged density $\bar{n}_e$, $\beta_p + \ell_i/2$ from the plasma equilibrium, $\beta_{p\perp}$ measured diamagnetically, and the atom flux ϕ_a from the outer upper target plate located inside the divertor chamber. The atom flux is due to the impinging ions which are neutralized and reflected. Since ϕ_a is measured for particle energies of >100 eV, it only represents ions from the main plasma periphery and therefore its intensity is related to the particle confinement properties of the plasma bound by the separatrix.

Figure 2(a) shows the variation of the H_α radiation in the divertor chamber. Both ϕ_a and H_α increase during the L-phase and drop sharply at the L–H transition. The particle content of the plasma is kept constant in the Ohmic phase by a density feedback system; in an L-discharge the density decreases despite additional particle fuelling by the beams and intensified gas puffing from the outside. In an H-discharge the particle content of the plasma rises sharply without external gas feed. The improved energy confinement causes the energy content of the discharge to rise, as is obvious from both the equilibrium signal and the diamagnetic signal. The energy content of an H-mode plasma is nearly twice that of an L-mode plasma and — since the heating power is the same in the two cases — the energy confinement time in the H-mode is nearly twice as long as in the L-mode. In the divertor chamber the H_α radiation is determined by local recycling due to the ionization of the neutral gas by the divertor plasma and due to the neutralization of the divertor plasma at the target plates. The intensity of this circular process — neutralization and re-ionization — depends on the power flux into the divertor chamber. The H_α intensity in the divertor chamber is, to a large extent, a measure of the energy confinement capability of the main plasma. In particular, a change in the H_α intensity or in the atom flux indicates a variation in the energy or particle confinement properties. For example, the transition to the H-phase (dashed vertical line in Figs 1 and 2(a)) is indicated by a sudden drop in ϕ_a and in the H_α intensity.

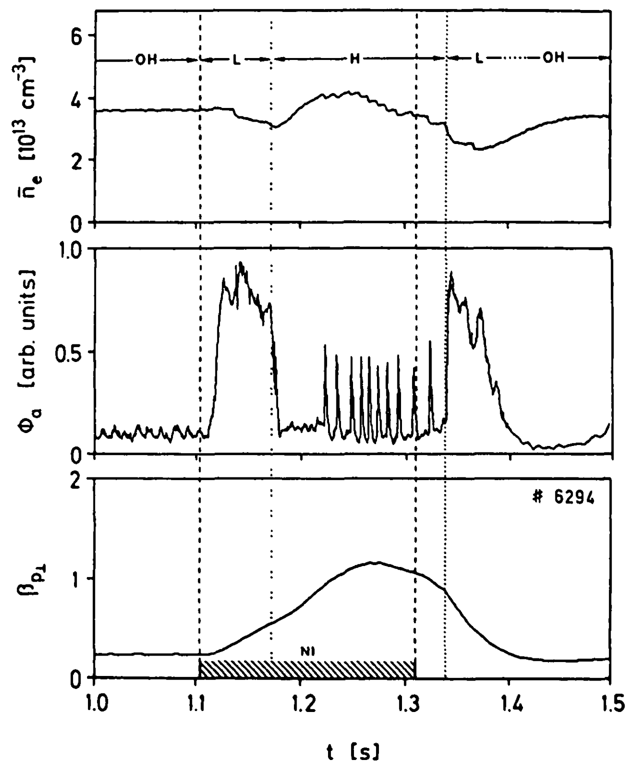

FIG. 3. Variation of the line averaged electron density $\bar{n}_e$, the atom flux ϕ_a from the outer neutralizer plate at the intersection of the separatrix and the neutralizer plate, and $\beta_{p\perp}$ from the diamagnetic loop during the NI phase (hatched area) and during the H- and L-phases.

A characteristic feature of the H-mode in ASDEX is that it develops from a preceding L-phase whose duration varies between 30 and 150 ms. A case where an Ohmic plasma directly develops to an H-mode as soon as the beams are switched on has never been observed in ASDEX. The transition from the L-phase to the H-phase can be seen in Fig. 1 and is shown in more detail in Fig. 3, where the time development of $\bar{n}_e$, β_p and ϕ_a is shown. At the L–H transition, ϕ_a drops to a value comparable to the Ohmic level. The simultaneous drop of the divertor signals (ϕ_a or H_α) and the correlated rise of the main plasma density and of β_p mark the transition to the H-phase. The transition is sharp and can happen within 2 ms, indicating the existence of distinct transition conditions. The transition occurs spontaneously, without any operational intervention from the outside. The development of an H-discharge during the beam heating phase is determined by the setting of the plasma parameters for the preceding Ohmic phase and by the level of heating power. The H-mode requires a high heating power, above a certain power threshold (see Section 4). When the beam pulse is terminated, the plasma remains in the H-phase for about 35 ms (two to three times the beam ion slowing-down time), after which time ϕ_a suddenly increases once more. In the same way as in the initial beam phase, but now during a phase with hardly any power input, a transition to a second L-mode occurs and gives rise to a discontinuity of the slopes of $\bar{n}_e$ and β_p, which thereafter decrease even faster. Apparently, in ASDEX the plasma cannot develop an H-phase from the Ohmic phase nor can it directly return to Ohmic transport properties. The plasma evolution with an H-mode during beam heating always occurs in the sequence OH–L–H–L–OH.

The plasma conditions developing in the H-phase give rise to a new type of MHD instability which repetitively modulates the H_α radiation in the divertor chamber and the atom flux ϕ_a (see Figs 1 and 3) and causes additional particle and energy losses, thereby degrading the good confinement properties of the H-phase. These fluctuations have been dubbed edge localized modes (ELMs) because they affect primarily the plasma boundary [3]. By extending the plasma major radius R_0 in ASDEX from 165 cm to 170 cm, ELMs can be avoided for 100–200 ms. These discharges are termed quiescent H-discharges (H^*). They display the transport properties intrinsic to the H-mode without additional MHD losses caused by ELMs [4–6] (see Section 3.4.3).

There are several regimes with auxiliary heating which demonstrate improved confinement. An H-mode is characterized by the properties mentioned above [5–8]. The improvement of the energy confinement time in the H-mode is substantial — a factor of two being typical. In ASDEX, H-discharges are only possible in the divertor configuration, except for a few belt limiter plasmas which show L–H transitions with minor improvements in confinement (see Section 4.3).

The H-mode was discovered on ASDEX in 1982 [1]. Since then, the inside of the ASDEX vessel was changed several times: A toroidal belt limiter was removed in 1982 after the H-mode had been discovered; low field side ICRH antennas were added in 1984; the divertor configuration was changed in 1986/87 from DV-I (large divertor volume, titanium target plates, radiation cooled) to DV-II (small divertor volume, copper target plates, water cooled); in the course of the years, more graphite was added. The configurational aspects of the divertor in the H-mode are discussed in Section 4.2.

2. CHARACTERISTICS OF H-MODE PLASMAS

2.1. Equilibrium parameters

The initiation of beam heating and the changes in confinement transiently affect the horizontal position of the centre of the flux surface which defines the separatrix, as shown in Fig. 4(b). When the beams are switched on, the sudden contribution of the beam ions to the plasma pressure causes the plasma to expand radially until the vertical magnetic field restores the pre-set radial position. Because of the improvement of β_p the horizontal plasma position Δ_{HOR} increases once more after the L–H transition. ELMs have a strong effect on the plasma equilibrium and lead to modulations in the horizontal plasma position, with a typical amplitude of a few millimetres [9]. To maintain the horizontal plasma equilibrium, the vertical field of an H-discharge is higher than that of an L-discharge; Fig. 4(a) compares the current I_{VF} in the vertical field coils of an L-discharge and of a similar H-discharge. The rise of I_{VF} with beam heating in an H-discharge is nearly twice that in an L-discharge with similar plasma and beam setting because of the two-fold increase in plasma beta.

The higher vertical field in the H-phase also affects the separatrix position in the divertor chamber and causes a shift of the location where the target plates intersect the separatrix in the direction of the main plasma by about 1 cm, which is about half the width of the energy and particle deposition profiles at the target plate.

2.2. Main plasma parameters

The dominant plasma characteristic of the H-mode seems to be the development of a transport barrier close to, but inside, the separatrix, with a radial extent which is not well determined but which is in the range of several centimetres. The particle and energy transport coefficients are decreased within this layer. This decrease also seems to reduce the cross-field transport coefficients in the scrape-off layer (SOL), whose radial extent

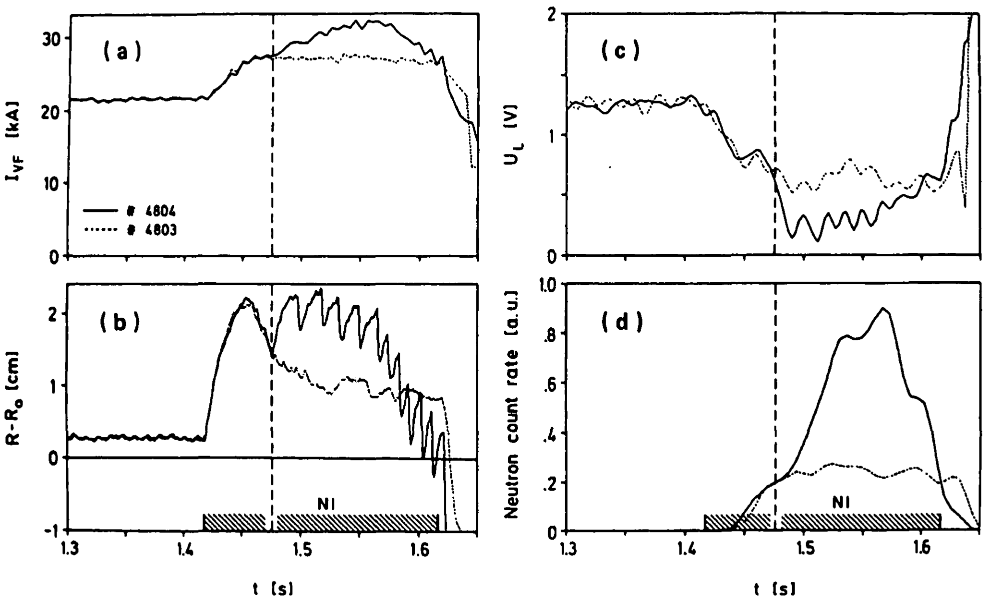

FIG. 4. Comparison of several plasma parameters of an L-discharge (No. 4803, dotted lines) and an H-discharge (No. 4804, solid lines).
(a) Vertical field curent I_{VF}, (b) shift of the plasma position R-R_0 (R_0 = 165 cm), (c) loop voltage U_L, (d) neutron count rate ϕ_n. The transition to the H-phase is indicated by dashed lines.

decreases. As a consequence, the wall recycling and the H_α intensity in the main plasma also decrease. Figure 5 summarizes the H_α variation measured at the typical locations, as indicated in the insert. Various aspects of the transport barrier will be discussed in Section 6.2. The changes in plasma properties caused by the transport barrier are described here; it gives rise to rather broad bulk plasma profiles with high peripheral values and steep gradients at the edge.

The profile changes affect the MHD behaviour of the discharge; the high electrical conductivity at the edge, which is a consequence of the good confinement properties of the plasma even at the periphery, causes the current channel to expand. Evidently, as a consequence of the steep edge gradients, a new MHD feature — the edge localized mode — appears.

The impurity development is determined by a rather complicated chain of events; the reduced transport in the SOL leads to better particle exhaust and therefore less recycling at, and reduced impurity erosion from, the divertor throats. The improved particle confinement reduces the charge exchange fluxes to the walls. On the other hand, the increased edge ion temperature will give rise to higher sputtering. The confinement of impurities and of the main plasma species will be improved; in particular, without sawteeth the effective impurity confinement in the plasma centre is high, whereas in the boundary region it will be reduced by ELMs. The combination of these different erosion and confinement effects determines the evolution of the impurity concentration in the plasma and the development of steady state conditions. The broadening of the conductivity profile after the L-H transition will introduce a further time constant in the development of the plasma properties in the H-phase.

Finally, the transport barrier affects the power fluxes out of the discharge, and ELMs — being a violent MHD feature — open up a new power loss channel with different transport and power deposition characteristics which may require a specific design of the target plates for future experiments.

2.2.1. *Profile development*

The tendency of all plasma profiles is to broaden in the H-mode. Figure 6 shows the time dependence of the electron temperature at three spatial locations and the line averaged density along three chords. In case (a), the density is regulated by a feedback system; in the H-phase the external gas flux becomes zero. In case (b), a strong and constant gas flux is maintained during the beam phase. This additional gas flux is initiated shortly before the beam is switched on and causes the Ohmic density to rise. The L-H transition leads to a sharp

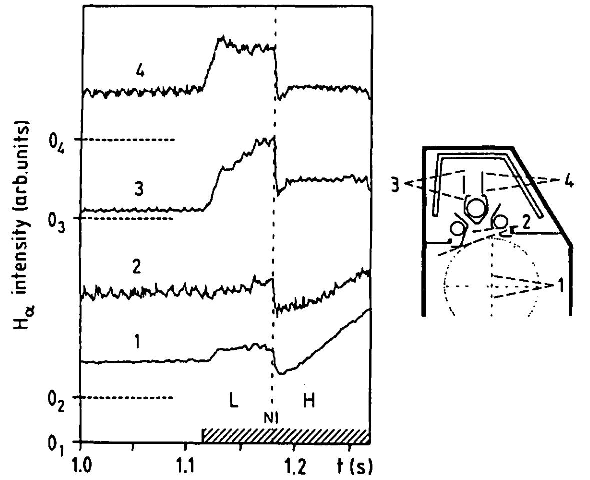

FIG. 5. Variation of the H_α intensity at different viewing angles (as shown separately) with neutral injection and at the L-H transition.

rise of both the electron temperature and density. In case (a) the rise in T_e is more pronounced, while in case (b) the rise in n_e is stronger. In both cases the relative rise in T_e and n_e increases towards the plasma edge.

Figure 2(b) shows the development of the T_e and n_e profiles from the Ohmic phase via the L-phase to the H-phase, measured with the multi-pulse Thomson scattering system, which gives a profile every 17 ms. In the H-phase, high T_e and n_e values at the periphery quickly develop from one laser time-point to the other. In some cases, both profiles develop shoulders at the edge. Without ELMs the density continuously increases after the L-H transition, causing the central T_e and T_i values to decrease after an initial rise.

The T_e gradient at the edge increases from 45 eV·cm^{-1} by a factor of four to 185 eV·cm^{-1}. This increase reflects a change of the plasma heat diffusivity at the edge (discussed in more detail in Section 6.2). The electron pressure gradient at the edge, which is 1×10^5 Pa·m^{-1}, increases by a factor of six. The steep gradient at the edge of the H-mode plasma may provide the instability conditions for ELMs (discussed in Section 2.3.3).

In Fig. 7, the profiles of the ion temperature T_i measured by passive charge exchange in the pre-transition phase are compared with those in the H-mode with ELMs. The tendency of the T_i profile is to broaden, reaching high values at the periphery. As mentioned above, the

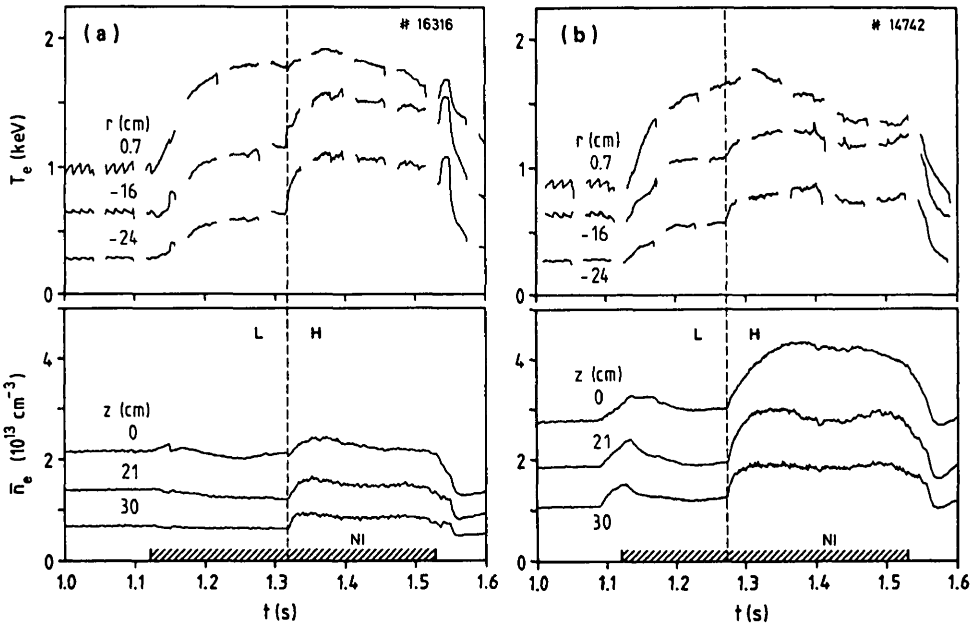

FIG. 6. Time evolution of the electron temperature T_e and the line averaged density $\bar{n}_e$ at three positions during the beam heating phase with L-H transitions (dashed vertical line).
In case (a), the density is regulated by a feedback system; in case (b), the internal gas flux is increased just before the beam is switched on and is then maintained at a constant level. The breaks in the electron cyclotron emission traces are caused by a chopper which is used to monitor possible drifts in the background signal.

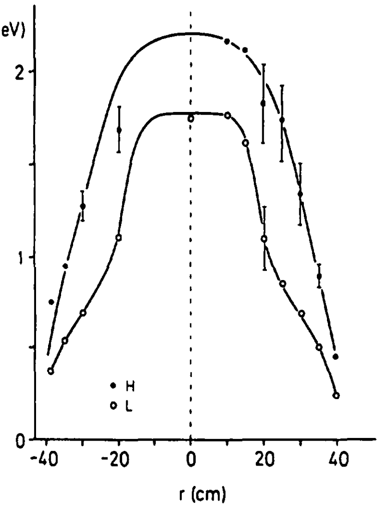

FIG. 7. Ion temperature profiles in the H-phase and at the end of the preceding L-phase, as measured by passive charge exchange ($H^0 \rightarrow D^+$). I_p = 0.38 MA, B_t = 2.2 T, P_{NI} = 3.3 MW.

high edge ion temperatures will give rise to increased charge exchange wall sputtering in the H-mode. The heating efficiencies for electrons and ions, $\eta_{e,i}$ ($\eta_{e,i} = \bar{n}_e \Delta T_{e,i} / \Delta P_{abs}$ = rise of electron or ion temperature with heating power, normalized to the line averaged density), are found to be higher in the H-mode than in the L-mode; in particular, $T_e(0)$ does not seem to saturate in the H-mode as it does in the L-mode. For a plasma current of 300 (380) kA, η_i increases from 1.6 (2.8) × 10^{13} keV·MW^{-1}·cm^{-3} in the L-mode to 2.5 (4.2) × 10^3 keV·MW^{-1}·cm^{-3} in the H-mode.

The thermal neutron flux ϕ_n increases after the L-H transition with H^0 injection into a D^+ plasma, as shown in Fig. 4(d) in comparison with an L-discharge. ϕ_n increases typically by a factor of two to four; the difference in ϕ_n between an H-discharge and an L-discharge of the same density, however, is a factor of about six. The increase in ϕ_n is caused by the broadening of the T_i profile and the rise in density in a confinement situation where, however, the ion temperature does not decrease when $\bar{n}_e$ increases. The analysis of the neutron flux points towards an improvement of the deuterium to hydrogen ratio after the L-H transition. During deuterium injection into deuterium plasmas the neutron production is dominated by beam-target reactions and is larger than in the case of hydrogen injection by about two orders of magnitude. The fusion rate of beam-target reactions is determined by the distribution function f_{inj} of the injected deuterons and by the target ion temperature. This distribution function is established during the slowing down of the ions, and thus the product of target electron density and f_{inj} is a function of the target electron temperature only. Therefore, the time development of the neutron count rate follows that of the central electron temperature, independent of changes in the target density. Since the electron temperature is not drastically changed after the L-H transition, in spite of the rising density, the neutron count rate for $D^0 \rightarrow D^+$ is similar in the L-regime and in the H-regime.

2.2.2. *Bootstrap currents and beam driven currents in the H-mode*

The increase of the electron temperature in the H-mode causes a further decrease of the loop voltage — in some cases to nearly zero. Figure 8 shows the development of the loop voltage from the OH-phase through the L-phase to the H-phase. Computer simulations have been used to investigate the effect of bootstrap currents and beam driven currents on the loop voltage and the toroidal current profile in H-plasmas [10]. It is found that loop voltages computed with neoclassival resistivity agree with measured values only if Ohmic, bootstrap and beam driven currents are included.

In a 320 kA discharge, bootstrap currents of up to 100 kA, with broad profiles, and beam driven currents of 50 kA, with peaked profiles, are generated (see Fig. 9). The sum of these currents can be 47% of the total plasma current. The resulting current density j(r) is found to adjust to the broader electron temperature and electrical conductivity profiles in the H-phase on a time-scale comparable to the resistive time-scale for the redistribution of current density, $\tau_{res} \approx 400$ ms. The broadening of j(r) due to bootstrap and beam driven currents has been shown to be a smaller effect, which also occurs on the resistive time-scale.

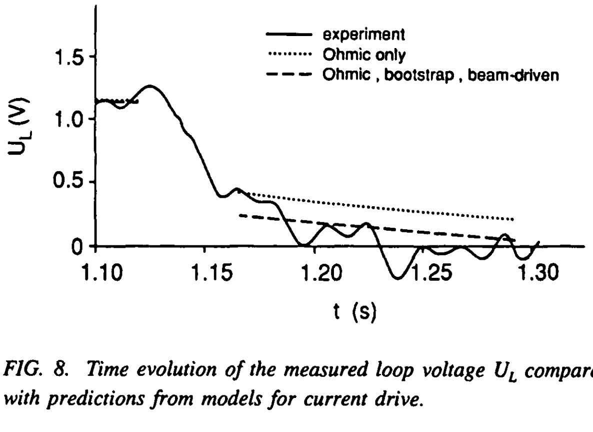

FIG. 8. Time evolution of the measured loop voltage U_L compared with predictions from models for current drive.

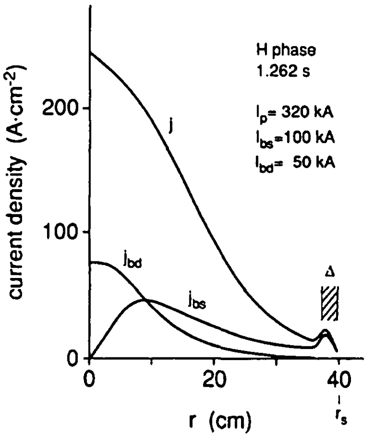

FIG. 9. Current density profiles: of the bootstrap current j_{bs}, the beam driven current j_{bd} and the total current j, in the ELM-free H-phase. Δ denotes the width of the steep gradient zone.

2.3. MHD characteristics of the H-mode

In this section, the MHD properties of the H-mode are discussed. Also, the preceding L-phase has to be considered, for several reasons. In particular, the behaviour of the m = 1/n = 1 mode and the sawteeth plays a dominant role and is, therefore, treated in Section 2.3.1, together with the m > 1/n = 1 modes coupled to the central mode. Apart from these modes, m ≥ 2 instabilities are observed which are clearly localized at the corresponding rational magnetic surfaces q = m/n ≥ 2. As shown in Section 2.3.2, there are characteristic differences between L-type and H-type plasmas as far as Mirnov oscillations are concerned. A still more characteristic and more important feature of the H-mode is the occurrence of a new type of instability, the ELM; Section 2.3.3 is dedicated to this topic. A comparison of the experimental findings and the theoretical models is presented in Section 7.

2.3.1. *Behaviour of the m = 1 mode and the sawteeth*

Ohmic discharges are generally subject to sawtooth fluctuations. The m = 1 precursors are small and grow within a few cycles; their rotation is in the electron diamagnetic drift direction, with a frequency of a few kilohertz. No coupled signal on the Mirnov loops is detectable.

In DIII-D [11] it has been observed that no H-mode develops when neutral injection is applied to an Ohmic discharge without sawteeth. In ASDEX, we have studied the importance of sawteeth in the Ohmic phase regarding the development of the H-mode and compared discharges which differed only in this MHD aspect. Figure 10(a) shows the central electron temperature of two discharges, illustrating the lack of sawteeth in one of them. Figure 10(b) plots the time variation of $\bar{n}_e$, $\beta_{p\perp}$ and H_α in the divertor chamber. The comparison shows that in the H-phase the two discharges do not differ in any important aspect. Contrary to what was found in DIII-D, in ASDEX it is irrelevant for the development of the H-mode whether there are sawteeth or not in the OH plasma before the L-phase preceding the L-H transition.

When neutral injection is applied, the m = 1 mode is still the leading mode in the bulk plasma. The wave form of this oscillation depends on external parameters which influence the profiles, i.e. the plasma configuration (limiter versus divertor), the NI power level, and the local electron transport properties, which are different in L- and H-discharges and in hydrogen and deuterium plasmas.

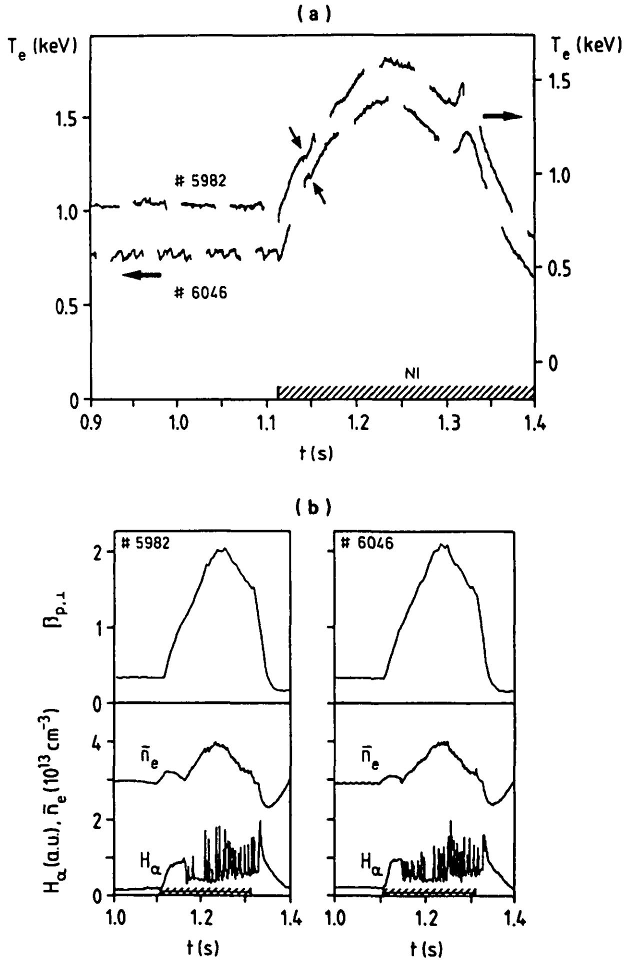

FIG. 10. (a) Central electron temperature of two discharges, one with sawteeth (No. 6046) and one without sawteeth (No. 5982), in the Ohmic phase. The arrows denote the L-H transition.
(b) Comparison of $\bar{n}_e$, $\beta_{p\perp}$ and H_α radiation in the divertor chamber for the two cases.

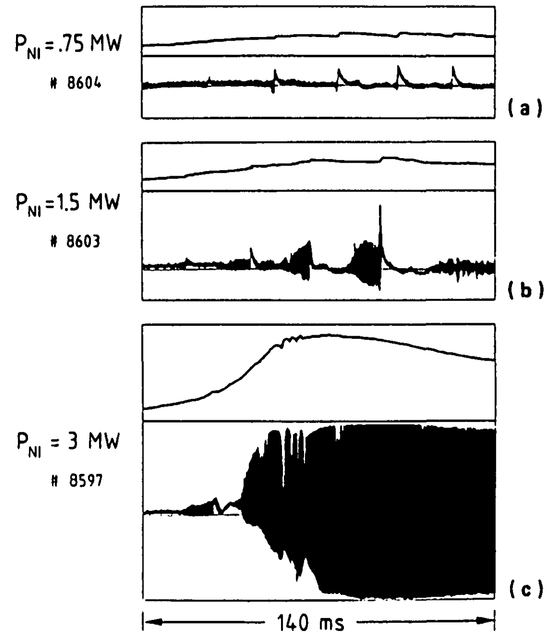

FIG. 11. Central soft X-ray signals showing the evolution of m = 1 modes and sawteeth during neutral injection at different beam powers P_{NI}.

Neutral injection into limiter discharges gives rise to periodically growing m = 1 modes which cause sawtooth disruptions and then vanish. The sawtooth repetition time increases somewhat with the beam power, but it quickly saturates at about 35 ms.

A different behaviour is observed in divertor discharges. Figure 11 shows the m = 1 and sawtooth behaviour at three different power levels. At low NI power (Fig. 11(a)), the m = 1 amplitude is small and its occurrence is repetitive, being terminated by a sawtooth. Contrary to what is observed in limiter discharges, the sawtooth repetition time increases with the beam power. At an injection power of >2 MW (Fig. 11(c)), the divertor discharges are free of sawteeth, except for a single sawtooth at the beginning of the NI pulse; this sawtooth is caused by a slowly growing m = 1 mode which leads to internal disruption after about 50 cycles. After the sawtooth, when q_0 has sufficiently dropped below 1, an m = 1 mode appears which saturates at a large amplitude without giving rise to any further sawteeth. Irrespective of the MHD oscillation level, all three examples represent L-type discharges with deteriorated confinement.

It is possible to achieve H-mode plasmas well below an injection power of 2 MW, i.e. below the power threshold for sawteeth to disappear in L-mode discharges. In these cases, the L–H transition is frequently triggered by a sawtooth crash, as is shown in Fig. 12. After the sawtooth, at t = 1.18 s, the electron temperature at the edge does not decrease as it did in the previous cases; rather, it continues to grow. Observations of such transitions have provided the first evidence of the role of a critical temperature (or a related quantity) in the near-boundary region; this subject is further discussed in Section 6.

Typically, deuterium H-mode plasmas are free of sawteeth; sawteeth occur only at low injection power together with a high plasma current. In contrast, hydrogen H-mode discharges exhibit sawteeth within the available power range ($P_{NI} \leq 3.5$ MW).

If a saturated, continuous m = 1/n = 1 mode has been established, it usually persists during neutral injection, provided the plasma remains in the L-regime. Sometimes, however, the plasma develops fishbone-like bursts. More often, an L–H transition occurs in the presence of such continuous modes the amplitudes of which then decrease on time-scales of between several milliseconds and several tens of milliseconds. An example of a rather fast decrease is shown in Fig. 13.

After the transition, the m = 1 mode occurs repetitively as fishbone-like bursts. The occurrence of these bursts indicates that q(0), the central value of the safety factor, is — at least temporarily — below 1 during the H-phase.

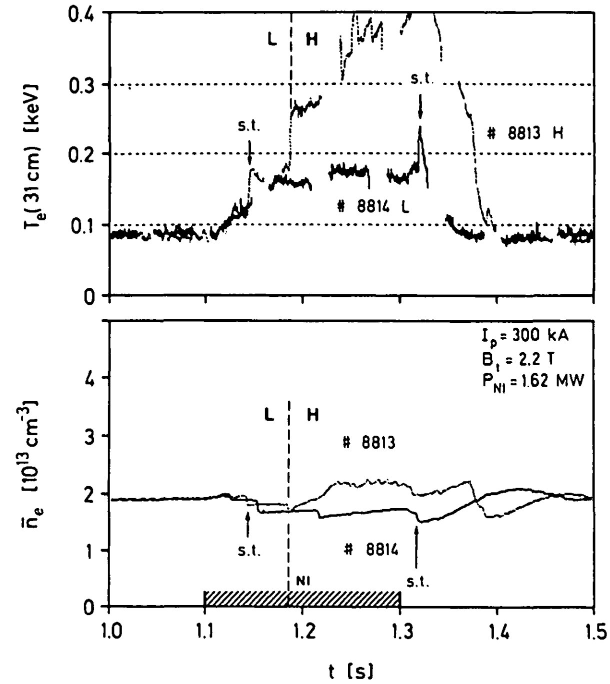

FIG. 12. Edge electron temperature T_e (measured by ECE) and line averaged electron density $\bar{n}_e$ of an L-discharge (No. 8814) and an H-discharge (No. 8813). Sawteeth (s.t.) are indicated by an arrow. The L–H transition is triggered by a sawtooth.

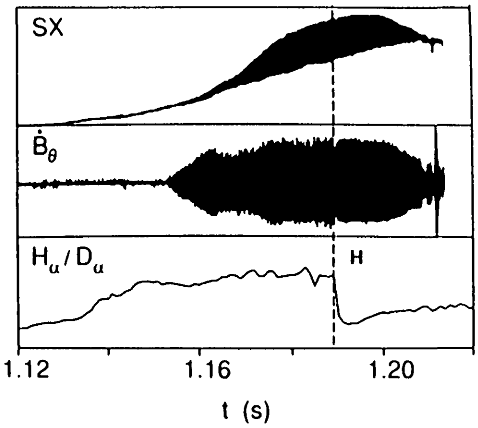

FIG. 13. Temporal evolution of soft X-ray emission (central chord, m = 1), $\dot{B}_\theta$ (m = 2) and H_α/D_α emission from the divertor. The L-H transition occurs at t = 1.19 s.

Since the time between two bursts is typically of the order of 10 ms, it is inconceivable that q(0) exceeds 1 substantially, if at all, during such periods. The m = 1 mode thus provides very important information on the current density profile, which would otherwise have to be obtained in a much more indirect way; when the Z_{eff} profiles are sufficiently flat, the broad electron temperature profiles lead to accordingly broad conductivity profiles. The current density profile is expected to follow this development on the skin time-scale, which is comparable to the NI pulse duration of 200–400 ms. Thus, it is obvious that the current density distribution cannot vary drastically. On the other hand, the possible development of peaked or hollow Z_{eff} profiles and the contribution of bootstrap and beam driven currents (see Section 2.2.2) might change this simple picture.

Because of the unidirectional neutral injection into the ASDEX device, the plasma rotates toroidally with central velocities of the order of 10^5 $m \cdot s^{-1}$ per MW, which leads to a frequency of the m = 1/n = 1 signal of 10 kHz per MW. If this rotation is fully developed, the contribution of the electron diamagnetic drift to this frequency is considerably smaller. The central m = 1 mode is always observed to be coupled to an m > 2/n = 1 mode, which manifests itself as Mirnov oscillation having the same direction of propagation, the same frequency and a similar temporal evolution of the amplitude (see Fig. 13). (Note that the amplitude of a soft X-ray (SX) diode signal is proportional to the perturbation level only in the case where the electron temperature, the electron density and the spectral composition of the recorded light do not vary appreciably.) The occurrence of these coupled modes is observed for all wave forms of the m = 1 instability, i.e. sawtooth precursor, continuous oscillation and fishbone-like burst. It is noteworthy that the poloidal mode number of the m > 2/n = 1 satellite mode always exceeds the q value at the boundary calculated from B_t, I_p and $\beta_p + \ell_i/2$, taking into account the toroidal effect but neglecting the contribution of the divertor coils. The q value is singular at the separatrix of an ideal poloidal configuration. In practice, the q value attains a finite maximum (owing to, for example, slight deviations from toroidal symmetry), which nevertheless exceeds the value of a non-divertor configuration. The coupled mode is not detectable by the SX camera and, therefore, it is not possible to decide whether it is excited inside or outside the separatrix.

The amplitude of this coupled mode is rather small and, hence, it does not lead to islands of considerable size, particularly since the mode resides in a region of increased shear close to the separatrix. Nevertheless, it is mostly sufficient to exceed the amplitude of another Mirnov oscillation which apparently is a characteristic signature of L-type discharges, as is discussed in the next section.

2.3.2. *Localized m ≥ 2 modes*

It has already been mentioned that the propagation of the near-centre m = 1 mode is dominated by the toroidal rotation of the plasma, while the diamagnetic electron drift causes only a minor modification. In the case of co-injection (the most frequent heating scenario), the phase velocity and hence the signal frequency is reduced by the contribution from this mode. The resulting direction of mode propagation depends, therefore, on the profiles of both the toroidal rotation and the diamagnetic drift velocities. In Ref. [12], this behaviour is treated in detail. For the purpose of this paper, a qualitative discussion should be sufficient. It can be concluded from measured pressure profiles that the poloidal angular frequency, $\omega_p = v_d/r$, of the diamagnetic drift velocity v_d does not vary appreciably over the minor radius. In contrast, at the plasma boundary the velocity of the toroidal rotation and hence the toroidal angular frequency, $\omega_t = v_t/R$, are nearly zero and, thus, the diamagnetic drift velocity may overcome the effect of the toroidal rotation for modes localized near the plasma boundary. This trend is, of course, supported by the weighting factors m and n, the ratio of which increases towards the plasma edge.

Obviously, the m = 1/n = 1 mode discussed in the preceding section is a localized mode, since it propagates according to the resulting local velocity, while the m > 2/n = 1 satellite is a driven mode. In many L-type

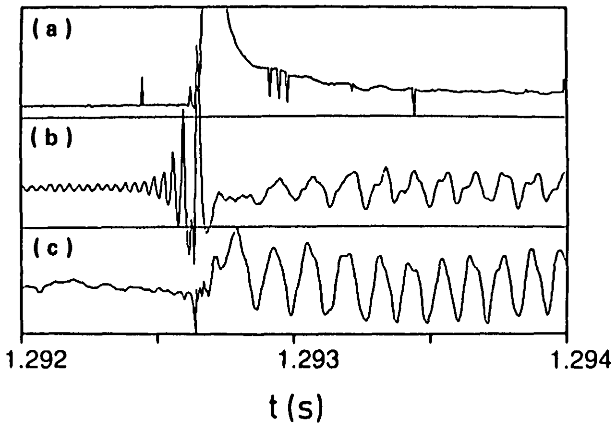

FIG. 14. Onset of the m = 2 oscillation in discharge No. 18033.
Trace (a): H_α/D_α signal (diode saturates).
Trace (b): Mirnov signal, midplane outside.
Trace (c): Mirnov signal, midplane inside.

discharges and in many L-phases before the L-H transition, besides these two modes a third mode with a distinctly lower frequency is observed in the Mirnov oscillations. Sometimes, the amplitudes are such that both frequencies are clearly seen in the raw signals. More frequently, however, the fast oscillation dominates, the slower one appearing only as an additional line in the Fourier spectrum. Using an ideal filter method, the two modes can be separated, and in this way it is shown that the slower mode propagates in the electron diamagnetic drift direction [13]. The toroidal mode number n is always 1 and the poloidal mode number m is 3 or 4; the latter is always close to but smaller than q_a.

To some extent, this mode is typical of L-type plasmas. It can be observed over phases of 100 ms or more, but it quickly disappears after the L-H transition; the amplitude becomes undetectable within a few milliseconds. After the L-H transition, it reappears rapidly. During the H-phase, it reappears only transiently together with ELMs. From the temporal sequence of events it is concluded that this mode is not a precursor of ELMs; rather, it seems to be triggered by them. This aspect will be discussed in the following section. Concerning the behaviour of this mode in the L-H-L sequence, one might speculate whether or not these transitions are due to changes in the current density profile.

In several H-mode discharges, two other localized modes are observed, namely $m = 2/n = 1$ and $m = 3/n = 2$. The latter is the only Mirnov oscillation with a toroidal mode number $n > 1$; it may exist over several hundreds of periods, but with small amplitudes which do not impair confinement.

In contrast, if an $m = 2/n = 1$ mode comes up, it quickly attains amplitudes corresponding to island sizes of up to 10 cm. The resulting degradation of confinement is clearly seen by comparison with discharges that do not exhibit this mode but have otherwise equal conditions [14].

If the $m = 2/n = 1$ mode occurs, its onset is always characterized by the sequence of events shown in Fig. 14. A fishbone-like burst is followed by an ELM which apparently triggers the $m = 2$ mode, which also propagates in the direction of the toroidal rotation but with a distinctly lower frequency owing to the features discussed above. Thereafter, the frequency of this mode tends to decrease, which may be attributed to mode locking. Frequently, a disruption occurs after several tens of milliseconds; there are, however, discharges in which the mode persists up to the end of the injection pulse.

If q_a is sufficiently large (e.g. > 2.7), L-mode plasmas are not susceptible to $m = 2$ modes or disruptions; the same applies to H-mode plasmas as long as beta is well below the Troyon limit [15]. The occurrence of disruption is restricted to discharges that aim at reaching or exceeding this limit. Most frequently, the $m = 2$ mode is excited in the phase of rising beta. On the other hand, non-disruptive decay of beta occurs more often in beta limit discharges in ASDEX.

2.3.3. *Edge localized modes*

Edge-localized modes are a new type of MHD instability which is observed in ASDEX [3] and in other devices in the H-phase only. They appear as rather irregular events which cause energy and particle losses from the main plasma on a time-scale of the order of 10^{-4} s. In this respect, the ELM has an effect similar to that of the disruptive instability. In contrast to disruptions, during ELMs the losses are restricted to the outer regions of the plasma and lead to changes in β_p of at most 0.1. The repetitive occurrence of ELMs, however, appreciably reduces the effective confinement time, as can be seen from the study of quiescent, ELM-free phases (see Section 3.4.3.1). The effect of ELMs on energy confinement is discussed in Section 3.4.3.2.

These modes are localized at the plasma edge. The location of ELMs is indicated in Fig. 15, which is a plot of the ECE measured electron temperature at the plasma centre (r = 1 cm) and halfway to the edge (r = 24 cm) during the NI phase, preceded and succeeded by Ohmic phases. During the Ohmic phases, the central electron temperature is periodically modulated by sawteeth. During neutral injection, the

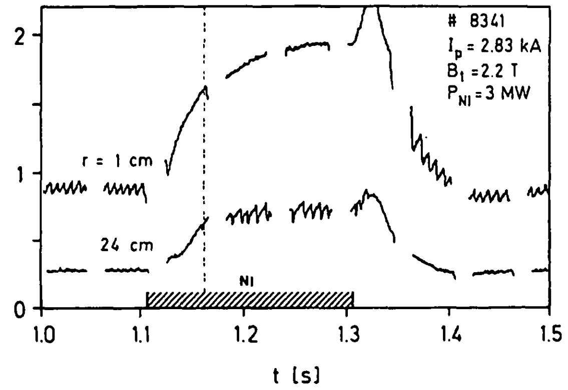

FIG. 15. ECE measured electron temperature T_e at the plasma centre (r = 1 cm) and half-way to the edge (r = 24 cm), showing that ELMs are localized in the outer part of the plasma. In the OH-phases the central electron temperature is modulated by sawteeth.

centre is unaffected, but — in the H-phase — rather similar relaxation phenomena appear as modulations on the outer T_e channel. The spatial variation of $\Delta T_e/T_e$ and $\Delta n_e/n_e$ as shown in Fig. 16 demonstrates that this mode affects the plasma in the range from about a/3 to a. The $\Delta T_e/T_e$ variation of sawteeth is also plotted for comparison.

It is well known that the disruptive instability is usually preceded by a growth of the $m = 2/n = 1$ mode, which is often readily observable over at least a few cycles. No corresponding precursor to an ELM has been found. Sometimes, ELMs are preceded by sawteeth and appear to be triggered by them. The same holds for fishbone-like bursts. More frequently, however, the occurrence of ELMs is clearly separated from $m = 1$ activity; both types of events can be observed in the same discharge. Thus, it must be concluded that the $m = 1$ mode and its satellite mode are not precursors of ELMs.

Particular attention has been paid to discharges in which neither a sawtooth nor a fishbone-like burst nor any other competing MHD activity (such as the 2/1 and 3/1 modes described in the previous section) occurred before an ELM. This situation is quite common, but it is only in very rare cases that weak precursor-like Mirnov oscillations with a duration of roughly half a cycle and with toroidal mode numbers $n \leq 3$ have been detected [16].

The fast decrease of the poloidal beta caused by an ELM leads to a fast inward motion of the plasma column by typically a few millimetres, which obviously gives a signal on the Mirnov probes that is usually large compared with oscillating mode amplitudes. By summation of the signals of the outside and inside coils the effect of the fast inward motion could be removed. Nevertheless, with this technique it was possible to detect a helical instability which occurs during the ELM and lasts for typically ten cycles or less [17]. By comparison with other signals corresponding to ELMs, it is found that this instability is not a precursor; rather, it appears to be triggered by the ELM. The mode structure and propagation are very similar to those of the uncoupled mode existing in the L-phase, as described in the preceding section. In particular, in the course of a discharge the mode number remains the same.

Regardless of the existence of this instability, the relaxation process itself does not appear to be correlated with a certain rational surface. This is concluded from the measurement of SX emission profiles, shown in Fig. 17. The minimum at r = 36 cm does not shift when q_a (cylindrical definition) is varied between 2.4 and 5.6. It is therefore assumed that ELMs are not located at a fixed resonant surface but are always very close to the plasma boundary. Since ELMs are only observed in the H-mode, it is tempting to conclude that the crucial element leading to the H-mode (which seems to be the transport barrier at the edge) also gives rise to a new instability condition.

Since ELMs are localized close the the plasma edge, it is obvious that the steep edge gradients of the H-mode are responsible for ELMs (see Fig. 28).

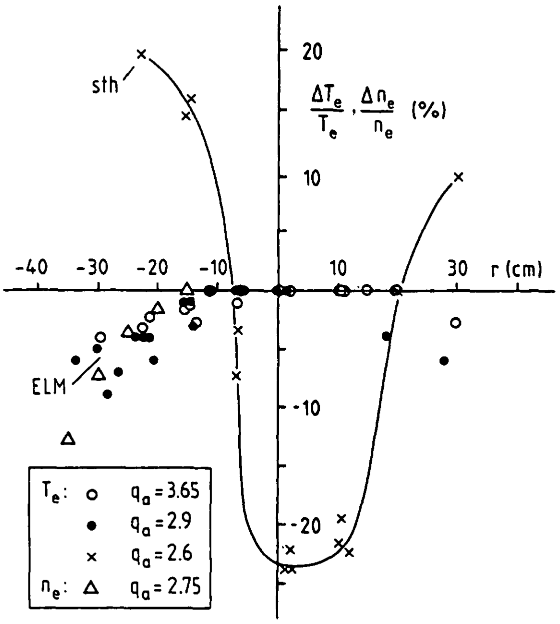

FIG. 16. Relative variation of the electron temperature and density due to ELMs versus plasma radius. The variation of T_e due to ELMs is compared with that due to sawteeth.

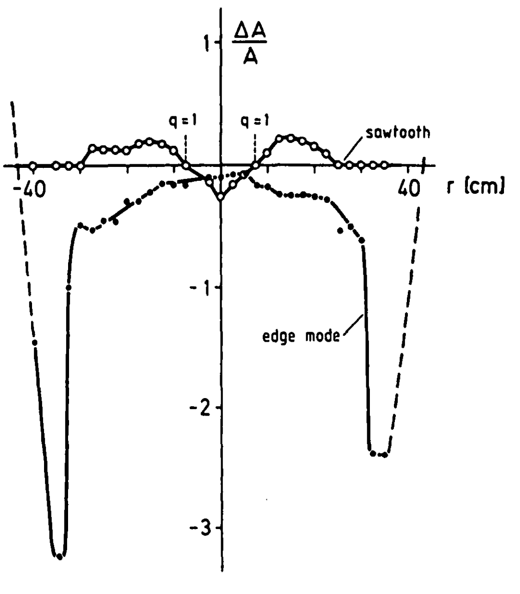

FIG. 17. Radial distributions of soft X-ray fluctuations connected with an ELM and a sawtooth. The measurements indicate that the ELMs are localized at the plasma edge.

The increase in SX intensity as observed during ELMs is ascribed to the release of particles and energy from the main plasma. This release is most clearly recorded by the lithium beam probing the local density around the separatrix. Figure 18 is a three-dimensional plot of the Li[2p-2s] light intensity, which is approximately proportional to the electron density.

Since the energy and particle flows into the divertor chamber are transiently increased during ELMs, there is a burst-like modulation of all divertor diagnostic signals, in particular those of the H_α/D_α light emission from the divertor chamber. Thus, the same signal monitors the L-H and the H-L transitions as well as the occurrence of ELMs, as is shown in many figures (for example, Figs 1, 2 and 6). This signal is routinely recorded with a sampling rate of 1 kHz and in many cases with a sampling rate of 250 kHz. From these data, the rise time is taken to be typically 50–100 μs, which is longer than the response time of the photodiode. The half-width of the signal ranges from 100 to 400 μs. The rise time of the H_α/D_α emission in the divertor chamber with respect to data from the main chamber is delayed by typically 100 μs. From all these observations it follows that ELMs occur on the MHD time-scale. Simply expressed, an ELM could be regarded as a transient return to the L-regime. This view is supported by the reappearance of the non-coupled mode, which, as shown in Section 2.3.2, is a characteristic feature of L-type plasmas. On the other hand, the energy and particle flows during ELMs can far exceed those of the L-phase.

In the H-phase, ELMs have various amplitudes and frequencies. They can be singular events, producing a large and distinct spike in the divertor H_α radiation. On the other hand, ELMs can occur as groups of small events; these ELMs have been dubbed 'grassy ELMs' because the appearance of divertor H_α radiation leads to this association. It has been speculated that singular ELMs are caused by an MHD phenomenon, but that grassy ELMs are caused by an unstable development of the H-phase during which the plasma oscillates between the L-phase and the H-phase.

The same wave form of the SX radiation is caused by a singular ELM and by one of the grassy ELMs. At the plasma edge, both singular ELMs and grassy ELMs cause a transient signal rise; more inside, the signal decreases. The relative decrease of the SX radiation, 5 cm inside the separatrix, is ~50% in the case of a singular ELM but only ~10% in the case of a grassy ELM. A singular ELM modulates the SX radiation measured along a chord through the centre; in the case of a grassy ELM, the signal modulation peters out between 10 and 20 cm from the centre. From this comparison we conclude that a grassy ELM also constitutes an MHD feature but that it has a smaller amplitude than a singular ELM.

The spatial structure of the energy release due to ELMs is difficult to assess since there are no sufficiently fast and detailed measurements, especially regarding toroidal variations. Because of the expected axisymmetry

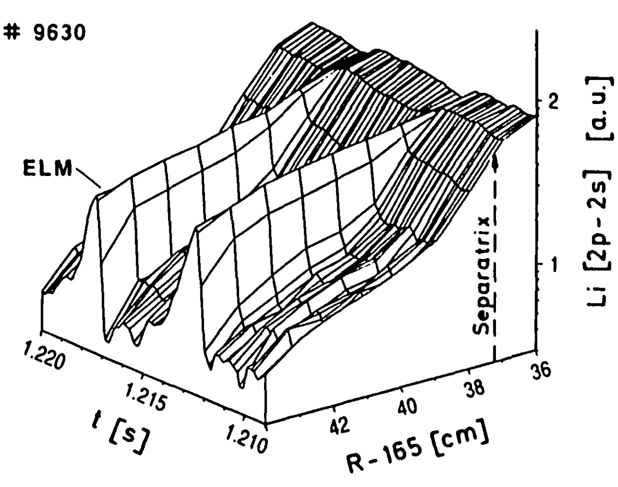

FIG. 18. Three-dimensional plot of the Li [2s-2p] light intensity along the beam over the period 1.209–1.22 s, encompassing two ELMs.

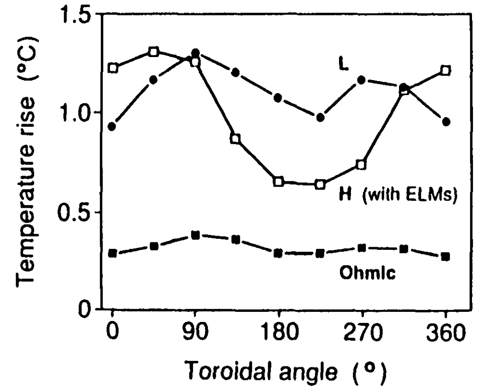

FIG. 19. Temperature rise of the cooling water in the eight toroidal segments of the upper, outer target plate. The three curves represent averages over four Ohmic discharges, seven L-mode dominated discharges and six H-mode ELM-dominated discharges. The beam heated shots have about the same total energy input.

of the equilibrium, most diagnostics are restricted to one poloidal plane and toroidal asymmetries are therefore not detected. Recently, however, new and important information was obtained on ASDEX when the original radiation cooled titanium target plates (DV-I) were replaced by a water cooled structure (DV-II); with these new divertor plates it is possible to perform time integrated but toroidally resolved measurements of the target power load by calorimetry. In Ohmic discharges as well as in discharges dominated by a long L-phase, the toroidal variation was less than 20%. However, in discharges with a long H-phase and many large ELMs, with only short L-phases at the beginning and at the end of beam heating, a nearly sinusoidal modulation of the deposited energy with n = 1 was observed (see Fig. 19). A difference between the maximum and the minimum power loads of up to a factor of three was found, depending on the actual evolution of the discharge.

Part of the power load obviously comes from the more homogeneous Ohmic phase and the L-phase as well as from the quiescent period between ELMs. Since, in addition, the signal represents a time average over many ELM events, it is concluded that the asymmetry for an individual ELM is significantly larger and that successive, virtually independent ELMs occur with approximately the same toroidal phase angle, indicating phase locking with respect to some fixed external perturbation. Since the only significant plasma-wall contact occurs at the target plates, the ELMs appear to be locked at non-axisymmetric external magnetic field perturbations. These may be caused by, for example, a slight misalignment of the divertor coil triplets in ASDEX. In fact, it has been shown by field line tracing that a random sideward shift or tilting of the multipole coils within mechanical tolerances of a few millimetres causes magnetic field ergodization around the separatrix and spatially fixed islands of a few centimetres in radial width on low rational surfaces inside the separatrix [18]. Since the magnetic field coils were not changed during the reconstruction of the divertor, we believe that the same perturbation and hence similar mode locking were also present in the previous arrangement (DV-I).

Previously, experimental evidence of such field errors was obtained from the destruction pattern on the original titanium target plates [19]; these errors could be traced back to local thermal overload by a high energy electron minority produced by lower hybrid current drive and partially lost along perturbed field lines intersecting the target plates.

Figure 19 shows that the total power load in the ELM dominated case is somewhat lower than in normal L-shots at the same total energy input. This indicates that some energy is deposited elsewhere, for example at the divertor throat, because of the wider radial profile of ELMs.

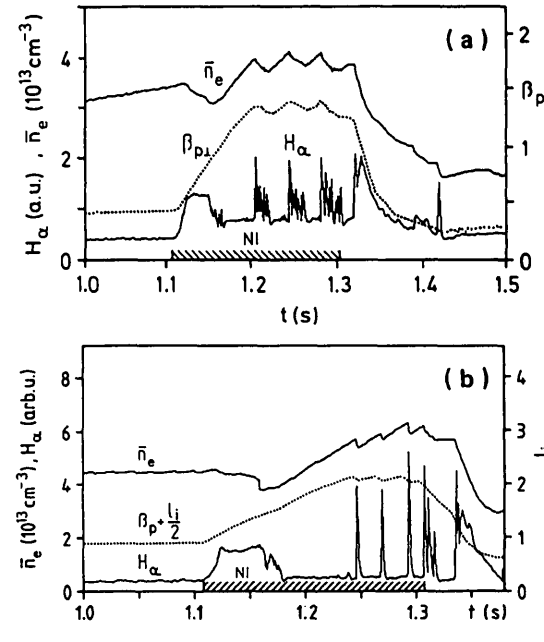

FIG. 20. (a) Variation of $\bar{n}_e$, $\beta_{p\perp}$ from the diamagnetic signal and H_α at a sudden termination of ELMs.
(b) Variation of $\bar{n}_e$, $\beta_p + \ell_i/2$ from equilibrium and H_α with singular large ELMs.

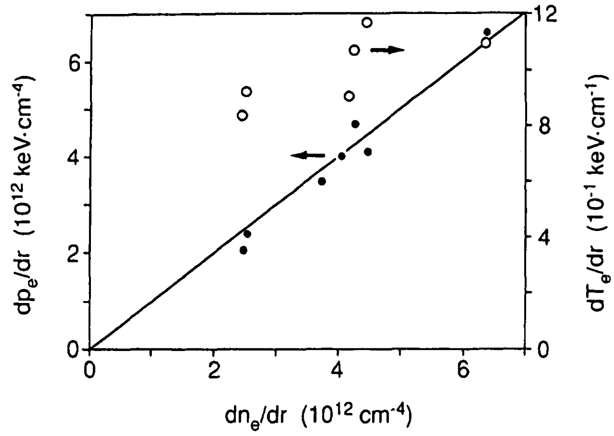

FIG. 21. Variation of the electron temperature and density gradient with the pressure gradient at the plasma periphery, at the end of quiescent H-phases shortly before the H-L transition. The edge pressure gradient is varied by changing the distance between the separatrix and the outer vessel wall, and by the plasma current.

The energy loss due to an ELM can be up to 4 kJ on one target plate; summed over all target plates, this corresponds to the energy content of an annulus at the plasma surface of several centimetres. Steady state conditions for the plasma energy content are provided only for ELMs with a period of about 6 ms. The effect of ELMs on the confinement of an H-discharge cannot easily be assessed in all cases because ELMs can be of high frequency with low amplitude or of low frequency with high amplitude (see Section 3.4.3). (Here and in the following, the amplitude of the H_α/D_α signal is considered as a measure of the violence of an ELM.) Generally, ELMs are more frequent at lower heating power; at higher heating power they are less frequent but have a more distinct pattern. Figure 20 shows the development of the density, the poloidal beta and the H_α radiation in the divertor chamber for two cases. One case is characterized by frequent ELMs which suddenly stop for short quiescent periods; in the other case the basically quiescent H-phase is interrupted by large ELMs. The poloidal beta in Fig. 20(b) is taken from the flux and from B_θ loops positioned inside the vacuum vessel; the diamagnetic loop is positioned outside the vacuum vessel and hence the signal is integrated with the vessel time constant of 16 ms. Both cases document the impact of ELMs on the particle and energy contents and show that ELMs can indeed lead to saturation of these parameters. The case of Fig. 20(b) with singular ELMs shows that the gain in particle and energy contents in the quiescent periods between ELMs is lost again during the ELM events. This is similar to the effect of a sawtooth. While a sawtooth, however, is an internal mode which redistributes the energy in the plasma core, an ELM is an external mode with a deteriorating effect on global confinement.

Since the occurrence of ELMs is erratic, it is difficult to study the cause of their appearance. The frequency of ELMs tends to increase at lower current and constant toroidal field, whereas their amplitude decreases, which indicates that ELMs may be correlated with the current density profile in the range of the steep electron temperature gradient at the edge. However, ELMs have a stronger impact on the edge density than on the temperature (see Fig. 64). No correlation between ELM frequencies is observed for the cases of ramp-up and ramp-down of the plasma current (especially when the current is increased or decreased at the plasma edge during the H-phase). It is also possible that ELMs are driven by the steep pressure gradient at the edge. The pressure gradient may be steep enough (within the accuracy of the edge measurements) to violate the ideal ballooning limit (on the assumption of a shear of $S = 2$ at the edge). At present, it is not possible to make a clear distinction between the two potential driving mechanisms — the current or the pressure gradient. The edge stability conditions are discussed in Section 7.

ELMs can be stabilized by moving the plasma column closer to the outer wall. This has been applied successfully at various stages of the experiment. Quiescent H-phases can be achieved with this method. Whether ELMs can be wall stabilized has not been proven yet. However, the maximum edge electron pressure seems to be correlated with the separation from the wall (correlation coefficient ≈ 0.6). During the quiescent phase, the edge pressure gradient continuously increases until the plasma transits back to the L-phase. A larger pressure gradient is possible at higher current. The pressure gradient at the end of a quiescent phase is larger than the average pressure gradient during a subsequent phase with ELMs. The variation of the edge pressure gradient in quiescent phases (either by changing the current or the distance to the wall) is mostly due to changes in density and not so much to changes in temperature gradient. Results are shown in Fig. 21.

2.4. Impurity development in the H-mode

As summarized in Section 2.2, the development of the impurity concentration in an H-discharge depends on many factors, such as the reduced wall erosion in the H-phase and the changed confinement and MHD characteristics [20, 21]. Figure 22 plots spectroscopic traces, representing the influx of oxygen and iron,

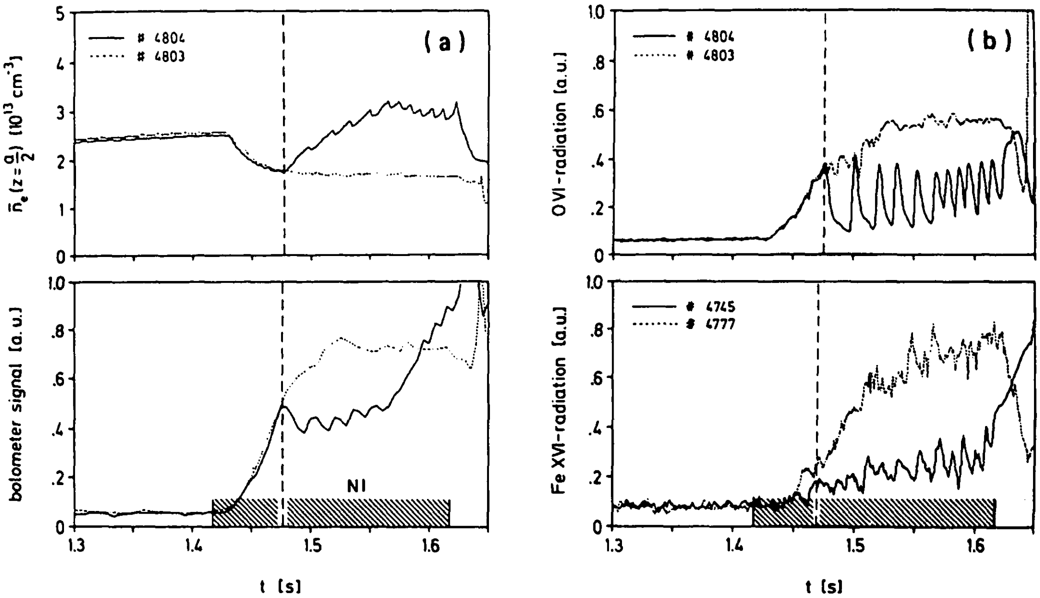

FIG. 22. (a) Plasma radiation from L- and H-type discharges as measured by a bolometer. The signal is divided by the plasma density. The line averaged density is also plotted for reference. (b) Radiation of O VI and Fe XVI, normalized for the plasma density from the two discharge types. The dashed lines indicate the L–H transition.

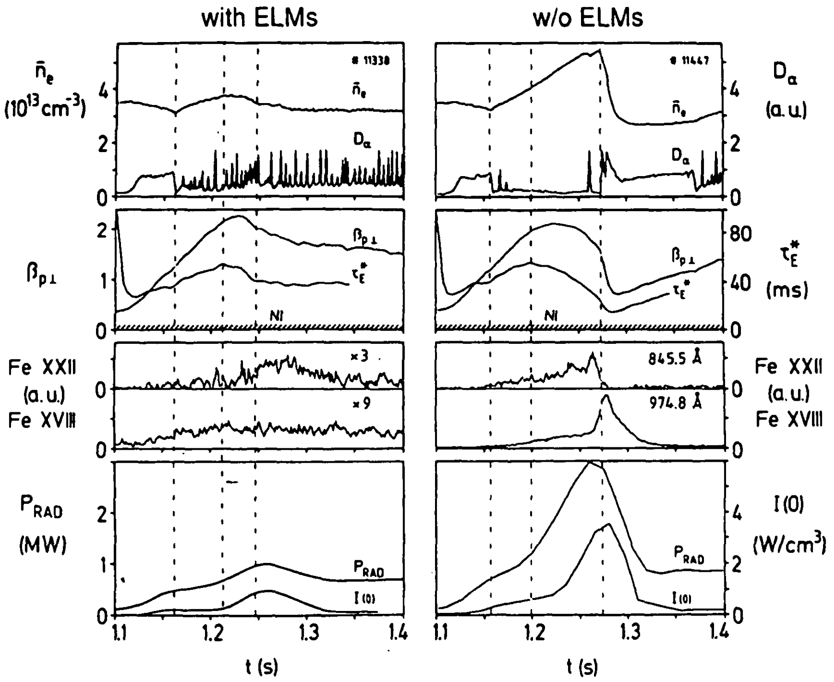

FIG. 23. Time evolution of various plasma parameters of H-mode discharges with and without ELMs (I_p = 0.32 MA, B_t = 2.17 T, P_{NI} = 3.3 MW, $H^0 \rightarrow D^+$): line averaged plasma density $\bar{n}_e$, D_α light intensity in the divertor chamber, poloidal beta β_p, global energy confinement time τ_E^*; Fe XVIII and Fe XXII line intensities (representative of iron radiation from r/a $\simeq$ 2/3 and from the plasma centre, respectively), and total and central radiation losses P_{RAD} and I(0).

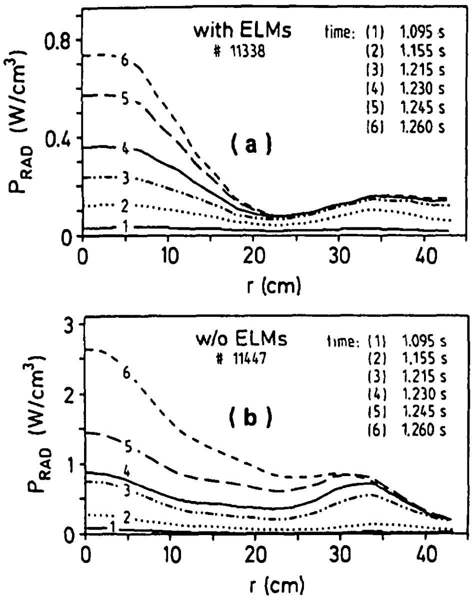

FIG. 24. Radiation power density profiles of (a) an ELM dominated H-discharge and (b) an ELM free H-discharge.

together with the line averaged density and the total radiation power. The radiation and spectroscopic data are normalized to the line density in order to demonstrate the effect of the impurity influx. The normalized intensities decrease after the L–H transition for both oxygen and iron; the decreased impurity influx after the L–H transition is also shown by the total impurity radiation, which, however, increases in the course of the H-phase to levels higher than those in the L-phase (even when normalized to the density). The increase in radiation is stopped when beam heating is termined. The rise in impurity radiation during the H-phase is caused by the improved confinement, which also affects the impurity ions. In particular, the absence of sawteeth in the plasma centre makes this zone susceptible to impurity accumulation. The outer zone is affected by ELMs, and the impurity development of the discharge depends very much on their presence and intensity. In Fig. 23, a discharge without ELMs is compared with a long discharge (beam stacking) with ELMs. In this section, we are interested only in the development of the impurity radiation and the energy content. Without ELMs, impurities quickly accumulate in the plasma centre, causing the total radiation and, in particular, the central radiation to increase. In the plasma centre, since there are no sawteeth, the inward flux of impurities is not stopped. The increased impurity radiation causes a saturation of the energy content of the discharge and a roll-over in β_p; finally, a forced transition back to the L-mode occurs.

In contrast to a quiescent discharge, in a discharge with ELMs the central radiation losses do not exceed a level of 0.8 W$\cdot$cm^{-3} and the discharge becomes stationary for more than 1.3 s. The development of the radiation profiles in cases with and without ELMs is shown in Fig. 24. The two profiles evolve in a similar manner until they have centrally peaked shapes; the absolute values, however, differ by a factor of about three. This difference in the absolute radiation is also found during the preceding L-phase, and in the case leading to a quiescent H-phase it is essentially caused by larger contamination. These discharges were produced by shifting the plasma 4 cm towards the outer stainless-steel protection limiters, thereby reducing the scrape-off region to a width of about 3 cm [21]. Furthermore, by means of laser blow-off injection of metals into the H-phase the suppression of ELMs could also be demonstrated [22]. The increased radiation can lead to a reduction of the pressure gradient in the edge region, thus eliminating the driving force of the ELM instability. Relatively high-Z elements (Cr, Ti), however, are needed to quench the ELM activity. Puffing of neon and methane, for instance, which radiate preferentially close to the separatrix, has the opposite effect: the ELM frequency is increased and it is even possible to fully restore the L-phase in this way (see Section 6.1.1). A similar response is observed in the case of hydrogen puffing or in cases where high recycling conditions in the main plasma chamber are established.

The development of the central iron concentration, $n_{Fe}(0)/n_e(0)$, in H-discharges with and without ELMs

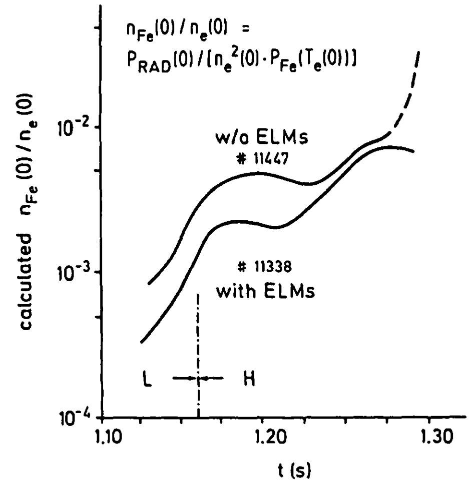

FIG. 25. Temporal evolution of the iron concentrations at the plasma centre, calculated from the central radiation density and the temperature dependent radiative power loss function of iron (see inserted formula).

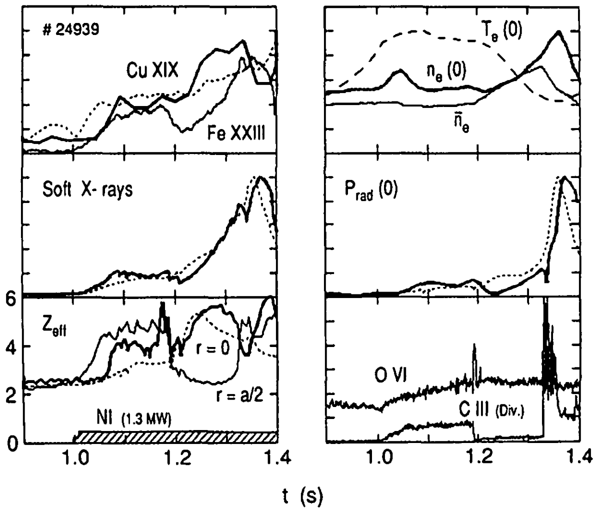

FIG. 26. Various signals as a function of time for a discharge in the new divertor configuration DV-II, exhibiting a quiescent H-mode in the period 1.18 ≤ t ≤ 1.34 s. Results of simulation calculations are plotted as dotted lines.

is shown in Fig. 25. These concentrations are derived from measured radiation densities, $p_{rad}(0, t)$, and from calculated radiation rates, $L_{Fe}(T_e)$, on the assumption that iron is the dominant metallic impurity ($p_{rad} = L_{Fe} n_{Fe} n_e$). We notice that although the radiation densities differ by factors of three to five, the concentrations are almost equal at the time when the quiescent discharge starts to collapse. The large difference in radiation losses is mainly due to the higher electron density (factor of ~2.5); additionally, the decrease of the temperature in the late quiescent phase causes a further increase of the radiation.

So far, the ELM activity has been taken to be only an indication of low metallic influxes. It is found, however, that ELMs also lead to improved impurity screening efficiency in the edge region. This is inferred from the observation that in all discharges with varying ELM frequency the central radiation is inversely correlated with this frequency, but with a delay of typically 50 ms, i.e. approximately the diffusion time. In these cases there is no reason to assume a changing influx of impurities across the separatrix. Further support for the screening effect of ELMs is obtained from experiments with constant low argon gas puff rates [20]. In discharges with ELMs the argon density in the main plasma is seen to saturate after about 100 ms, whereas it steadily increases in quiescent discharges. The opposite behaviour is found in the divertor region where the argon density increases in discharges with high ELM frequency, which indicates impurity retention, but during quiescent phases the argon density is constant.

Attempts to simulate the impurity behaviour during the quiescent H-phase were initially based on anomalous transport modelling. However, no unique description of the transport parameters can be derived from the measurements and different transport formulations can lead to similar results. Nevertheless, it was found necessary to reduce the anomalous diffusion coefficient D_{an} by a factor of about four and to postulate substantial inward drift velocities in simulations of the L-H transition [20]. On the other hand, a consistent analysis of the accumulation of metallic impurities in various regimes of improved confinement in ASDEX [22] is possible by invoking a combination of neoclassical transport and anomalous diffusion. Thus, it can be concluded that impurity accumulation is simply the result of a reduction of the anomalous diffusion coefficient by which the outward fluxes are decreased.

In the following, we apply this concept of impurity transport to the analysis of a more recent discharge in the new divertor configuration DV-II, where quiescent H-phases of up to 160 ms are achieved. This configuration has better diagnostics than the previous one and, in particular, 16-channel Z_{eff} measurements (infrared bremsstrahlung) as well as good time and space resolved T_e and n_e profiles are available. Some of the relevant signals are plotted in Fig. 26. The global parameters are: I_p = 380 kA, B_T = 2.2 T, neutral beam heating (1.3 MW D^0 in D^+) for 1.0 ≤ t ≤ 1.8 s and slightly carbonized walls. The L-H transition occurs at 1.18 s and the transition back to the L-mode occurs at 1.34 s, as is clearly seen from the C III divertor radiation signal shown in the lower right corner of Fig. 26. In the H-phase, the line averaged electron density (upper right corner of Fig. 26) steadily increases to a maximum of 6.3×10^{13} cm^{-3} and, simultaneously, the central density rises, reaching its maximum of 9.0×10^{13} cm^{-3} during the second L-phase. In contrast, the central electron temperature decreases from a maximum of $T_e(0)$ = 2.5 keV during the first L-phase to 1.1 keV at the end of the H-phase. Similarly, the poloidal beta reaches a maximum of 1.5 at t = 1.27 s and thereafter decreases because of the rapidly increasing radiation losses (at t = 1.3 s: $P_{in,tot}$ = 1.6 MW, $P_{rad,tot}$ = 1.3 MW). Also shown in Fig. 26 are the spectroscopic signals of O VI, Cu XIX and Fe XXIII along central chords. The O VI signal is emitted close to the separatrix and is representative of the influx of oxygen, which is seen to be fairly constant for t > 1.15 s. The Cu XIX radiation is preferentially produced at r = 30 cm; this signal is determined by influx as well as transport. Core radiation is represented by the Fe XXIII signal and particularly by the soft X-ray intensity. In addition, the development of Z_{eff} on axis and at the half minor radius is shown in the lower left corner of Fig. 26. The total central radiation losses are also plotted; they reach a maximum of 4.5 $W \cdot cm^{-3}$ during the second L-phase. The results of our transport calculations for copper (the new target metal in the divertor) are indicated by the dotted lines in Fig. 26. The calculations are based on the following assumptions: The influx of copper at the onset of neutral injection rises by a factor of ten during $1.0 \leq t \leq 1.05$ s and then stays constant at a level of $\phi_{Cu} = 1.5 \times 10^{19}\ s^{-1}$ (6×10^{13} atoms/$cm^2 \cdot s$). The anomalous diffusion coefficient D_{an} changes from a constant value of 0.9 $m^2 \cdot s^{-1}$ during the L-phase to 0.1 $m^2 \cdot s^{-1}$ during the H-phase. This reduction takes place in the whole inner region, $r \leq a$, but not in the SOL zone, $r > a$. In this way, reasonable agreement is obtained (in absolute scale) with the measured Cu XIX intensity ($I_{Cu,max} = 0.023\ W \cdot cm^{-2}$). For comparison with the soft X-ray data, the contribution of iron, which, according to VUV spectra, is about equal in concentration, must be added. We thus obtain 70% of the detected SX intensity ($I_{SX,max} = 7.5\ W \cdot cm^{-2}$). Normalizing the calculated and measured SX traces yields the agreement shown in Fig. 26, which is satisfactory. At the time of maximum poloidal beta the central metallic concentration $(n_{Cu} + n_{Fe})/n_e$ is again 0.5%.

For the estimation of Z_{eff}, additional assumptions with respect to the behaviour of the light elements O and C must be made. As a first approximation, we ignore accumulation effects and take the contribution of O and C as measured during the Ohmic phase, i.e. $Z_{eff}(0) - 1 = 1.3$. When the calculated Cu and Fe parts are added, the dotted curve plotted in the lower left corner of Fig. 26 is obtained. The agreement with the measured values (bold curve) for $r = 0$ is not satisfactory in detail, but the systematic trends and also the rather high values of $Z_{eff}(0) \approx 5$ are consistently reproduced. The measured Z_{eff} traces demonstrate the impurity accumulation by the inverse behaviour of $Z_{eff}(0)$ and $Z_{eff}(a/2)$. From intermediate Z_{eff} channels the actual accumulation region is found to be a small core zone within $r \leq 12$ cm. It is also this region where a sharp rise in Z_{eff} is detected immediately before the transition to the H-phase (see Fig. 26). This can be explained by (1) the existence of poloidal asymmetries caused by the sawteeth that trigger the L-H transition, and (2) the occurrence of marfes in the torus midplane. Furthermore, it should be noted that the high central Z_{eff} is of little importance for the volume averaged quantity $\bar{Z}_{eff}$, which enters into the ratio of the plasma current to the loop voltage. In fact, calculating $\bar{Z}_{eff}$ from the corresponding profile measurements yields a relatively low value of $\bar{Z}_{eff} \sim 3.2$ for the H-phase, whereas $\bar{Z}_{eff}$ is as high as 4.5 during the preceding L-phase.

It has been found that the exceptionally good confinement properties of the quiescent H-mode cannot be utilized to achieve a maximum plasma energy content. In particular, the metallic influxes from the divertor target plates (Ti, Cu) and additional fluxes from the walls (Fe) under non-carbonized or poorly carbonized conditions are too large to keep the central radiation losses at tolerable levels when accumulation occurs. As in other improved confinement regimes, the impurity accumulation process can be understood by neoclassical inward drifts, which become essential when anomalous diffusion (caused by turbulence under degraded conditions) is suppressed. Although these inward velocities are lower in the present case than, for example, in the case of neutral counter-injection, where the accumulation is strongly increased by the marked peaking of the proton profile [23], they are still high enough ($v_{Fe}(a/2) = 0.8\ m \cdot s^{-1}$) to produce dangerous core concentrations, of the order of 0.5%, within about 0.1 s. In addition

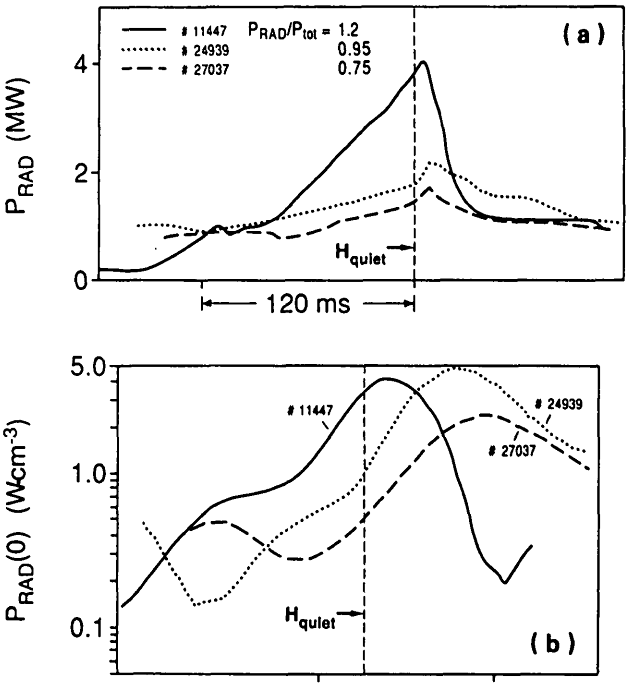

FIG. 27. *Total radiation (a) and central radiation density (b) for three quiescent H-phases with various divertor configurations: Solid lines: DV-I, closed configuration; dotted lines: DV-II, open configuration; dashed lines: DV-II, closed configuration. The traces are shifted along the time axis such that the H-L transition occurs at the same time point.*

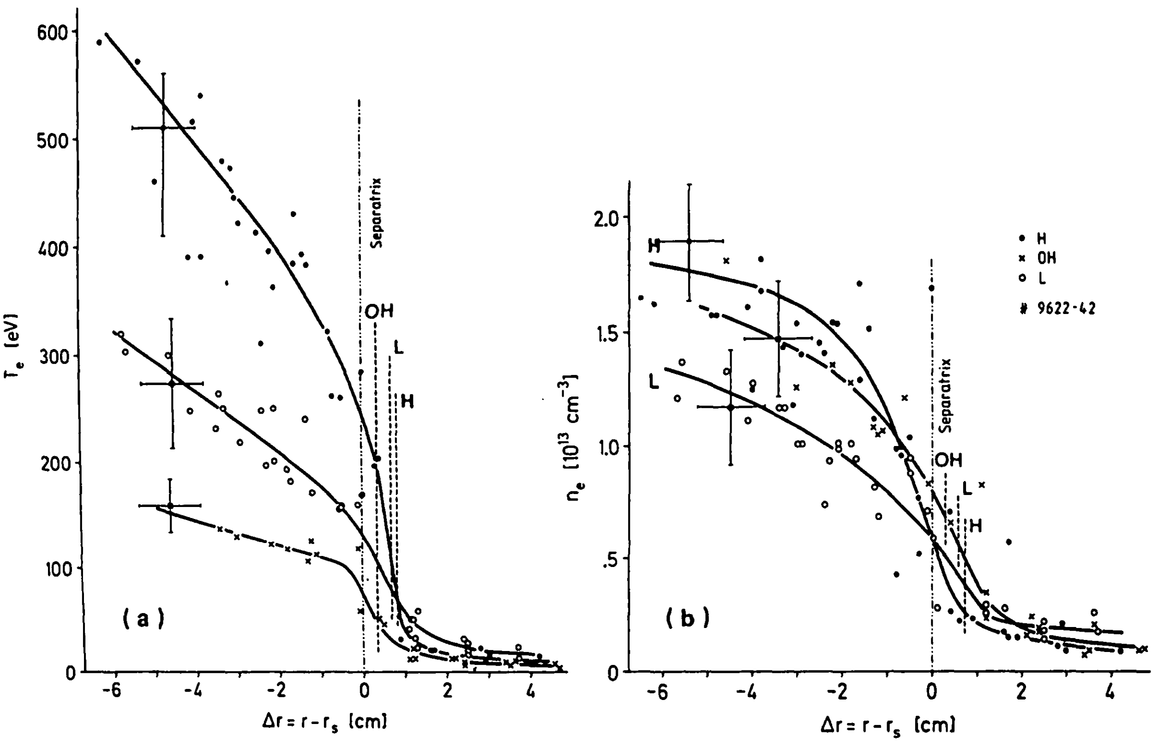

FIG. 28. Radial profiles of (a) T_e and (b) n_e, in the midplane over the separatrix, for ohmically heated and beam heated discharges; $r = r_s$ is the nominal separatrix position according to magnetic signals. Vertical bars indicate separatrix positions determined from electron pressure profiles in the divertor chamber using the assumption that n_eT_e = constant along field lines. The question of the exact location of the separatrix is discussed in the text.

to accumulation of metals, central accumulation of light elements cannot be excluded and may lead to a further dilution of the proton/deuteron density. Information on this important aspect is expected from charge exchange resonance measurements of C VI and O VIII which are planned for the near future. However, it should be emphasized again that in H-modes with ELMs it is possible to achieve steady state operation with constant poloidal beta, acceptable impurity levels (Fig. 23(a)) and superior energy confinement compared with that in the L-mode (see Section 3.4.6).

We have studied the sudden termination of the quiescent H-phase during beam heating with various divertor configurations (see Section 4.2) which lead to different developments of the total and central impurity radiation, as shown in Fig. 27. The solid curve is obtained in the initial divertor configuration DV-I of ASDEX, and the dotted and dashed curves are obtained with the new divertor topology DV-II, under open and closed conditions, respectively. (The curves are shifted along the time axis such that the termination points for the quiescent H-phases coincide.) Comparison of the impurity development shows that the end of the H-phase does not coincide with the maximum of total or central radiation. The maximum radiation occurs after the H*-L transition. This delay is rather distinct in the new divertor configuration and is obviously connected with the rapid shrinking of the density profile in the L-phase. The actual reason for the sudden termination of the quiescent H-phase and the transition to a second L-phase is not yet clear. The increased radiation level does not seem to be the only reason for it. A possible cause is the continuously rising edge pressure; the transition to the second L-phase is initiated by an ELM.

2.5. Scrape-off layer and divertor plasma parameters

Various specific diagnostics are available in ASDEX for edge and divertor investigations. The edge electron density and the temperature in the equatorial plane can be measured by using the Thomson scattering system at the edge. The H-mode profiles of T_e and n_e at the plasma edge are plotted in Fig. 28 together with L-mode and OH results. As the diagnostic is limited to five observation channels which are spatially fixed, the horizontal plasma position was shifted from discharge to discharge in order to increase the spatial range and

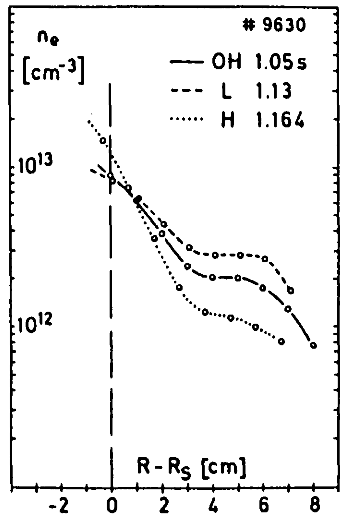

FIG. 29. Density profiles in the SOL during the Ohmic phase, the L-phase and the H-phase. $H^0 \rightarrow D^+$, P_{NI} = 2.8 MW, B_t = 2.17 kG, I_p = 315 kA.

the number of data points. In the scrape-off layer (SOL) outside the separatrix the statistical error increases because of the low scattered light intensity and also because of plasma fluctuations (laser pulse length ≈ 20 ns). Note the high edge electron temperature (~600 eV) a few centimetres inside the separatrix and its steep gradient. The H-mode in these measurements exhibited ELMs; the data shown in Fig. 28 therefore represent average values, as observed in discharges with ELMs.

The separatrix position shown in Fig. 28 has been determined from the signals of flux loops and magnetic probes ('nominal' position). Its uncertainty of about ±1 cm is comparable to the radial decay length, causing a significant error in the plasma parameters at the last closed surface. Previously, the separatrix position was also determined from the measured pressure profile in the divertor plasma fan as well as the momentum balance along the field lines between midplane and divertor, i.e. with approximate pressure constancy [24]. This procedure yields a separatrix position shifted to the outside by ~1 cm, as indicated in Fig. 28. At the nominal separatrix position, a suprisingly high temperature is found especially for the H-phase; to obtain consistency with the measured total power deposition in the divertor chamber, a substantial thermal barrier on open field lines would have to be assumed. Taking the pressure corrected separatrix position in Fig. 28, one obtains values much closer to those expected from numerical edge models including a flux limited electron energy transport into the divertor. There is additional evidence that the actual separatrix position is shifted further out, for example by the instant X-ray emission which occurs when a small target is moved across the separatrix under plasma conditions where a fast electron minority is present, as during lower hybrid heating or current drive [18].

Despite the experimental scatter of the data in Fig. 28, it is obvious that the radial decay lengths of the density and temperature in the H-phase are much shorter than those during L- and OH-phases. From detailed studies of the actual separatrix position we conclude that a radial zone of large density and electron temperature gradients is located at, but inside, the separatrix. The exact location of this zone with respect to the separatrix is of decisive importance for H-mode theory.

In addition, continuous radial edge electron densities with high time resolution and accuracy can be derived from measurements of the intensity of light emitted from Li atoms which are impact excited by electrons and ions in the SOL. For this purpose, the Li beam is injected perpendicularly to the plasma surface in the outer midplane; the Li(2p–2s) emission profile along the beam is measured at ten spatial points spanning 9 cm [25]. Figure 29 compares the radial dependence of the electron density in the Ohmic phase, the pre-transition L-phase and the quiescent intervals between ELMs in the H-phase. Most pronounced is the large variation in the density e-folding length λ_n near the separatrix, which ranges from ~2.1 cm in the OH-phase to ~2.8 cm in the L-phase and to ~1.2 cm in the H-phase. A few centimetres further out, a more or less clear plateau is obtained in a region where the electron temperature has fallen below the ionization level everywhere along the field lines. Qualitatively, these changes are related to changes in plasma confinement: λ_n is largely determined by the cross-field diffusion in the SOL and by the transit time for particles between the midplane and the divertor target plates. Thus, a decrease of λ_n in the H-phase reflects a reduction of the cross-field transport coefficient, and, conversely, an increase of λ_n during the L-phase is correlated with increased perpendicular particle transport. Assuming a parallel flow, with Mach number M ≈ 0.2 as a first approximation to a SOL with divertor recycling, we obtain D ≈ 4000, 10000 and 1500 cm^2·s^{-1}, respectively, for the OH-, L- and H-phases in the strong gradient part of the SOL.

Another important aspect of the SOL density profile during the H-phase is its invariance with respect to global plasma properties. Figure 30 illustrates the temporal behaviour of the density at the nominal separatrix, n_s, and of the density e-folding length over

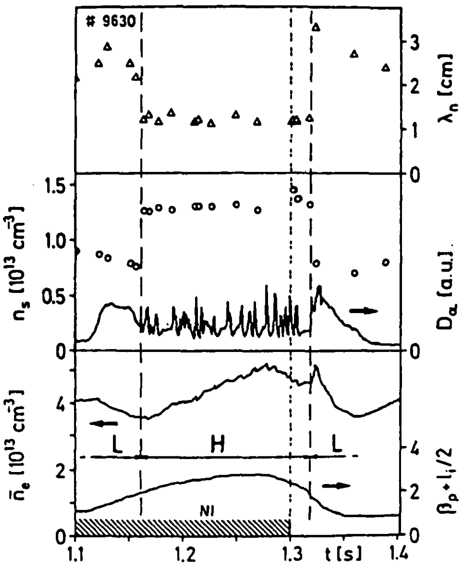

FIG. 30. Temporal behaviour of $\beta_p + \ell_i/2$, the line averaged density $\bar{n}_e$, the D_α light intensity of the divertor plasma, the separatrix density n_s, and the density e-folding length λ_n in the SOL during and after neutral injection, for the discharge of Fig. 29.

a time span of 400 ms for the discharge considered in Fig. 29. Upon attainment of the H-phase, n_s and λ_n exhibit no time dependence, even though $\bar{n}_e$ increases from ~3.4 × 10^{13} to 5 × 10^{13} cm^{-3} and $\beta_p + \ell_i/2$ increases from ~2 to 2.8. The density profiles in the SOL during the H-phase are extremely invariant. This is particularly striking, since the geometric position of the nominal separatrix shifts over a range of 2 cm as a result of the increase in poloidal beta and the plasma position control.

The constancy of the H-mode SOL profile is sporadically destroyed by ELMs, which are associated with a catastrophic breakdown of the transport barrier. In less than 200 μs, particles are released into the SOL and lead to an increase in λ_n by a factor of more than four. Subsequently, λ_n decays to the pre-ELM values with an exponential time constant of ~0.5 ms. Within a few milliseconds, the SOL density profile reassumes its pre-ELM state in both λ_n and n_s.

The relative behaviour of λ_n in the various phases shown in Figs 29 and 30 is universal. A limited database, selected for its parameter extremes ($\bar{n}_e$ = (1.8-5) × 10^{13} cm^{-3}, I_p = 220-415 kA, B_t = 16.7-25.1 kG and P_{NI} = 2.4-3.4 MW), shows that $\lambda_n(L)/\lambda_n(OH) \sim 1.3 \pm 0.27$ and $\lambda_n(H)/\lambda_n(OH) \sim 0.7 \pm 0.12$, with single-null discharges having lower values of $\lambda_n(L)$. With this database, it is found that for injection power levels which eventually lead to the H-mode, $n_s/\bar{n}_e$ remains roughly constant in both the Ohmic phase and the L-phase, i.e. the global density profiles exhibit self-similarity in the parameter $n_s/\bar{n}_e$. Since for the DV-I divertor configuration, $\bar{n}_e$ always decreases during the L-phase, n_s decreases as well. In contrast, at the onset of the H-phase, $n_s(H) \propto \bar{n}_e^{2.2}/P_{tot}^{2.5}$ ($\bar{n}_e$ in 10^{13} cm^{-3}; absorbed total power in MW). Hence, depending on the values of $\bar{n}_e$ and P_{tot}, $n_s(H)$ can be either greater than n_s in the L-phase (as in Fig. 29) or less than $n_s(L)$ for low densities and high injection powers. More details on the database are given in Ref. [26].

The SOL parameters in the midplane have to be compared with those in the divertor chamber. Figure 31 shows the location and the viewing angle and direction of several different diagnostics. The line integrated electron density in the SOL is measured interferometrically with a microwave system. The characteristic variation of the line density during the NI phase is plotted in Fig. 32 for an inner divertor chamber. During an L-discharge the line density increases until it reaches a maximum and then it decreases to the Ohmic level. At the L-H transition this decrease occurs quickly. Only recently, when an interferometer with a higher cut-off density became available on ASDEX, it became possible to measure the line density across the outer, denser divertor plasma fan. The qualitative signature obtained with this interferometer turns out to be similar to that

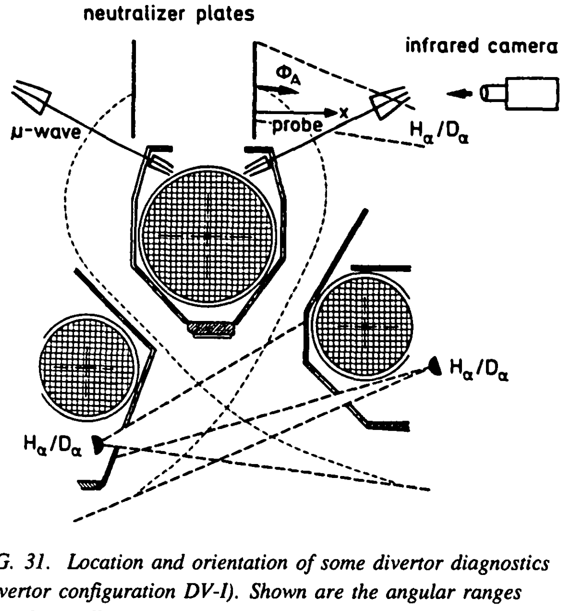

FIG. 31. Location and orientation of some divertor diagnostics (divertor configuration DV-I). Shown are the angular ranges viewed by different H_α/D_α monitors; the chord, sampled by the Langmuir probe; the location of inside and outside microwave horns used to measure the electron line density; the origin of the reflected flux ϕ_a at the intersection of the separatrix and the neutralizer plate; and the line of sight of the infrared camera.

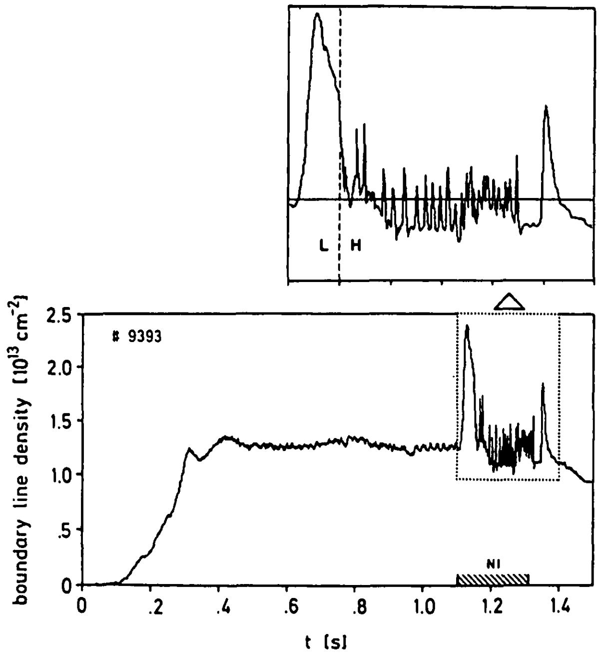

FIG. 32. Time dependence of the inner boundary layer line density; the NI phase is plotted on an expanded time-scale. $I_p = 0.3$ MA, $\bar{n}_e = 3 \times 10^{13}$ cm^{-3}, $P_{NI} = 3.0$ MW.

found previously, i.e. a sharp decrease of the line density at the L–H transition, sometimes followed by ELMs which cause a strong modulation.

The typical variation of the line density as described above and as shown in Fig. 32 can be analysed as a corollary of the particle confinement variation of the main plasma [27].

The electron temperature and density profiles in the divertor have been measured with Langmuir probes. Examples of these profiles, obtained on a shot-to-shot basis with a static probe in the different confinement regimes, are plotted in Fig. 33 for two different distances from the target plates. The profiles exhibit a sharp peak close to the separatrix, a rapid decrease at the inside, where the flux surfaces encompass the inner multipole coil, and a broad shoulder on the outside on flux surfaces which form the usual SOL. This shoulder is sharply cut off at a major radius of 173 cm because the flux surfaces at larger radii intersect the shields which form the divertor throat. This shoulder is obviously related to the somewhat less pronounced plateau observed in density profiles on the midplane (Fig. 30). The most important aspect of these measurements regarding confinement is the variation of the peak values, which rise from the Ohmic phase to the L-phase and then drop again to the low values of the Ohmic phase in the H-mode.

The power flow to the target plate is proportional to $n_t T_t^{3/2}$, where T_t and n_t are the values at the target. Taking the values measured with the probe at z = 87 cm, which is quite close to the target plate, we can estimate the variation of the deposited power for the different regimes, We come to the conclusion that the increase of the power flux into the divertor chamber in the L-mode is in rough agreement with the increase of the heating power, but after the L-H transition the power flux is sharply decreased although the heating power is the same as before.

Additional information on the divertor plasma parameters was obtained when the static probe in the divertor of ASDEX was replaced by a fast moving Langmuir probe. When this is operated in the triple mode, continuous profiles are obtained along a major radius line, as shown in Fig. 34 for L- and H-phases with ELMs. At a typical probe velocity of about 1 m·s^{-1}, many ELMs occur in the H-phase during one transit through the divertor plasma fan. Therefore, if the inidvidual ELMs do not significantly change, the lower envelope of each profile in Fig. 34 approximately represents the profile shape in the periods between ELMs, while the upper envelope, connecting

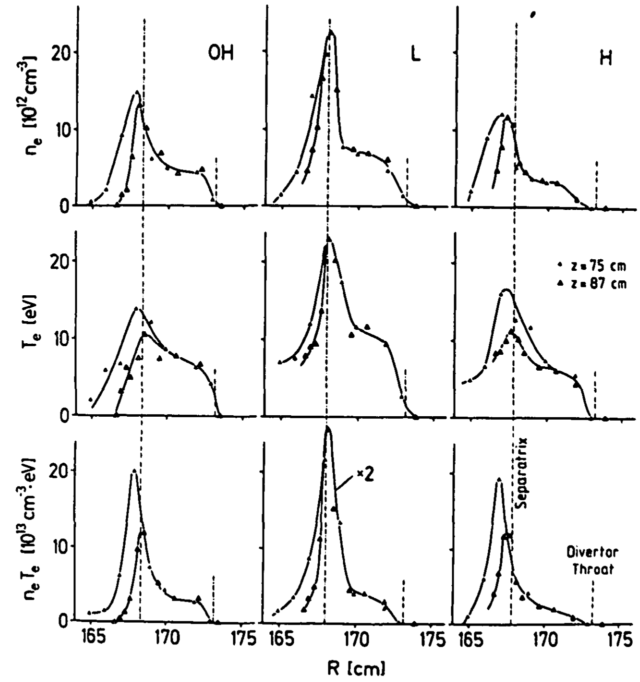

FIG. 33. Radial profiles of the electron density, temperature and pressure of a divertor plasma at two positions from the target plates, in the OH-, L- and H-phases. $I_p = 0.32$ MA, $\bar{n}_e = 3.6 \times 10^{13}$ cm^{-3}, $P_{NI} = 3.1$ MW.

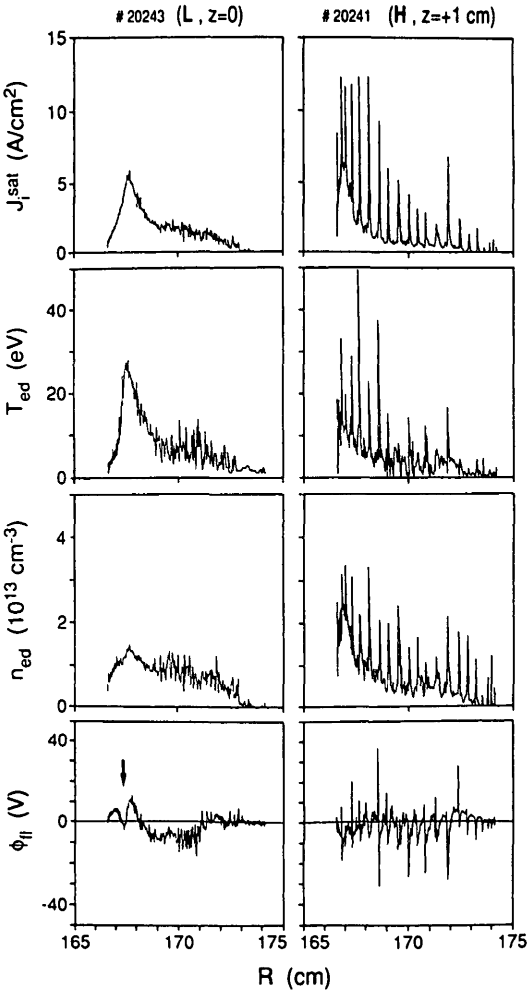

FIG. 34. Profiles of the divertor plasma fan taken with a fast moving Langmuir triple probe (velocity ≈ 1 $m \cdot s^{-1}$) along the major radius (ion saturation current, electron temperature, density and floating potential), assuming a Maxwellian plasma with a single temperature. Left: Unshifted L-discharge; the negative dip in the floating potential (arrow) is supposed to indicate the local separatrix position. Right: vertically shifted H-discharge (z = 1 cm) with regular ELMs.

the ELM maxima, roughly represents an average ELM profile. Comparing L- and H-profiles, it should be noted that the H-profile corresponds to an upshifted single-null divertor discharge, which is favourable for L–H transition, while the L-profile corresponds to an unshifted double-null configuration. An upshift usually causes nearly a doubling of the ion saturation current and density in the upper divertor. Except for such differences in the global discharge parameters, the main results of the static probe measurements are confirmed by the measurements with the Langmuir probe and additional information for ELMs is obtained. Their radial profile turns out to be even wider in the H-phase than in the L-phase. However, a quantitative analysis of the individual ELM parameters obtained with the Langmuir probe seems to be incompatible with details from other diagnostics measuring at different toroidal positions (see below). One reason for this discrepancy may be the strong asymmetry of the power flow during an ELM, as is discussed in more detail in Section 2.3.3. Another possible source of error is that the simple triple-probe theory used for interpretation may not be valid for such a highly dynamic event.

The results from the retractable Langmuir probe may also help resolve the question of the correct separatrix position in the divertor. The magnetically determined position is inaccurate within about ± 1 cm, as in the main chamber, and is frequently different from that determined with standard SOL models since, for example, it is located on the 'wrong' side of the profile maximum. However, it has been shown [28] that the floating potential profile in the divertor always exhibits a more or less pronounced negative dip roughly at the theoretically expected position inside the profile maximum. This dip is attributed to a hot electron minority which leaves the plasma very close to the separatrix without being reflected at the electrostatic sheath at the target plate. This dip therefore provides a direct, local determination of the separatrix together with the other triple-probe results. The dip in the floating potential is clearly seen on the L-profile in Fig. 34 (see arrow; left, bottom part). In the H-phase, the dip is often masked by ELM perturbations but, when the dip is well developed, it is at the expected position. Thus the observed location of the dip at a different position, which is sometimes especially pronounced in H-phases, seems to be an artefact, caused by errors in the magnetic measurements or by incomplete equilibrium models used for the determination of the magnetic configuration. Possible reasons are finite currents around the separatrix (e.g. near the X-point), which are usually omitted in the equilibrium codes, or even three-dimensional external magnetic error fields, as discussed in Section 2.3.3.

Instead of measuring the power load with the Langmuir probes, it can be derived from the temperature increase of the target plates during the discharge by using an infrared camera. The power deposition profile at the outer target plate is shown in Fig. 35, again for the three confinement phases, i.e. the OH phase, the L-phase and the quiescent H-phase (H^*) shortly after the transition. The highest power flux is about 100 W$\cdot$cm^{-2} in the Ohmic phase, 220 W$\cdot$cm^{-2} in the L-phase preceding the transition and only 35 W$\cdot$cm^{-2} in the H-phase.

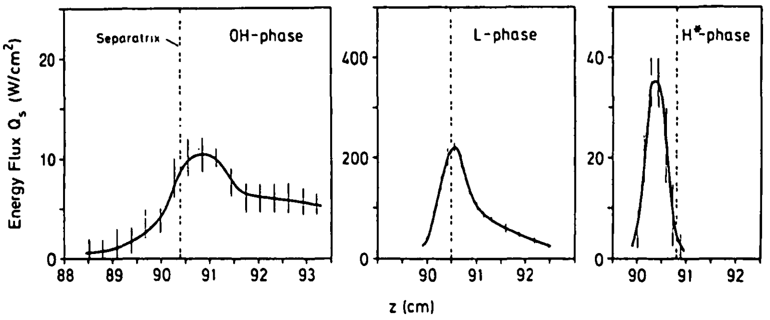

FIG. 35. Power deposition profiles at the upper outer target plate during OH-, L- and H-phases. P_{NI} = 3 MW.*

The total power deposited in the divertor chamber (deposition plus radiation) is 0.25 MW in the OH phase and increases to 1.85 MW in the L-phase. As expected, this variation is in agreement with the increase in heating power from 0.35 MW to 3 MW. It is, however, surprising that the power deposited in the divertor chamber in the H-phase is reduced to approximately the value found in the Ohmic phase, but at invariantly high heating power.

Ions from the main plasma which travel along the SOL impinge on the target plates and are partly reflected as atoms. According to the ion temperature at the separatrix, the bulk of the ions are in the energy range of 100 eV to a few hundred electronvolts and do not experience a large change in energy after reflection. The deposition of these ions from the main plasma can be measured by using a scanning charge exchange analyser. Figure 36 shows the deposition profiles of reflected particles in the L- and H-phases. The increase of the perpendicular diffusion coefficient D, which extends into the SOL (as revealed by the behaviour of the SOL density), leads to a broadening of the particle profile in the L-mode (compared with that during OH), and the decrease of D in the H-mode (between ELMs) causes the particle profile to shrink. In addition, the increase of the poloidal beta in the H-phase gives rise to a shift of the deposition maximum. From the measured energy of the particles, their residential time in the SOL can be calculated, using 15 m as the average path length from the plasma midplane to the target plate. A value of D which best fits the measured profiles is obtained by assuming diffusive perpendicular transport in the SOL. The following diffusion coefficients in the SOL are obtained: $D_{OH} = 4500\ \mathrm{cm^2 \cdot s^{-1}}$, $D_L = 8000\ \mathrm{cm^2 \cdot s^{-1}}$ and $D_H = 3500\ \mathrm{cm^2 \cdot s^{-1}}$. This agrees quite well with the values obtained from the analysis of the e-folding length λ_n.

The explosive nature of ELMs leads to an increase of the SOL fall-off length in the main plasma vessel, as observed with the Li beam diagnostic, and, as a consequence, to a broadening of the particle profiles in the divertor, as seen from the retractable Langmuir probe (Fig. 34). This feature is also confirmed by the power and particle deposition on the target plate, as shown in

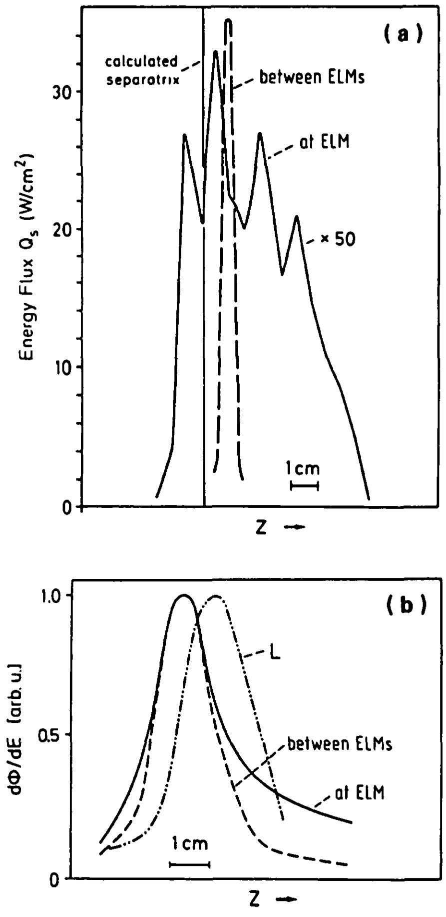

FIG. 36. Profiles of (a) the power flux onto the target plate and (b) the particles reflected from the target plates, during L- and H-phases, between ELMs and at an ELM. The displacement of the backscattering profiles of L- and H-phases is due to the higher vertical magnetic field in the H-phase. P_{NI} = 2.8 MW.

Fig. 36 in comparison with quiescent phases. The power deposition profile half-width, summed over 19 ELMs during a period of 120 ms (discharge No. 10817), increases to 5 cm; the profile wing is limited by the divertor aperture, indicating that some power is also deposited at the throat. The power deposition can reach peak values of several kilowatts per square centimetre; the total energy deposited during an ELM can be of the order of 10 kJ, i.e. of the order of 10% of the plasma energy content [29]. The power pulse length is about 0.4 ms, which is the time resolution of the camera. Soft X-ray signals indicate pulses as short as 0.1 ms. Using calorimetry in the new, water cooled divertor, a spatially fixed, sinusoidal average power deposition is found for the ELMs along the outer, upper target (Section 2.3.3). The infrared camera is located close to the deposition maximum, while the Langmuir probe and the divertor interferometer are, respectively, 90° and 180° away from it, which introduces some ambiguity in the comparison of the data from these different diagnostics. Nevertheless, even for qualitative agreement between the results, it is necessary to assume that strong local electric currents flow onto the target, in which case the electric sheath may be located in the electron collecting regime. For the fast ion deposition (Fig. 36(b)) the profile change is less dramatic, but the appearance of a broader shoulder is also evident.

In the quiescent H-mode the recycling of hydrogen changes, since the interaction of the SOL with the vessel wall is reduced. Furthermore, for a plasma with better particle confinement, less gas influx is required to maintain the same particle content and to compensate for the diffusive losses. In all regions of ASDEX where H_α monitors are positioned (they are uncalibrated and hence unsuitable for absolute determination of the ionization rate) the H_α intensity decreases at the L–H transition. The H_α radiation at locations important for recycling (divertor chamber and neck, stagnation point, typical wall section) is shown in Fig. 5. Because of the reduced recycling and the well localized ionization of hydrogen in the region with steep gradients, the plasma boundary is sharp and well defined in the H-mode. The transition to the H-phase can be easily demonstrated by a high-speed movie film.

3. CONFINEMENT IN THE H-MODE

3.1. Power fluxes in the H-mode

The power transported into the divertor chamber is the main power loss channel in the OH- and L-phases, in keeping with the anomalous radial heat conduction by electrons across the separatrix. The power flux into the divertor chamber is divided into radiated power via volume processes (impurity radiation and charge exchange losses) and power deposited onto the target plates. Another loss channel is impurity radiation and charge exchange whereby power is deposited onto the walls around the main plasma. Because of the high cleanlines of divertor discharges under both Ohmic and beam heating conditions, the impurity radiation power is small. The process of power transport from the main plasma to the divertor chamber is explained in terms of classical electron heat conduction along the magnetic field lines in the SOL. Thus, for plasmas under Ohmic and beam heating conditions in the L-regime, we have a consistent picture.

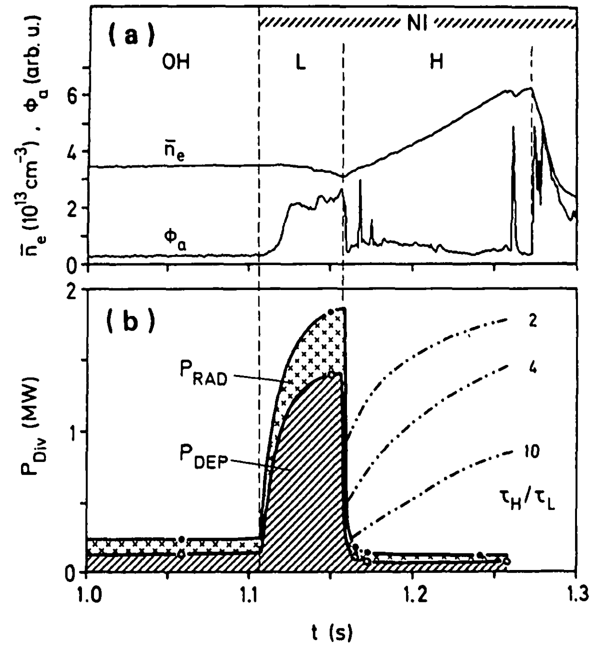

FIG. 37. Time development of (a) $\bar{n}_e$ and ϕ_a, and (b) the total power flow P_{Div} into the divertor chambers. The dash-dotted lines show the variation of the normalized transport losses for energy confinement time changes at the L-H transition (I_p = 0.315 MA, P_{NI} = 3.5 MW).

The situation is totally different after the L–H transition. At constant heating power, the power transported to the divertor chamber drops approximately to the Ohmic level at the transition. This rapid and surprising reduction of the power flux into the divertor chamber is plotted in Fig. 37, which shows both the power radiated from the divertor plasma and the power transferred to the target plates. This sudden decrease of the power flux into the divertor chamber is not due to a sudden deterioration of the magnetic configuration.

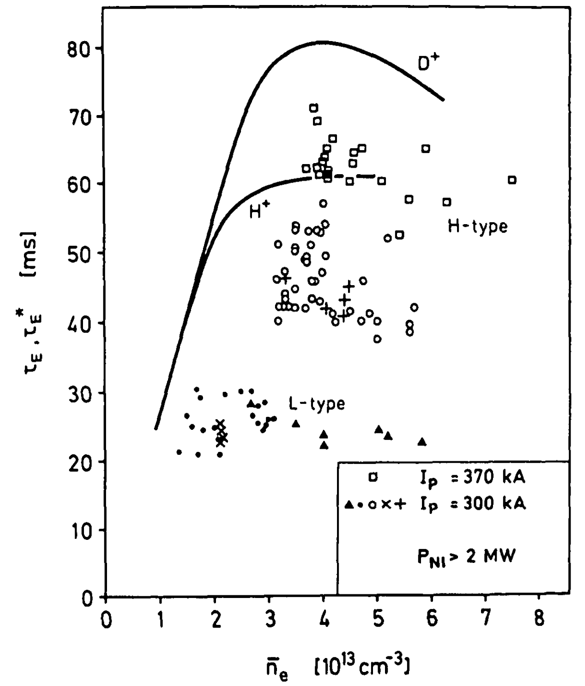

FIG. 38. Global energy confinement time versus line averaged density. The solid curves show the Ohmic relation for hydrogen and deuterium plasmas. The solid data points are L-type discharges (dots: divertor discharges, triangles: limiter discharges); the open symbols are H-type discharges at two different currents. Crosses denote τ_E values deduced kinetically; the other symbols are based on diamagnetic loop measurements (τ_E^*).

Particles and energy are still transported onto the target plates at the location where the separatrix is supposed to intersect them. The radial extent of the SOL is even reduced and the width of the deposition peaks shrinks, as shown in Fig. 35. However, as a consequence of the reduced power inflow, the parameters of the divertor plasma (density, electron temperature, H_α radiation) resume the Ohmic values (see Fig. 33).

In the periods between ELMs the power flux into the divertor chamber is also low. During ELMs the power seems to be transported in pulses into the divertor chamber. Taking an average over these pulses (e.g. with a bolometer), it is found that the radiated power within the divertor chamber is somewhat below that in the pre-transition L-phase and much above the level during a quiescent H-phase. Regarding the power accountability (ratio of the three loss channels, bulk radiation + divertor radiation + power to target plates, to the power input), there seem to be no serious problems during ELMs.

After a change in confinement, it must be assumed that a transient reduction of the power loss across the separatrix occurs. Within two to three confinement times, however, when the energy content of the discharge is built up and steady state conditions are restored, the power loss will be the same as before. The expected variations of the power flux into the divertor chamber are plotted in Fig. 37 for different confinement times. In contrast to expectations, the measured power loss remains low — at the level immediately after the L-H transition. The low level of the measured power flux across the separatrix cannot be explained fully by impurity radiation and by the power required to heat the plasma at the edge.

The precision of power accountability is 80-100% in the OH- and L-phases, but just after the L-H transition such a precision is not possible. At present, we can only assume the existence of a hidden power loss channel and we do not know its origin nor do we know the location where the missing power is deposited and the relevance of the power loss mechanism for the development of the H-mode. Possible reasons for the power loss are either asymmetries in the radiated power of the main plasma or toroidal variations of the power deposited in the divertor chamber (see Section 2.3.3). Hidden losses could be along drift orbits which allow particles to cross magnetic field lines and to 'disregard' the magnetic field topology. Such a loss channel may be opened up at the L-H transition, where even the plasma edge is collisionless or nearly so. It is possible that these losses are closely connected with the physics prerequisites for the L-H transition, as discussed in Section 6.

3.2. Global confinement

The global energy confinement time τ_E is in most cases determined from the poloidal beta (at its maximum or under steady state conditions), measured with a well compensated diamagnetic loop. The results are regularly tested with $\beta_p + \ell_i/2$, measured by the equilibrium coils, and with the poloidal beta of electrons, as provided in a quasi-continuous manner by the multipulse Thomson scattering diagnostics. In some cases, the ion temperature profiles are measured and then a full kinetic determination of β_p is possible. In numerous cases, transport analysis also provided a consistency check for many experimental data.

Figure 38 compares the τ_E values of H-mode plasmas at 300 and 370 kA with those of L-mode plasmas at 300 kA, for a heating power of >2 MW (H^0 injection into D^+ plasmas, H-mode with ELMs); the τ_E values are either from diamagnetic loop measurements or kinetically deduced from the profiles. At low density, an L-mode discharge with a divertor configuration may occur; at densities above 3×10^{13} cm^{-3}, only H-mode discharges develop. In this density range, the confinement times can only be compared with limiter data. At the same current, τ_E^H exceeds τ_E^L by a factor of two; τ_E^H increases with the plasma current (see Section 3.4), as in L-mode plasmas. Because of the scattering of the data (predominantly introduced by the irregular nature of the ELMs) a density dependence cannot be determined, but a steep or even linear density dependence — as in the low-density Ohmic phase — can be excluded.

In Fig. 38, the H-mode results are also compared with Ohmic data. For clarity, only smooth curves through the Ohmic data points are shown. The OH results are plotted for hydrogen and deuterium discharges. The high current H-mode results agree well with the saturated Ohmic values, and the $H^0 \rightarrow D^+$ data lie between the hydrogen and deuterium results in the OH-phase. Because of the difference in parameter scaling, the comparison of OH- and H-mode τ_E values has no physical meaning but simply serves to put the absolute values of τ_E into perspective.

The improved particle confinement at the L-H transition is obvious from the sudden increase in density, which leads to reduced or even zero external gas consumption. The plasma is then externally fuelled by the beams only. In the quiescent H-mode the rise in the density content is higher than the beam fuelling rate by a factor of about two to three; under these circumstances the plasma is refuelled by gas accumulated in the divertor chamber and the chamber walls. Figure 39 compares the line averaged density and the external gas flux of L- and H-discharges. During the L-phase the external gas flux is sharply increased, to counteract the density decrease that would occur without such an increase.

The absolute values of the particle confinement time in the different confinement regimes are difficult to assess. Particle transport will be discussed in separate sections, dealing with the transport analysis of the plasma in the core and boundary regions, and with impurity transport.

Here, we summarize the constituents of the particle balance equation for the different confinement regimes:

$$dN/dt = -N/\tau_P + \Phi_G + \Phi_B + \Phi_R \tag{2}$$

where N is the particle content within the separatrix, τ_P is the global particle confinement time of the plasma bound by the separatrix, Φ_G is the external gas flux through the valve, Φ_B is the fuelling rate of the beams and Φ_R is the recycling flux. In ASDEX the source of recycling is the amount of neutral gas stored within the divertor chamber and in its walls. The recycling flux is therfore approximated by

$$\Phi_R = N_0/\tau_D \tag{3}$$

where N_0 is the neutral particle content of the divertor chamber, and τ_D the confinement time of neutral particles in the divertor chamber, which is largely determined by the conductance of the divertor throats and possible by-passes.

Typical values for the components of Eq. (2) are listed in Table I; the quoted τ_P values have to be taken with caution, but they clearly demonstrate the drastically

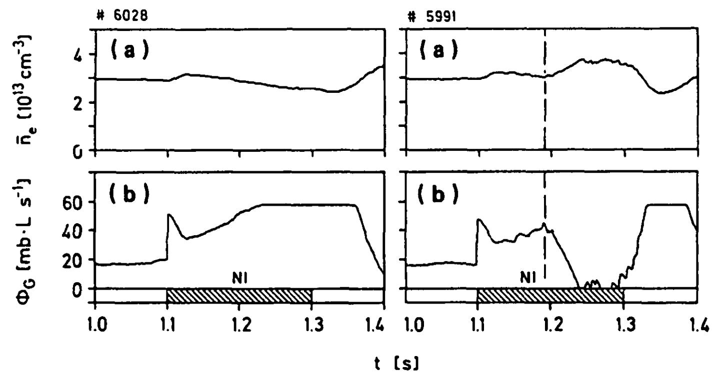

FIG. 39. Time dependence of (a) the line averaged density $\bar{n}_e$ and (b) the external gas flux ϕ_G, of L-type discharges (left column) and H-type discharges (right column). The dashed line indicates the transition from the L-regime to the H-regime.

TABLE I. ELEMENTS OF THE PARTICLE BALANCE EQUATION*

Phase	dN/dt (s^{-1})	Φ_G (s^{-1})	Φ_B[a] (s^{-1})	Φ_R[b] (s^{-1})	τ_p (s)
OH	0	10^{21}	0	2×10^{21}	0.05
L	0	6×10^{21}	8×10^{20}	2×10^{21}	0.01
H^*	2×10^{21}	0	8×10^{20}	2×10^{21}	0.15

* Particle balance equation:

$$\frac{dN}{dt} + \frac{N}{\tau_p} = \Phi_G + \Phi_B + \Phi_R$$

with N the particle content, τ_p the particle confinement time, Φ_G the external gas input, ϕ_B the beam contribution and Φ_R the recycling fuelling.

[a] Particle flux at 3 MW.

[b] The recycling flux is not well known.

improved particle confinement of the H-mode. The increase of the particle content in the quiescent H-phase is in rough agreement with the beam fuelling rate and the recycling flux as estimated for the Ohmic phase.

3.3. Transport analysis

To achieve a better understanding of the transport processes, we made detailed local analyses, with modified versions of the BALDUR simulation code and with the $1\frac{1}{2}$-D TRANSP analysis code, both developed at PPPL [30]. For these investigations we took the measured radial profiles of n_e, T_e, p_{rad} and Z_{eff} as well as computed power deposition profiles from the solutions of the equations for current diffusion, beam deposition and slowing-down of charged particles. The ion energy balance was solved without actual knowledge of the radial profile of T_i, but determining $T_i(r)$ under different model assumptions for the ion heat diffusivity $\chi_i(r)$, in an attempt to fit the results of active and passive charge exchange analysis and the integral constraints given by $\beta_{p\perp}$, $\beta_p^{equ} + \ell_i/2$ and the neutron flux. Besides providing checks on the mutual consistency of the measured data, this yielded radial profiles of the formally defined electron heat diffusivity, $\chi_e = -q_e/(kn_e\nabla T_e)$, using the TRANSP code, or radial profiles of T_e by applying models for χ_e, using the BALDUR code.

The main result of these studies is that the changes in the energy confinement, from the saturated OH (SOC) regime to the beam heated L-mode and then to the H-mode, are due to modifications in the electron and ion thermal transport losses (both conductive and convective):

— The conductive electron loss q_e and the electron heat diffusivity χ_e increase in the L-phase, while the electron heat conduction is the dominating loss channel. The increase in χ_e is pronounced in the initial phase when the beam is switched on. After the L-H transition, q_e and χ_e decrease (by a factor of up to two in ELM-free H^*-discharges) in the main plasma and, at least in ELM-free H^*-discharges, q_e approaches zero near the plasma boundary [31-36].

— The conductive ion heat loss q_i and the ion heat diffusivity χ_i increase slowly after the OH-L transition; this increase continues after the L-H transition. Even if χ_e is kept constant in the analysis during the H-phase, at the level of the preceding L-phase, q_i and χ_i are still found to increase after the L-H transition. Apart from radiation losses, the ion heat conduction becomes the dominating loss channel in the H-phase. The ion heat diffusivity in ohmically and additionally heated plasmas with 'flat' density profiles, having $\eta_i = (d \ln T_i/dr)/(d \ln n_i/dr) > 1$, can be formally described by the assumption of an enhanced (by a factor of two to four) neoclassical conductivity $\chi_{i,CH}$ as given by Chang and Hinton [35-38]. However, a combination of neoclassical and η_i-driven ion transport (see Ref. [127]) is also compatible with the T_i measurements in all discharge phases (SOC, L, H); moreover, it can explain in a consistent way the improvement of both the global and the ion confinement in peaked density discharges with $\eta_i \leq 1$ [39].

— The convective electron and ion losses increase during the temperature rise of the L-phase ($P_{conv}/P = 5/2\, \Gamma k\, (T_e + T_i)/(\Gamma\, \langle E \rangle)$), with Γ the particle flux and $\langle E \rangle$ the medium energy of the injected neutrals), especially in $D^0 \rightarrow D^+$ discharges with a reduced medium energy per injected nucleon and increased temperatures of the deuterium plasma (see Section 3.4.4). For $r/a < 0.7$, the dominant particle source comes from beam fuelling, whereas in the edge region the main particle source is due to the ionization of cold atoms. In this case, the total convective losses may become comparable to either the electron or the ion conduction losses. At the L-H transition the convection losses decrease because of the strongly reduced particle transport ($\tau_P > \tau_E$), which leads to an increase in the particle content and to a variation of the density profile shapes. In H^*-mode plasmas (density profiles are shown in Fig. 63), the energy is transported even towards the plasma centre by convection.

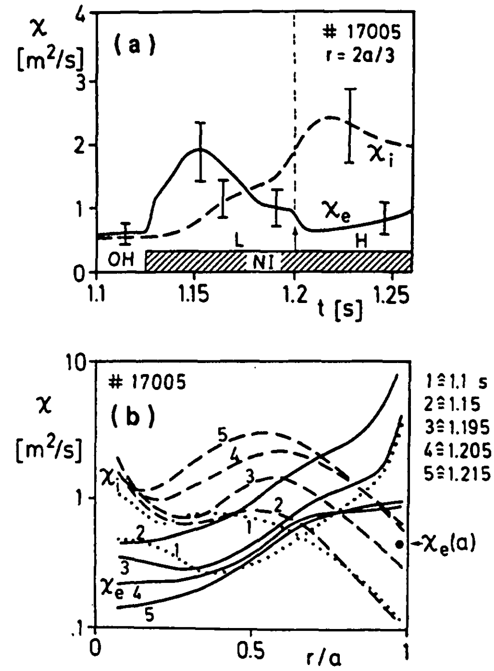

FIG. 40. (a) Electron diffusivity χ_e and ion heat diffusivity χ_i (= $\chi_{i,NC} + \chi_{i,\eta_i}$) versus time during consecutive OH-, L- and H-phases of a $D^0 \rightarrow D^+$ discharge.
(b) Corresponding radial profiles of χ_e and χ_i in the Ohmic phase (1), the L-mode (2) and at the L-H transition (3-5). The dots denote $\chi_e(a)$ deduced from the profiles of Fig. 28 in a quiescent H-phase.

We now analyse the local transport behaviour in more detail. Figure 40(a) shows the time dependence of χ_e and χ_i at r = 2/3a in the main confinement zone of a $D^0 \rightarrow D^+$ discharge, and Fig. 40(b) shows the corresponding radial profiles in the Ohmic phase, during the L-mode and at the L-H transition. The value of χ_e^H comes close to the χ_e^{OH} values, although the scalings are different. The central hump on the $\chi_e(r)$ curve in the Ohmic phase indicates losses due to sawteeth; these are not present in the H-phase. The data point $\chi_e(a)$ denotes the value of the electron heat diffusivity in the steep-gradient edge zone. The time dependences of χ_e at all radii show that the transition from the OH-phase to the L-phase occurs within a few milliseconds, which is — for the bulk region — shorter than the transition from the L-mode to the H-mode. The L-H transition is sharp in the outer plasma zone (r > 3/4a), where the transition obviously starts [34, 40]; q_e is strongly reduced. The density fluctuation studies are described in Section 6.3.1. It is interesting to note that these studies also indicate the existence of two time-scales: a rapid drop of the fluctuation amplitude at the edge and a gradual reduction of the amplitude in the bulk plasma. Since the confinement depends on the frequency of the ELMs, the deduced transport coefficients should be upper limits for the underlying quasi-stationary transport. In the quiescent H-phase (H^*) the electron heat diffusivity is even more reduced, but the central and global radiation losses increase during the quiescent phase, which leads to large errors in the determination of the transport coefficients.

The time behaviour of the effective heat diffusivity χ_{eff} for both electron and ion transport is in qualitative agreement with the χ_e behaviour illustrated in Fig. 40(a). Modelling the ion transport with a value of χ_{CH} that is increased by an appropriate factor (α = 2-4) in order to agree with the peak or the average ion temperature, the magnetically measured plasma beta and the neutron fluxes, yields only small changes in the resulting χ_i values at the L-H transition. After the L-H transition, however, the formally defined neoclassical enhancement factor α, which increases during the L-phase, is reduced again. The reproduction of the measured ion temperature profile shapes with the factor α is not satisfactory.

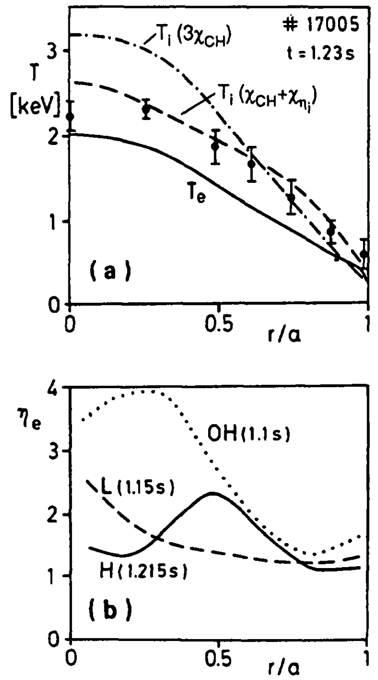

FIG. 41. (a) Radial profiles of T_e (measured with Thomson scattering) and of T_i simulated with $\chi_i = \chi_{i,CH} + \chi_{i,\eta_i}$ (given in Fig. 40) and 3 × $\chi_{i,CH}$, during the H-phase of a $D^0 \rightarrow D^+$ discharge. The points are T_i values measured in a passive CX neutral analysis of a comparable $H^0 \rightarrow D^+$ discharge with the same T_e profile but with 40% lower n_e values.
(b) Radial profiles of η_e = (d ln T_e/dr)/(d ln n_e/dr) during the OH-, L- and H-phases of the $D^0 \rightarrow D^+$ discharge of Figs 40 and 41(a).

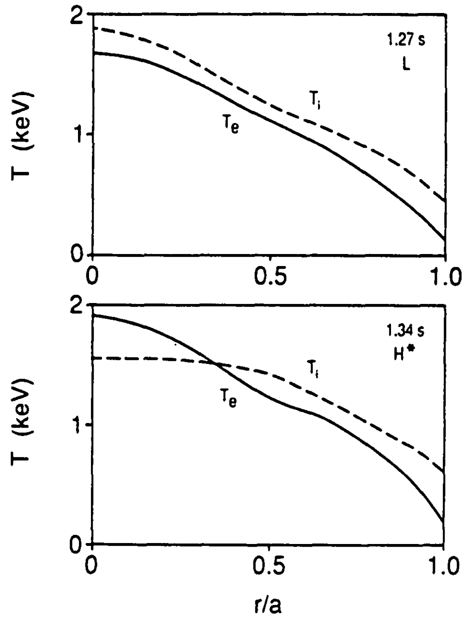

FIG. 42. Comparison of T_e and T_i profiles in quiescent L- and H-phases. The T_i profiles are determined from passive charge exchange flux spectra measured along five radial chords, in such a way that the deviations of the expected flux spectra from the measured ones are minimal over the full energy range.

Figure 41(a) shows the measured T_e profiles and the calculated T_i profiles during the H-phase of the discharge illustrated in Fig. 40, with $\chi_i = 3\chi_{CH}$ or $\chi_i = \chi_{CH} + \chi_{\eta i}$, respectively. The assumption of $\chi_i = 3\chi_{CH}$ yields a much too peaked T_i profile; this is also the case for L-mode discharges [39]. Since it was not possible to measure the T_i profile for the $D^0 \rightarrow D^+$ discharge with the passive charge exchange technique, we compare in Fig. 41(a) the simulated T_i profile with the measured T_i values (passive charge exchange) of a comparable $H^0 \rightarrow D^+$ discharge phase with the same absolute T_e profile and the same n_e profile but with a 40% lower $\bar{n}_e$ value. (This lower line averaged density explains the lower energy confinement time of the $H^0 \rightarrow D^+$ discharge.) The η_i-mode driven enhancement of χ_i yields agreement between the calculated and the measured T_i profile shapes, as is also the case for OH- and L-mode $H^0 \rightarrow D^+$ discharges. Figure 41(b) shows for the L- and H-phases the η_e profiles, which are close to the calculated and measured η_i profiles. Owing to the strong $T_i^{3/2}$ dependence, the latter χ_i model gives the increase in χ_i from the L-mode to the H-mode (see Fig. 40). However, the behaviour of the ion heat conduction losses is similar in the two χ_i models, since the increased χ_i values are counterbalanced by the reduced T_i gradients obtained with the η_i model.

Because of the difficulty of clearly determining the effects of the L-H transition on the ion transport, we have used the described comparison of $\chi_i = \alpha\, \chi_{CH}$ and $\chi_i = \chi_{CH} + \chi_{\eta i}$ also for ELM-free $H^0 \rightarrow D^+$ discharges. Basically the same results are obtained with the measured T_e and T_i profiles. Figure 42 shows these profiles at the end of the L-phase and 20 ms after the beginning of the H^*-phase.

A further and rather important indication that the ion transport is governed by η_i-mode driven strong turbulence even in the H-phase is the fact that the toroidal angular momentum diffusivities χ_ψ, derived from the measured toroidal rotation velocities (the momentum profiles are plotted in Fig. 43 for L- and H^*-phases), can be well described by the theoretical χ_ψ values based on η_i-mode driven turbulence for both L- and H^*-phases. It is important to note that there is a simultaneous improvement of both the ion energy and the toroidal momentum confinement in discharges with counter-injection of neutrals; in these discharges a peak of the density profile occurs which results in a decrease of η_i to less than 1 over a large part of the plasma cross-section. The experimentally and theoretically derived χ_i and χ_ψ values are correspondingly reduced compared with those in co-injection L-mode discharges [51]. The momentum confinement time τ_ψ increases from ~25 ms during the L-phase to ~40 ms during the H-phase, whereas, with counter-injection of neutrals, τ_ψ increases to 120 ms when χ_i drops to the neoclassical level.

Another example of transport analysis (based on the BALDUR code) of the pre-transition L-phase and of an ELM-free H-phase including the steep-gradient zone Δ close to the separatrix is given in Fig. 44 [41].

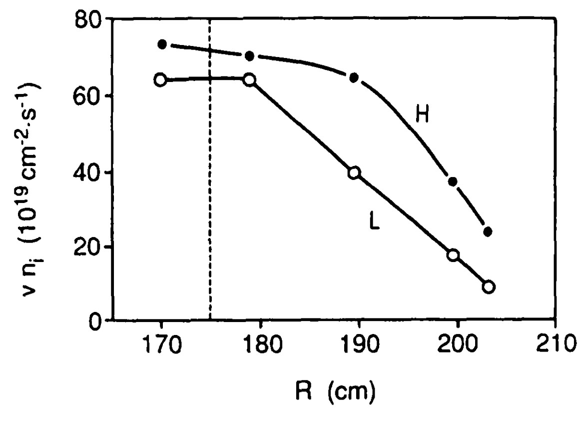

FIG. 43. Momentum profiles in the L- and H-phases measured by resonant charge exchange on O^{7+}.

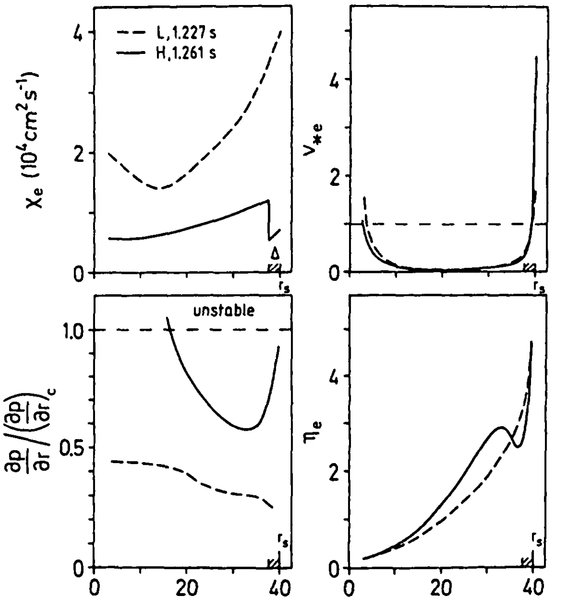

FIG. 44. Profiles of the electron heat diffusivity χ_e, the electron collisionality factor ν_{*e}, the ideal ballooning stability parameter $\partial p/\partial r/(\partial p/\partial r)_c$ and η_e (= d ln T_e/d ln n_e) in L- and H-phases.

The diffusivities χ_e and D in the zone Δ are strongly reduced in quiescent H-phases (see also Fig. 40(b)). An exact figure for χ_e cannot be given because the gradient length in the edge is comparable to the separation of the diagnostic channels; a factor of six may be typical. The confinement in the inner plasma has been shown to improve within 10 ms after the L-H transition (see also Fig. 40(b)). Figure 44 further shows the electron collisionality factor ν_{*e}, the ideal ballooning stability parameter, $(\partial p/\partial r)(\partial p/\partial r)_c$, and the profile parameter, η_e = d ln T_e/d ln n_e, for this simulation of an $H^0 \rightarrow D^+$ discharge.

Another objective of local transport analysis is the determination of the scaling relations for the electron heat diffusivity, the diffusion coefficient, the inward drift velocity and the ion heat diffusivity. Results from these studies [33, 39, 42, 43, 44] are presented in Section 3.4.7. Another important topic is the search for parameters that may be critical for the L-H transition and that may determine the operational limits of the H-mode [45, 46]. These points are closely related with attempts to identify the class of instabilities responsible for the anomalous fluxes in various confinement regimes. For the ions it is very likely that these instabilities are the η_i modes, as described above; for the electrons, however, no obvious instability could be determined so far (see Section 9).

Local transport and ballooning stability studies in H-mode plasmas have been carried out at the beta limit [38, 48, 49, 65]. It is found that the discharges below the beta limit exhibit H-mode transport and are stable to ideal ballooning modes. There is no gradual reduction of confinement when beta approaches the limit ('hard' beta saturation limit). The degradation of energy confinement at the beta limit is shown to be due to increased electron heat conduction and convection losses. The occurrence of these additional losses close to the ideal MHD limit suggests that kink and ballooning instabilities are responsible for them.

3.4. Scaling of the energy confinement time in the H-mode

This section deals mainly with the dependence of the global energy confinement time on various external parameters [52]. If not otherwise noted, the energy confinement times are deduced from the poloidal beta measured with the diamagnetic loop and refer to quasi-stationary states obtained by averaging over many ELMs. The agreement between the confinement times obtained from magnetic measurements (τ_E^*) and those calculated from measured plasma profiles (τ_E) has been checked; an example is shown in Fig. 39. No correction due to radiation is made, which is justified for H-discharges with a sufficient ELM frequency where the volume integrated radiation power losses are between 20% and 30% of the input power and come largely from the edge.

3.4.1. Density dependence

The density dependence of ohmically heated ASDEX discharges shows a linear increase of the global energy confinement time τ_E with $\bar{n}_e$ for lower densities ($\bar{n}_e \lesssim 3 \times 10^{13}$ cm^{-3}) and, in the saturated Ohmic confinement (SOC) regime, a levelling-off at higher densities, which is attributed to an increasing contribution of anomalous ion heat conductivity [50, 53]. In the improved Ohmic confinement (IOC) regime, τ_E continues to increase, up to the density limit [54]. For L-discharges as well as for neutral beam heated limiter discharges, however, τ_E is found to be largely independent of the plasma density. Contrary to the Ohmic case, however, the lack of $\bar{n}_e$ dependence is exclusively an electron transport property [31].

Experimental investigation of the density dependence in H-mode discharges is hampered by the large variation in the frequency of the usually observed ELM activity,

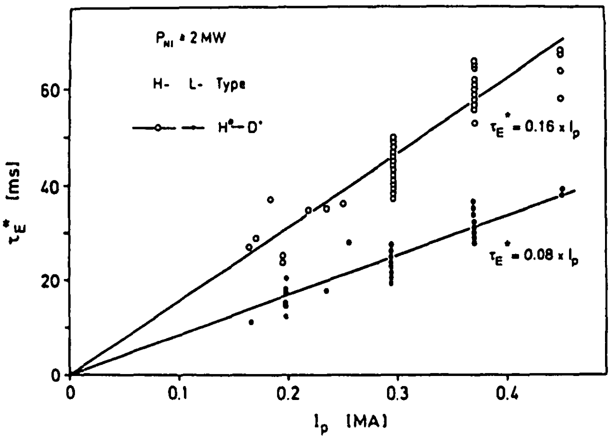

FIG. 45. Current scaling of the energy confinement time for D^+ target plasmas ($H^0 \rightarrow D^+$) in L- and H-modes.

which affects both particle and energy confinement. In cases where a quasi-stationary state, averaged over the ELMs, is obtained during the injection period, the deduced global confinement time does not show a marked $\bar{n}_e$ dependence over a wide range, within the uncertainty of the data (see Fig. 38). The interpretation of the non-stationary high density H-discharges is more complicated; high densities are obtained only by strong gas puffing during the short neutral injection phase, which, in turn, leads to a higher ELM frequency and therefore tends to reduce the τ_E values. At densities above (7–8) × 10^{13} cm^{-3}, only L-discharges seem to be possible with gas puff refuelling. A precise classification of the discharges into L-modes and H-modes is not always possible because the density together with the H_α radiation increase sharply and transitions may escape observation. Phases without any ELMs, on the other hand, are governed by a long particle confinement time (see Section 3.2). To what extent the energy confinement time of the quiescent H-phase exhibits a density is still not known.

3.4.2. Current dependence

An important new parameter which enters the scaling of neutral beam heated plasmas in ASDEX as well as in other machines [52, 55, 56] is the plasma current I_p. The global energy confinement time τ_E was found to increase linearly with I_p over almost the full current range accessible in ASDEX (150 kA ≤ I_p ≤ 450 kA). This applies to L- and H-mode discharges, as shown in Fig. 45. The τ_E^* values for H-discharges are averaged over ELMs during a quasi-stationary state. At the highest plasma current, τ_E^* for an H-mode D^+ plasma is comparable to the saturation confinement time of Ohmic discharges. With ELMs, however, a tendency of τ_E^* to level off at high I_p is generally observed. Unfortunately, it is not possible within the ASDEX parameter range to find out whether the breakdown of the I_p scaling at high plasma currents is caused by q_a approaching a value of 2 or by τ_E reaching the saturation level of Ohmic discharges.

Since no current scaling is observed in Ohmic plasmas, the transport in the H-phase seems to be related with that of L-type discharges rather than that of Ohmic discharges. We consider the dependence of τ_E on I_p under auxiliary heating conditions to be a consequence of the Ohmic power input, which is negligible. Therefore, this dependence, which is common to L-plasmas and H-plasmas, does not necessarily imply any common trends in microscopic transport and does not necessarily represent a contrast between ohmically heated and auxiliary heated discharges.

3.4.3. Power dependence

The ASDEX neutral beam system with eight ion sources is especially well suited for power scan experiments since it allows the heating power to be varied in fairly small steps. The power from one ion source of about 0.4 MW is comparable to the Ohmic heating power. Additional heating with only one source already leads to a complete change of the electron transport. The dependence of τ_E^* on the total heating power P_{tot}, deduced from power scan experiments with H^0 injection, is illustrated in Fig. 46. The (L-mode) results can be

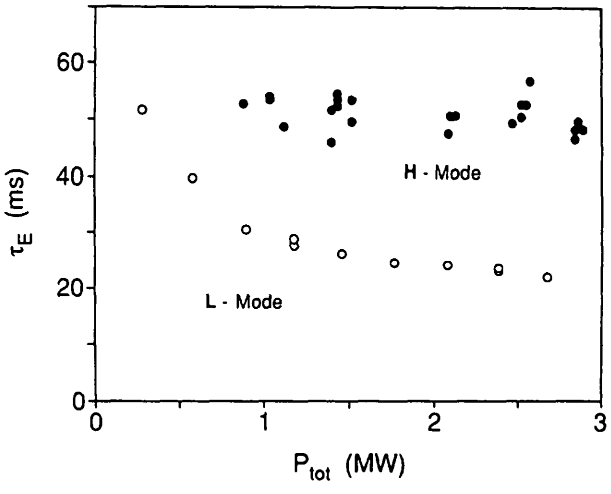

FIG. 46. Power dependence of the global confinement time for L- and H-discharges ($H^0 \rightarrow D^+$, I_p = 320 kA, B_t = 2.2 T).

well described by $\tau_E^* \propto P_{tot}^w$, with $w \approx -1/2$ for heating powers of up to 3.5 MW. This finding is in qualitative agreement with the results of other experiments [55] and was confirmed by detailed transport analyses [31].

The power dependence of H-mode discharges has been investigated by operating in a single-null divertor configuration. This configuration yields somewhat lower confinement values than the double-null configuration (see Fig. 61), but it reduces the power threshold for the L-H transition and therefore permits a scan over a wider power range. The results of Fig. 46 demonstrate that the energy confinement time in quasi-stationary H-phases with ELMs is largely independent of the heating power ($\tau_E \propto P^{-0.06\pm0.03}$).

3.4.3.1. Power scaling of τ_E in the quiescent H-mode

A lack of power dependence for deuterium injection into deuterium plasmas was reported previously from DIII-D [11]. These findings are in contrast to those from JET [57] and JFT-2M [7], where a degradation of τ_E was observed in the H-mode as well as in the L-mode. Recent results from DIII-D, obtained from a wider power range ($P_{OH} \leq P \leq 12$ MW), also indicate a power degradation of τ_E. The different results for the power dependence of τ_E lead to great uncertainties in the prediction of the H-mode confinement attainable in next-generation tokamak experiments. We try to analyse the power dependence of τ_E in the quiescent H-mode and to compare it with that of the regular H-mode. It is possible that the H^*-mode displays intrinsic H-mode confinement properties because ELMs do not additionally contribute to the energy losses. The power scaling studies of JET are for discharges without ELMs, but the published results of ASDEX and DIII-D are for discharges with ELMs.

In ASDEX, with $I_p = 0.32$ MA and $B_t = 2.2$ T, power scans in the quiescent H-mode could be made for both H^0 and D^0 injection into deuterium plasmas, in the restricted power range $1.75 \leq P_{NI} \leq 3.5$ MW. For discharges without ELMs, an additional difficulty in the τ_E analysis is that the H^*-phase does not reach a steady state and is suddenly terminated by a thermal quench due to excessive impurity radiation (see Fig. 37). The duration of the H^*-phase depends on the heating power and increases from 95 ms at 1.75 MW to 125 ms at 3.5 MW. During the H^*-phase the particle content increases linearly at a rate corresponding to two to three times the beam fuelling rate. The impurity radiation increases nearly exponentially. After the L-H^* transition, the poloidal beta increases again because of the improved confinement; when the impurity radiation starts to affect the energy balance, β_p rolls over and already decreases during the H^*-phase. Because of the non-steady-state conditions and the central radiation losses, the τ_E analysis is done in three steps: First, τ_E is evaluated according to $\tau_E^{(1)} = E/(P_{tot} - dE/dt)$, to correct for the absence of a steady state. These values can be compared with those from other experiments (e.g. for the purpose of size scaling). Second, the following relation is used:

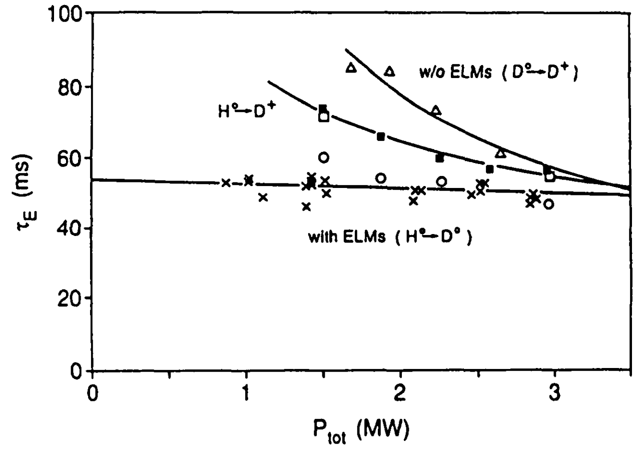

FIG. 47. Global energy confinement time in the quiescent H-mode (H) and in the regular H-mode (H) with ELMs, versus heating power. The curve is a power fit to the $D^0 \rightarrow D^+$ (Δ) case, the horizontal line is a guide for the eye regarding the H-cases with $H^0 \rightarrow D^+$ (×). The circles are calculated from the $H^0 \rightarrow D^+$ $\tau_E^{(2)}$ values with the radiation correction. The $\tau_E^{(1)}$ values from the TRANSP analysis ($H^0 \rightarrow D^+$) are indicated by squares.*

$$\tau_E^{(2)} = \tau_E^{(1)} \cdot \left[1 - \frac{\int_0^a r \int_0^r p^{rad}(\rho)\, \rho \, d\rho \, dr}{\int_0^a r \int_0^r p^{heat}(\rho)\, \rho \, d\rho \, dr} \right]^{-1} \qquad (1)$$

Equation (1) corrects for the radiation power emitted in the radial zone where the radiation and the heating power densities concur. Edge radiation alone does not lead to a correction. The $\tau_E^{(2)}$ values should represent the actual transport properties of the quiescent H^*-mode. There is a certain arbitrariness in the choice of $\tau_E^{(2)}$ since it strongly varies with time (as is also shown in the τ_E traces of Fig. 47). We choose the $\tau_E^{(2)}$ values at the time where $\tau_E^{(1)}$ has a maximum (the maximum is typically reached one confinement time after the L-H transition; thereafter, β_p decreases because of excessive radiation).

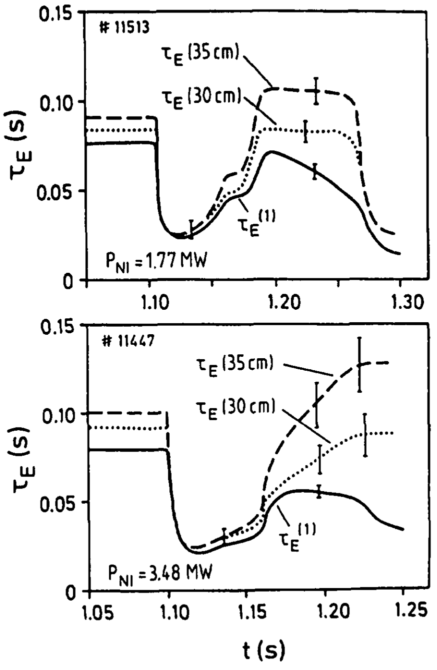

FIG. 48. Energy confinement time τ_E at two radii and replacement time $\tau_E^{(1)}$ for two H-discharges with different heating powers, as obtained from TRANSP.*

In the third step, a full transport analysis is performed (using TRANSP) for two H*-discharges — one with the lowest heating power and one with the highest heating power — to have a further check on the data and the analysis.

Figure 47 shows the power dependence of the global confinement times $\tau_E^{(1)}$ in the H*-mode, evaluated as described above, in comparison with τ_E values of the regular H-mode with ELMs. Since H-phases with ELMs reach a steady state, τ_E is calculated in this case simply from $\tau_E = E/P_{tot}$, as described above. In the quiescent H-mode, τ_E does indeed show a power dependence. The following scaling results are obtained for the H*-phase (based on four data points only!): $\tau_E^{(1)} = 86P^{-0.41\pm0.05}$, for $H^0 \rightarrow D^+$, and $\tau_E^{(1)} = 132P^{-0.75\pm0.16}$, for $D^0 \rightarrow D^+$. The curve in Fig. 47 is the power fit to the $D^0 \rightarrow D^+$ cases, with the horizontal line indicating the results obtained with ELMs.

Figure 48 shows the time dependence of τ_E as obtained from the full transport analysis, which also yields the time dependence of $\tau_E^{(1)}$. The confinement times are plotted for the OH-phase, the L-phase and the H*-phase. The results shown are for the cases of lowest and highest power. The τ_E values are obtained from the transport analysis, with allowance for radiation losses, and correspond to $\tau_E^{(2)}$ as obtained from Eq. (1) [58]. The $\tau_E^{(1)}$ values obtained from the transport analysis are also plotted in Fig. 47.

We find in ASDEX the same power dependence of τ_E in the quiescent H*-mode as in JET. Since such a dependence is not observed in the regular H-mode, it can be speculated that in this case τ_E is predominantly determined by the energy losses caused by ELMs superimposed on the heat transport losses, so that the overall confinement time is independent of power. We try to analyse this possibility in the following.

3.4.3.2. Effect of ELMs on global confinement

Since ELMs are external modes, the global confinement is affected. A discharge with frequent ELMs followed by quiescent phases is shown in Fig. 20. As soon as ELMs set in, the particle and energy contents decrease. It is difficult to assess the energy losses per event. From the changes in the slope of the β_p trace (Fig. 20(a)) we conclude that τ_E^{ELM} (for losses during periods of frequent ELM events with low amplitude) is about 110 ms.

The energy lost during an ELM event can be determined in three ways. First, $\Delta\beta_p$ can be measured directly by using the equilibrium coils, which are placed within the vacuum vessel and have a sufficient time response. Typically 5% of the energy content is lost in an ELM event (Fig. 20(b)). Second, the energy loss can be determined via the effect of an ELM event on the plasma profiles; n_e and T_e are reduced in the range from the plasma edge to r ~ 15 cm (see Fig. 16). The relative amplitude increases approximately linearly with the radius, with $\Delta n_e/n_e \approx \Delta T_e/T_e \approx 10\%$ at $r = 30$ cm. Assuming that the T_i profile is affected by an ELM event in the same way as n_e and T_e, the energy loss can be integrated; it is found that about 8% of the energy is lost. Third, the energy loss of an ELM event can be evaluated by measuring the power flux into the divertor chamber and onto the target plate, with a peak power density of about 1 $kW \cdot cm^{-2}$ and a width of about 4 cm (see Fig. 36). The period of increased energy loss during an ELM event is approximately 0.4 ms; the energy loss is found to be about 10 kJ, which is in rough agreement with the other estimates. The particle loss per ELM event is typically 1×10^{19}, corresponding to $\Delta N_e/N_e \approx 5\%$.

The repetition time of ELMs depends on the heating power. At low power, ELMs appear erratically and the ELM period is not well defined. At high power, the repetition time of ELMs becomes constant (about 6 ms) and the ELM period is better defined. Figure 49 shows the distribution of the ELM frequency at the low and

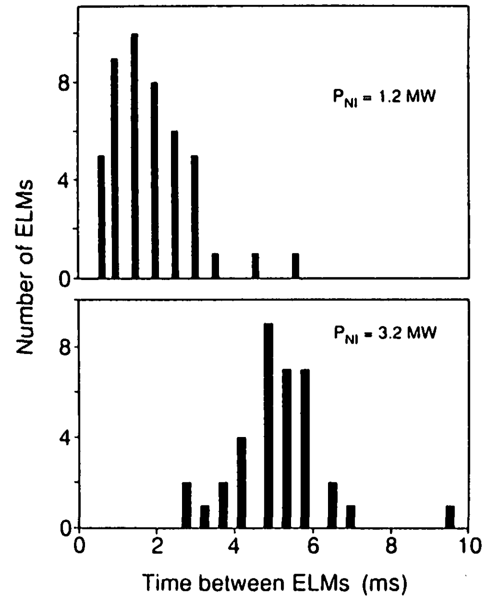

FIG. 49. Frequency distribution of the ELM period for low and high powers.

high power ends of the scan. It was not possible to determine the amplitude distribution of ELMs. The low power, high frequency ELMs are clearly smaller in amplitude. Assuming a constant ELM amplitude $\Delta E/E$ of 6% and a repetition time t_{ELM} = 6 ms, we obtain a confinement time for the ELM losses alone, $\tau_E^{ELM} = E/\Delta E \cdot t_{ELM}$ = 100 ms. For large amplitude singular ELM events the equivalent confinement time is τ_E^{ELM} = 110 ms, estimated for the integral effect of frequent low amplitude ELMs which dominate a low power (see Fig. 20(a)). Because of the agreement between these data, we assume that the losses due to ELMs are largely independent of power under the conditions of our H-mode power scans. Superimposing the ELM losses onto the intrinsic and power dependent transport losses, we have calculated the power dependence of the global confinement time: $\tau_E^{-1} = (\tau_E^{(2)})^{-1} + (\Delta E/E) t_{ELM}^{-1}$. The results obtained in this way (open circles in Fig. 49) are also plotted in Fig. 47. They agree roughly with the measured τ_E data as obtained for the regular H-mode with ELMs.

We conclude that the global energy confinement time decreases with power when the H-mode is operated in the quiescent H-phase as in JET. However, this conclusion has a rather weak experimental basis because operation in the H-mode without ELMs is limited on ASDEX. The lack of power dependence in the regular H-mode with ELMs could be due to the power dependent microscopic transport losses in addition to those caused by ELMs.

The ratio of τ_E in the quiescent H-mode between JET and ASDEX (both with $D^0 \rightarrow D^+$), as determined from β_p without radiation correction, is about 20, which is a factor of two more than the ratio of the currents, indicating an additional approximate scaling with the major radius.

3.4.4. Plasma species dependence

The confinement properties of neutral beam heated ASDEX discharges have been studied with hydrogen, deuterium and, to a smaller extent, helium target plasmas. Transitions to the H-mode have been obtained in all cases, with some differences in the operational range (see Section 4). Figure 50 shows the density dependence of τ_E for $D^0 \rightarrow D^+$, $H^0 \rightarrow H^+$ and $H^0 \rightarrow D^+$ H-mode cases. For comparison, OH results are also shown. As in the other confinement regimes, the energy confinement time of deuterium is superior to that of hydrogen: $\tau_E^H/I_p(D^0 \rightarrow D^+) = 0.23\ \mathrm{ms \cdot kA^{-1}}$, $\tau_E^H/I_p(H^0 \rightarrow D^+) = 0.16\ \mathrm{ms \cdot kA^{-1}}$, $\tau_E^H/I_p(H^0 \rightarrow H^+) = 0.11\ \mathrm{ms \cdot kA^{-1}}$. The power dependence of τ_E for $H^0 \rightarrow H^+$ is plotted in Fig. 51 for L- and H-modes. The isotope effect on τ_E in both L- and H-phases has been confirmed also by injection of two successive NI pulses — one with hydrogen and one with deuterium — separated by an Ohmic phase; these pulses were injected into a single deuterium discharge for both

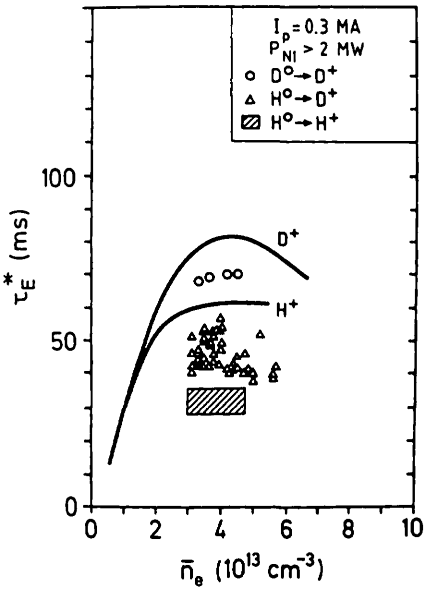

FIG. 50. Density dependence of τ_E^* in the H-mode for $H^0 \rightarrow H^+$, $H^0 \rightarrow D^+$ and $D^0 \rightarrow D^+$; Ohmic results (fitted curves) are shown for comparison.

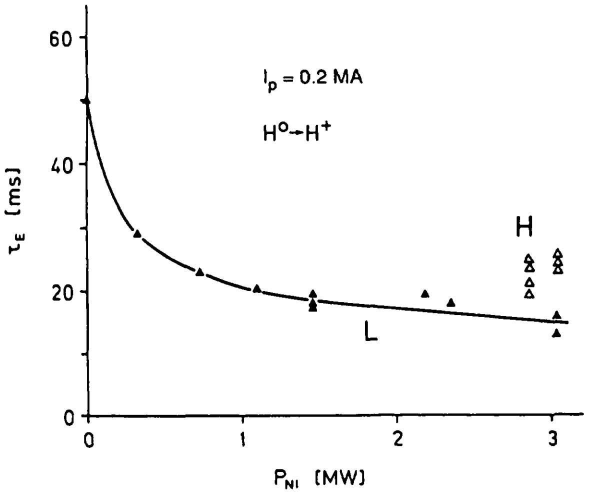

FIG. 51. Power dependence of L- and H-mode results for $H^0 \rightarrow H^+$.

the L-phase ($P_{NI} = 1.2$ MW) and the H-phase ($P_{NI} = 1.55$ MW). The ratio τ_E^D/τ_E^H[L] is 1.42 and τ_E^D/τ_E^H[H] is 1.53. Although it is primarily the ion mass which is different in these cases, it seems that the superior confinement properties of deuterium plasmas are a consequence of the electron transport since electron heat losses dominate the energy balance in these discharges.

3.4.5. *Toroidal field dependence*

The effect of the toroidal magnetic field B_t on the confinement of neutral beam heated ASDEX discharges was investigated in a few series of experiments in which B_t was varied in the range $1.6 \text{ T} \leq B_t \leq 2.6 \text{ T}$, while all other plasma parameters were kept constant. The results of various B_t scans are shown in Fig. 52. They demonstrate that the toroidal field does not significantly affect the global energy confinement in both the L-mode and the H-mode.

3.4.6. *Summary of the τ_E scaling results*

In the scaling studies we investigated the role of the external parameters $\bar{n}_e$, I_p, P_{tot} and B_t, and of the atomic mass A_i of the target plasma. The scaling for τ_E can be summarized as

$$\tau_E = C\, n_e^0 \times I_p^1 \times P_{tot}^0 \times B_t^0 \times A_i^1$$

Generally, the confinement results for the H-mode are given by a combination of microscopic transport and energy losses through an MHD process. In the above scaling results the parameter scaling of the impact of ELMs on the energy losses is partly included.

The above scaling relation has been obtained from the outcome of well prepared and controlled single parameter scans. We have also constructed scaling relations from a larger database in which not only the results of optimized scenarios are included. We have divided the database into two groups, representing discharges from shots No. 4000–12000 and from shots No. 17000–20000, which makes it possible to assess also long term aspects in the development of the confinement. The following results have been obtained for $H^0 \rightarrow D^+$:

Early series: $\tau_E^H \text{ (ms)} = 1.00\, I_p^{0.57}\, P_{tot}^{-0.50}\, n_e^{0.32}$
Late series: $\tau_E^H \text{ (ms)} = 0.90\, I_p^{0.70}\, P_{tot}^{-0.41}\, n_e^{0.22}$

where I_p is in kA, P_{tot} is in MW and n_e is in 10^{13} cm^{-3}.

The scaling result of the total data bank (154 data points) is:

$$\tau_E^H = 0.987\, I_p^{0.67\pm0.07}\, P_{tot}^{-0.30\pm0.05}\, n_e^{0.22\pm0.06}$$

Figure 53 shows a histogram of the data versus the ratio of τ_E^H and the predicted values of the Goldston [59] scaling and the Kaye-Goldston [60] scaling. The H-mode results are typically a factor of two above the L-mode scaling results. A factor of two is also obtained in the comparison of the H-mode confinement times with an ASDEX L-mode database.

3.4.7. *Scaling of transport coefficients*

Local (flux surface averaged) transport has been analysed by computer simulations of a series of

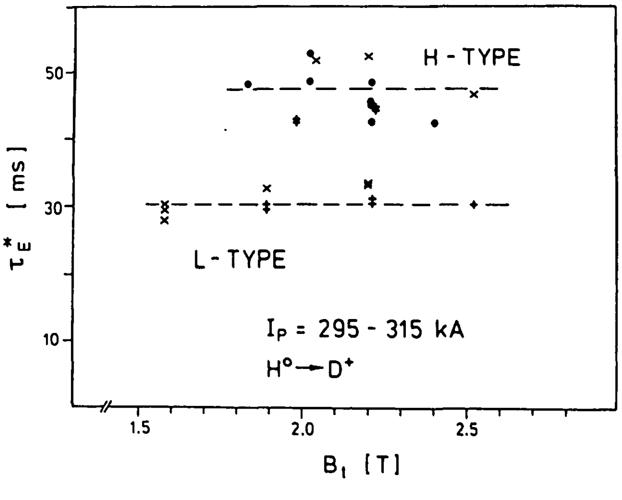

FIG. 52. Variation of the energy confinement time with the toroidal field for L- and H-discharges. The different symbols belong to different series of experiments.

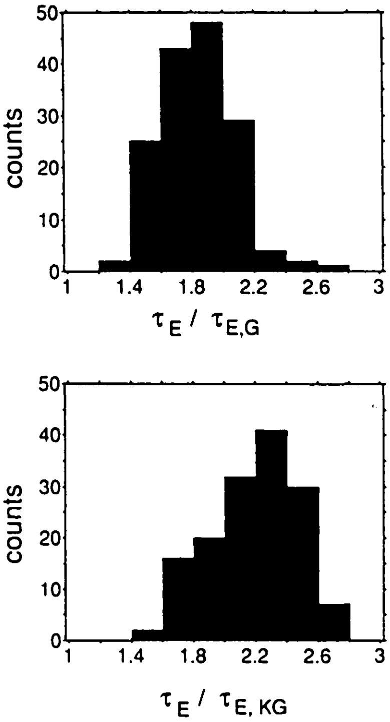

FIG. 53. Histogram of the τ_E values of the H-mode normalized with respect to the predicted values.

ASDEX L- and H-discharges. The coefficients obtained are for tangential co-injection of hydrogen into deuterium target plasmas and for injection powers much higher than the Ohmic input power before the auxiliary heating. The following empirical scaling relations give a good fit to the measured profiles of the electron density and the electron and ion temperatures, and to the poloidal beta in the L-regime, the H-regime with ELMs and the H*-regime [33, 42, 43]:

$$\chi_e(r)\ (\mathrm{cm^2 \cdot s^{-1}}) = C_0\, q(r)\, B_t(R)^{-1}$$

$$D(r) = 0.4\, \chi_e(r)$$

$$v_{in}(r) = 0.5\, D(r)\, T_e(r)^{-1} \frac{\partial T_e}{\partial r}$$

where C_0 is a regime dependent factor, $C_L = 6.2 \times 10^5$, $C_H = 2.5 \times 10^5$ and $C_H^* = 1.3 \times 10^5$. B_t is in kG and $qB_t^{-1} = r\,(B_pR)^{-1}$, with the major radius R in cm. The outstanding features of χ_e are the inverse B_p scaling and the lack of a density and temperature dependence. The thermoelectric type relation for the anomalous inward drift is found to work in the above regimes [44] and is applied instead of the Ware pinch.

4. OPERATIONAL RANGE OF THE H-MODE

The H-mode can be produced over a wide parameter range, and in ASDEX it is the L-mode which is limited to small regions of the operational space. For the H-mode a threshold beam power is required and it is only accessible in a density window. The H-mode is achieved in hydrogen, deuterium and helium discharges, in single-null (SN) and double-null (DN) divertor plasmas, with either neutral injection (co- and counter-injection) or ion cyclotron resonance heating. For NI, the power threshold depends on the plasma configuration, the species, the NI geometry, the location of the gas input valve (divertor dome fuelling is superior to gas puffing into the main plasma vessel) and on circumstances that are less controllable, such as the wall and recycling conditions or the unpredictable occurrence of a large sawtooth in the L-phase which triggers the L–H transition. The configurational aspects of the L–H transition are considerable. The H-mode is most easily accessible in the SN divertor configuration. The lowest power threshold for the L–H transition ever observed on ASDEX was obtained with counter-NI. In this case, a total power of 1.1 MW (60% NI power and 40% OH power) was sufficient to trigger L–H transitions at 420 kA, 380 kA and 300 kA, in a DN configuration at the higher currents and in an SN configuration (vertical position $\Delta z = -4$ cm) at the lower current. SN operation at 420 kA did not further reduce the power threshold. The low power injected in these cases, however, did not allow the H-mode to be maintained for more than 10 ms, after which time the occurrence of ELMs caused the plasma to switch back to the L-mode. Even at high powers, the H-mode developed only for rather short phases (a few ten milliseconds) and mostly collapsed because of a strong increase of radiation or because of MHD problems. H-mode studies with counter-NI are, therefore, of a preliminary nature.

4.1. Parameter dependence of the H-mode power threshold

Study of the power threshold P_{thr} for the H-mode is of importance because such a study may reveal the inherent transition physics; furthermore, there seem to be crucial differences between the various experiments. In JET [61] and DIII-D [62] it is observed that P_{thr} increases with the toroidal field; in DIII-D it is found that P_{thr} increases also with the density. For JFT-2M an increase of P_{thr} with current is reported [7]. In particular, the unfavourable dependence of P_{thr} on B_t and $\bar{n}_e$ may jeopardize the prospects of high field/high density

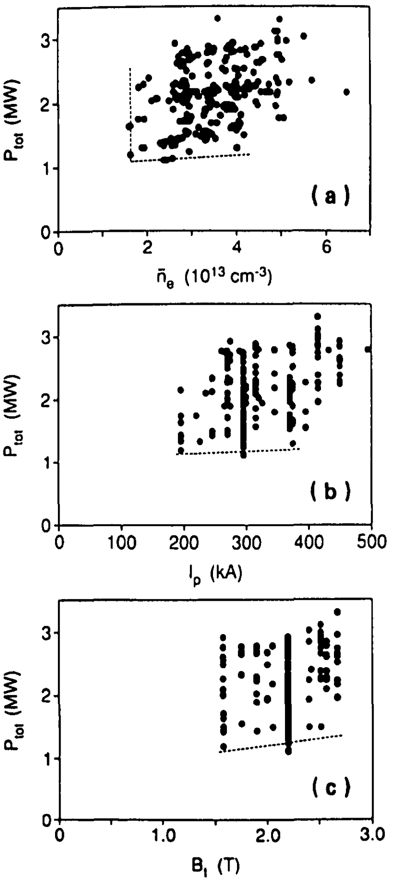

FIG. 54. Operational diagram for H-mode plasmas giving the power threshold versus (a) line averaged density $\bar{n}_e$, (b) plasma current I_p and (c) toroidal field B_t.

devices being able to operate in the H-mode. Figure 54 shows the operational range of H-discharges versus the setting parameters of the discharge, i.e. the density in the OH plateau phase, the current and the toroidal field. The power threshold is approximately 1.1 MW; in the experimentally accessible range, no current or field limitation has been observed. The operational range of the H-mode is, however, restricted by a lower density limit (approximately 1.7×10^{13} cm^{-3}). It is of importance that the H-mode can be accessed at all current levels, even up to the highest values, I_p = 490 kA. These discharges are of interest because at $q_a = 2$ (B_t = 1.86 T) the highest densities are achieved on ASDEX. The quality of these low q_a H-phases is, however, degraded, possibly because of the increased density. A confinement time of 50 ms is obtained at $\bar{n}_e = 7 \times 10^{13}$ cm^{-3} and I_p = 480 kA.

In contrast to the results of other experiments, no pronounced dependence of P_{thr} on B_t, I_p or $\bar{n}_e$ has been detected. A weak dependence of P_{thr} on the density cannot be excluded. This could be understood from considerations that the power threshold may be caused by the necessity to raise the edge electron temperature (or a related quantity) above a limiting value. The actual sensitivity of P_{thr} on $\bar{n}_e$ may depend on recycling control and on the actual geometrical conditions, which may be less favourable in an expanded boundary topology than in a closed divertor. The aspects of recycling control will be discussed in Section 4.2.

Because of the linear (or even steeper) increase of P_{thr} with B_t, as observed in other experiments, we have studied this aspect in great detail. Figure 55 shows H_α radiation traces, measured in the upper outer divertor chamber, which serve as monitors for confinement phases, at various toroidal fields and constant plasma current I_p = 290 kA. The power is scanned during the discharge in three pulses. In all cases, the H-mode is realized in the third pulse, at P_{tot} = 2.2 MW. In the case of the lowest B_t value, the H-mode develops already during the second pulse, at P_{tot} = 1.65 MW. From this observation it may be concluded that there is indeed a B_t dependence of P_{thr} which is not distinguishable in a scatter diagram of all data (Fig. 54(c)). However, we should point out that the sawtooth amplitude at the edge increases when B_t is lowered (in a case where I_p = const), as indicated, for example, by the sawtooth modulation of H_α during the first pulse. Unlike in the other cases, the L–H transition is triggered in this case by a sawtooth at the lowest field value, B_t = 1.7 T, leading to a B_t dependence of P_{thr}, which, however, is actually given by a secondary process.

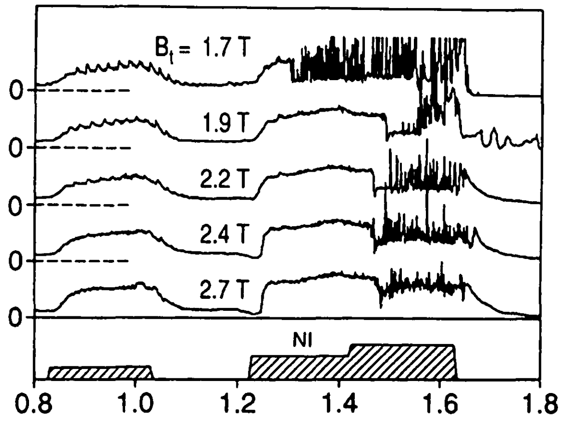

FIG. 55. Temporal evolution of the H_α/D_α radiation in the divertor chamber for three NI pulses with different beam power levels. The variation of B_t from discharge to discharge is indicated.

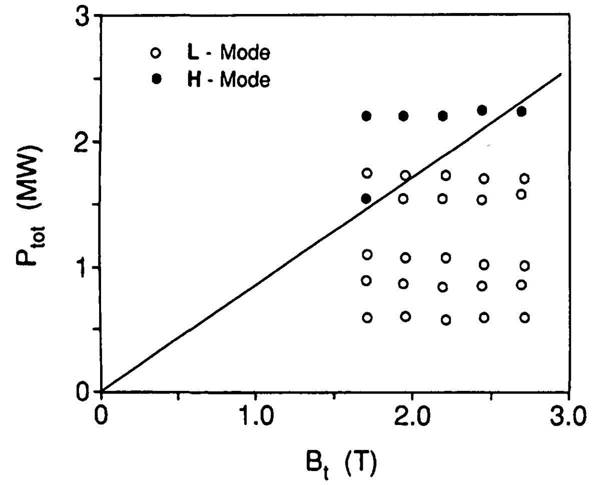

FIG. 56. *Operational diagram giving the power threshold as a function of B_t. The data points are the results of a detailed single parameter scan carried out for this purpose.*

In a second scan, the power in the three pulses was reduced to 0.6, 1.0 and 1.7 MW. No H-phase appeared in the range 1.7 T ≤ B_t ≤ 2.7 T.

Figure 56 summarizes these results in an operational diagram. A linear relation between P_{thr} and B_t can be concluded from Fig. 56 (solid line). The slope of the line is $\alpha = ((P_{Max} - P_{Min})/P_{Min})/((B_{Max} - B_{Min})/B_{Min}) < 0.7$. The slope of the boundary in Fig. 54 is $\alpha \simeq 0$. The comparable values are $\alpha \simeq 1.1$ for DIII-D [62] and $\alpha \simeq 3.7$ for JET [61].

Because of the importance of the B_t dependence of P_{thr} we have also studied the duration of the L-phase preceding the L–H transition in a B_t scan. The idea behind this investigation is that a potentially favourable B_t dependence of P_{thr} would also be indicated by a shortening of the L-phase when B_t is decreased. No such dependence has been found (see Fig. 57).

Figure 58 exemplifies in single parameter scans the lack of an I_p dependence of P_{thr}. Plotted is the rise of β_p (as deduced from plasma equilibrium) for the low power L-cases and the high power H-cases at three current levels. The L–H transition occurs at $P_{NI} \sim 2$ MW (DN discharges). There is a lower density threshold for the development of the H-mode, about 3×10^{13} cm^{-3} (see Fig. 59), which might slightly increase with the current. The results shown in Fig. 59 are also obtained from DN discharges. There is also an upper density threshold for the development of the H-mode, which — under ASDEX heating conditions — is about 7×10^{13} cm^{-3}. At high density, achieved under the unfavourable conditions of gas puffing, the H-mode edge conditions obviously cannot be maintained with the given heating power. A similar observation was made in PDX [63]. With pellet refuelling under conditions of low edge cooling, the upper density threshold can be increased (see Section 5.3).

The power threshold clearly depends on the divertor configuration and on the isotope mass of the target plasma and the beam. For the L–H transition, less power is required in the SN configuration than in the DN configuration. Figure 60(a) shows the data from Fig. 54, sorted according to the plasma configuration.

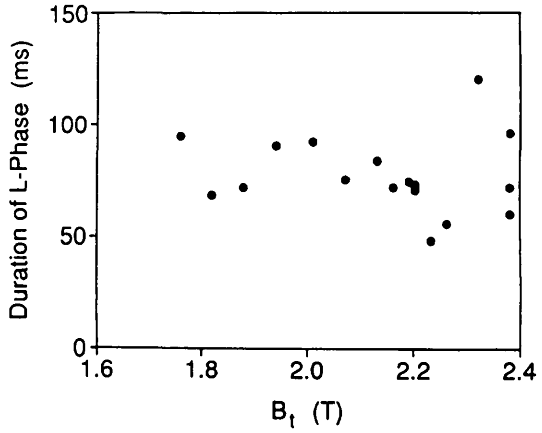

FIG. 57. *Duration of the L-phase preceding the L–H transition versus toroidal field.*

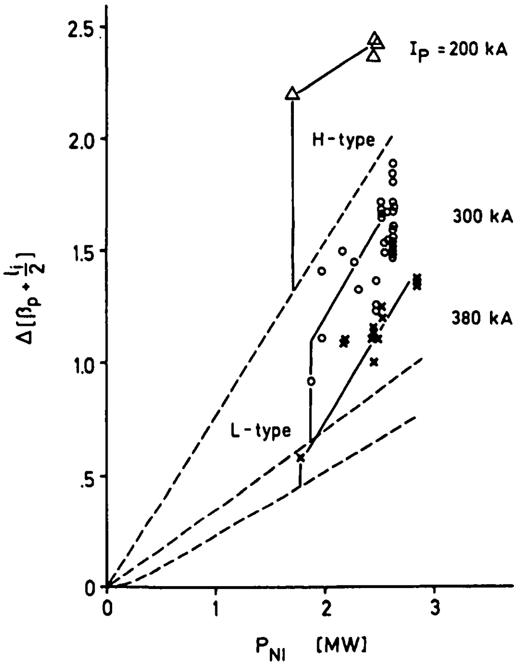

FIG. 58. *Increase in $\beta_p + \ell_i/2$ (from plasma equilibrium) versus NI power. For clarity, the L-mode data points are omitted; the transition to the H-phase is indicated.*

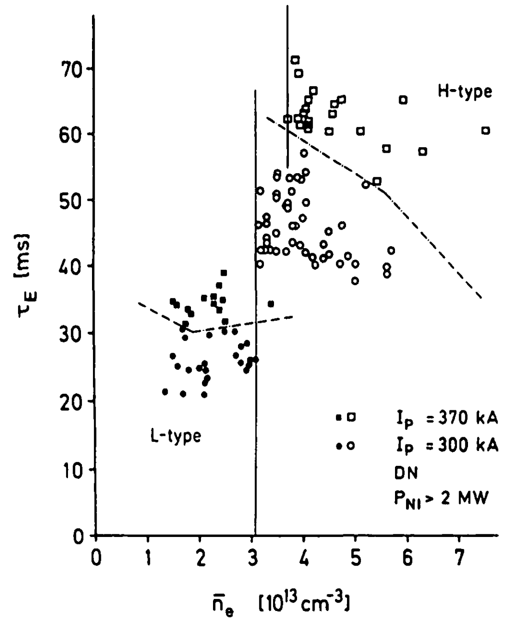

FIG. 59. Energy confinement time versus line averaged density for L- and H-mode discharges (DN configuration). The vertical lines denote the density threshold; the dashed lines separate the data points plotted for two different current values.

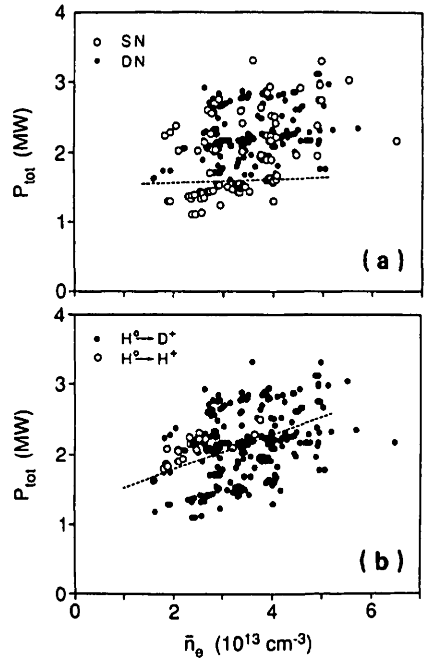

FIG. 60. H-mode operational diagram for discharges with (a) various configurations (SN, DN) and (b) various injection gases (H^0, D^0). The power threshold is lower for the SN configuration and for $H^0 \rightarrow D^+$.

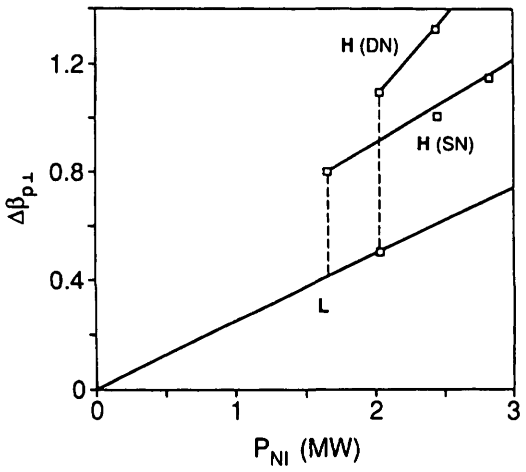

FIG. 61. Increase in $\beta_{p\perp}$ versus NI power, showing the lowering of the power threshold with the SN configuration. The SN τ_E values are lower, mostly because of a smaller plasma cross-section.

P_{thr} is about 1.5 MW for the DN configuration and 1.1 MW for the SN configuration. Figure 61 shows the rise of β_p (deduced from diamagnetism) from a single scan under controlled conditions; a H-mode in the SN configuration can be obtained at a power which gives L-mode plasmas in the DN configuration. (The rise of β_p is weaker in the SN configuration because the plasma minor radius is smaller.) In the SN configuration also the lower density limit is reduced, from typically 3×10^{13} cm^{-3} to 1.7×10^{13} cm^{-3}. The power requirements for the H-mode are reduced in the SN configuration only when the ion grad-B drift is directed to the X-point; otherwise, P_{thr} is even higher. This aspect will be discussed in Section 9.3.

Another scaling parameter for P_{thr} is the isotope mass of the target plasma and the beam. Figure 60(a) also shows cases with H^0 injection into H^+ (SN configuration); P_{thr} is increased by a factor of nearly two. The isotope effect on P_{thr} was confirmed under controlled conditions; a hydrogen pulse and a deuterium pulse were consecutively injected into a single D^+ discharge at low power. At P_{tot} = 1.3 MW, the hydrogen pulse did not produce the H-mode, while the deuterium pulse caused an L–H transition at a lower power, P_{tot} = 1.15 MW. It is interesting to note that the improved confinement with deuterium (see Section 3.4.4) has a positive effect also on P_{thr}.

The question of whether the H-mode can only be realized under divertor conditions has been examined on ASDEX with various limiter configurations, i.e. poloidally closed ring limiters, poloidal arc limiters placed on either the high or the low field side,

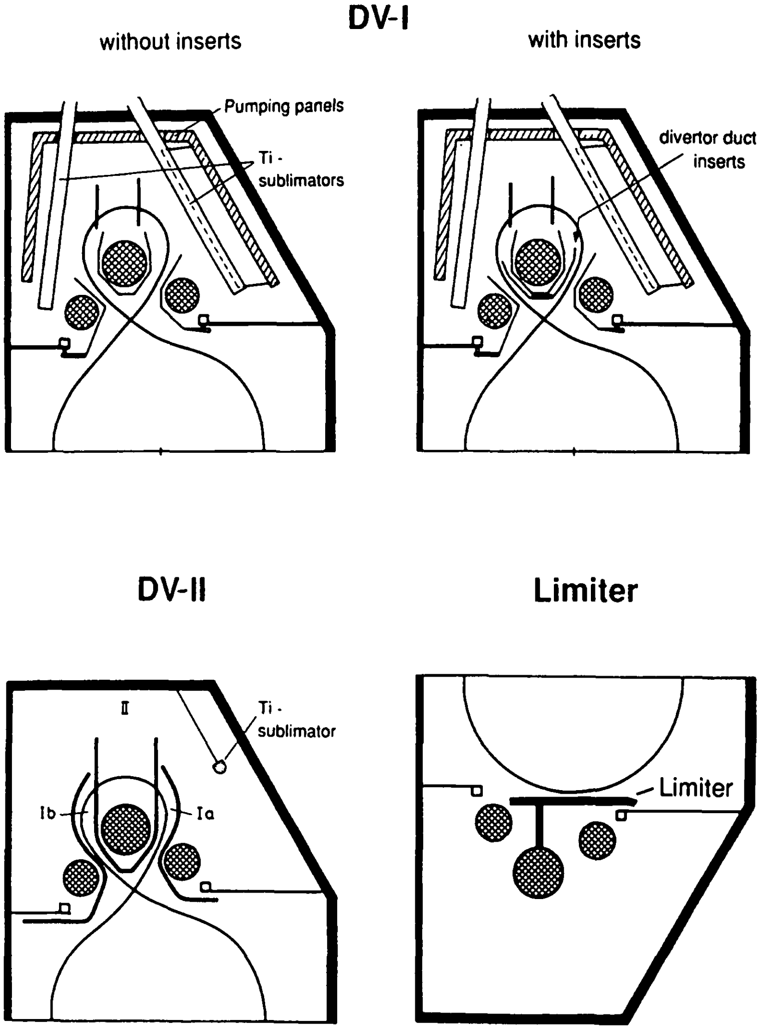

FIG. 62. The different divertor configurations of ASDEX with which H-mode studies were carried out. The structures of DV-I were radiation cooled, those of DV-II are water cooled. The cross-section of the toroidal graphite belt limiter in ASDEX is also shown.

mushroom limiters, and a toroidally closed belt limiter placed on the bottom side of the plasma. The limiter material was iron in all cases and, in a second version, graphite. The experiments with auxiliary arc limiters or with mushroom limiters showed that the H-mode is quenched at a separatrix-limiter distance of 2.5 cm, irrespective of the limiter position (at the low or the high field side). In a recent analysis of belt limiter discharges, L–H transitions have been detected. The results are presented in Section 4.3.

A specific limitation for H-mode confinement studies is the high beta stability limit. In spite of its superior confinement, the H-mode seems to have the same low beta limit as the L-mode [64]. However, this result may be an indication that different mechanisms are responsible for the stability limit at high beta and for the gradual degradation of confinement in the L-regime already at low beta.

H-mode plasmas conform to the beta limit scaling $\beta_{MAX} = CI_p/aB_t$ [15], with $C = 2.8$ for a thermal plasma or with $C = 3.5$ when plasma rotation and beam pressure are included. At the beta limit, ASDEX discharges generally do not disrupt, but the confinement degrades irreversibly during NI, causing beta to drop after it has reached a maximum [65].

In conclusion, the operational power range within which the intrinsic confinement properties of the H-mode can be studied is small. The H-mode can be established only at a power of more than 1.1 MW, and, because of the good confinement, a relatively low power of 3 MW brings the plasma up to the beta limit. Close to and at the beta limit, the confinement properties are additionally influenced by superimposed stability effects.

4.2. Study of the H-mode under various divertor topologies

The various divertor configurations which have been realized on ASDEX and explored for their impact on the development and properties of the H-mode are shown in Fig. 62. The H-mode was discovered in the previous divertor configuration DV-I without inserts, which had a closed divertor chamber. The only connection between the main plasma vessel and the divertor was through the divertor necks, with a vacuum conductance of 7 × 10^5 L·s^{-1} for molecular hydrogen. Many of the results described in this paper have been obtained in this configuration. In the configuration DV-I with additional inserts around the central multipole coil, the cross-section of the divertor neck was further reduced. In this configuration the vacuum conductance of the divertor neck was 3.2 × 10^5 L·s^{-1}. This modification did not cause any changes in the threshold power and the confinement properties of the H-mode. The modification of the divertor to the DV-II configuration [66] was necessary to enable long-puse heating to be performed. Since the modified divertor had to be water cooled, an additional and rather compact insert was installed in the previous divertor chamber. Now, the divertor chamber is no longer well separated from the main plasma vessel since by-passes establish a parallel conductance of 6 × 10^5 L·s^{-1}. These modifications had a strong impact on the power threshold, which increased to more than 2.6 MW (the present limit of the long-pulse injection system on ASDEX) for the DN configuration and to twice the previous value for the SN configuration (~2.4 MW). Clearly, the competing edge effects, which make sufficient edge heating impossible, are intensified in this geometry. In contrast to our previous experience, sawteeth do not disappear during the H-phase, which also indicates that edge heating is less effective. Furthermore, the quality of the H-mode confinement is degraded and after the L–H transition the increase in beta is only 50% of the previously obtained values. The main reason for this confinement degradation is a higher ELM frequency. A tentative explanation of the new situation is that after the L–H transition the edge density quickly rises owing to the higher recycling through the by-passes, with the consequence that the edge temperature does not increase sufficiently to stabilize the H-mode before the increased edge pressure gradient gives rise to an ELM. Because of these unfavourable aspects, the new divertor chamber was again separated from the main plasma vessel as much as was technically possible.

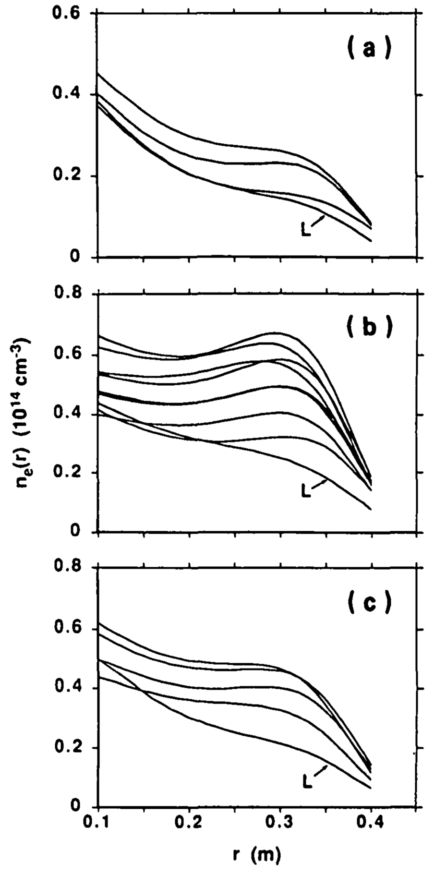

FIG. 63. Density profile development in the quiescent H-mode for various divertor configurations. Each case starts with the last L-mode profile just before the L-H transition. There is a successive rise in density. The profiles are measured by Thomson scattering with a repetition time of 17 ms. (a) DV-I, closed configuration; (b) DV-II, open configuration; (c) DV-II closed configuration.

To study the role of the recycling gas in more detail, only the upper divertor chamber was closed. This measure reduced the H-mode power threshold to the original level for upper SN discharges. The effect of recycling on the parameter dependence of the H-phase was studied in quiescent H-phases in the DV-I and DV-II configurations with open and closed divertor. The variation of the density profile shape and the increase of the electron temperature or density at the plasma edge were found to depend sensitively on the prevailing recycling conditions. Under closed divertor conditions the density profile broadened moderately but remained peaked throughout the quiescent H-phase. The most peaked profiles were obtained in DV-I and the broadest ones in the open configuration of DV-II.

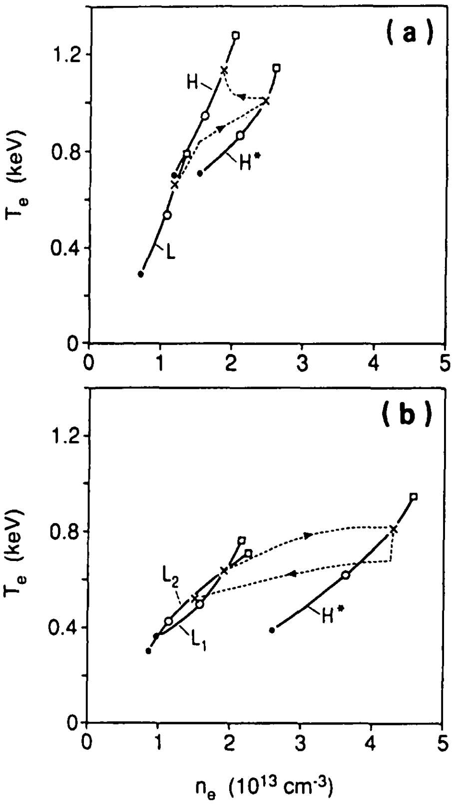

FIG. 64. Edge electron temperature versus edge density (• 2.5 cm, ○ 5 cm, × 7.5 cm, □ 10 cm inside the separatrix) for the L-phase and the H-phase.
(a) Edge profiles for the quiescent H-phase (H) and after the onset of ELMs (H, DV-I).*
(b) Profiles for the preceding L-phase (L_1) and the subsequent L-phase (L_2), and for the quiescent H-phase (DV-II).
The dashed curves follow the excursion of the parameters 7.5 cm inside the separatrix.

In this case, even hollow profiles were obtained. The profile development during the quiescent H-phase is shown in Fig. 63, beginning with the L-phase in each of the cases. The density builds up successively. The profiles are measured every 17 ms. The variation of the edge temperature and density at the L-H transition is plotted in Fig. 64 for the closed DV-I configuration and the open DV-II configuration. Data points are shown from r = 37.5 cm to r = 30 cm, in steps of 2.5 cm (see the various symbols). The plots of the L- and H-profiles in the quiescent phase (H^*) and in the phase with ELMs (H) in Fig. 64(a) document the strong rise in edge temperature with a modest rise in density. In the open divertor configuration (Fig. 64(b)) the rise in edge temperature is modest but the density increases strongly. The profiles are shown at the end of the L-phase preceding the L-H transition, at the end of the quiescent H-phase and at the beginning of the second L-phase. The dashed lines show a plasma cycle from the L-phase to the H^*-phase, and then to the phase with ELMs in case (a) and to the second L-phase in case (b). From our studies with various divertor configurations we come to the conclusion that the development of the density profile depends on the actual recycling conditions. This may explain some of the differences in the density profile shape in the H-mode as observed in various experiments [61, 62]. The study of various divertor configurations demonstrates that the edge pressure always increases after the L-H transition; whether it rises mainly via the density or via the temperature depends on the recycling conditions.

4.3. Limiter H-mode of ASDEX

The discovery of the H-mode under limiter conditions in JFT-2M [7] and in other experiments (see Section 8) stimulated thorough analyses of limiter discharges; on ASDEX, an axisymmetric belt limiter had been used in these discharges. Figure 60 shows the shape and position of this limiter in a poloidal cross-section. The limiter material is graphite. In limiter discharges the multipole coils were not in operation.

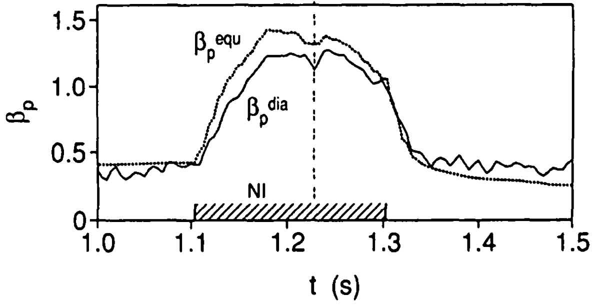

FIG. 65. Line averaged density along two chords, H_α intensity emitted in the midplane, and β_p^{dia} and β_p^{equ} for a limiter discharge. The transition to the H-mode is indicated by the vertical line. (Because of incomplete compensation, β_p^{dia} can only be used for relative measurements.)

These toroidal limiter plasmas showed L-type confinement in all cases investigated. Therefore, no detailed analysis of the discharges was carried out. A recent study showed that in some of these discharges there were indeed L-H transitions which had previously not been noticed. Figure 65 shows the density, the H_α measured in the plasma midplane and the poloidal beta estimated from plasma equilibrium and diamagnetism. The dashed line indicates the transition to the H-mode. At this transition, both the density and the energy content increase, the recycling decreases, the edge electron temperature increases, and ELMs set in which show the characteristic changes in density, edge electron temperature and horizontal plasma position; in the H-phase the high-Z impurity radiation increases. The increase in beta after the L-H transition is typically only 10% (in divertor discharges it is 100%). The small increase in beta after the L-H transition in limiter discharges of circular cross-section has also been observed in other experiments.

The only new information from the limiter H-mode discharges on ASDEX is that the H-mode can also be realized with a bottom limiter and not only with an inside limiter. Although the relevance of this finding is not studied here, it should be mentioned that the ion grad-B drift was away from the limiter (see Section 9.3).

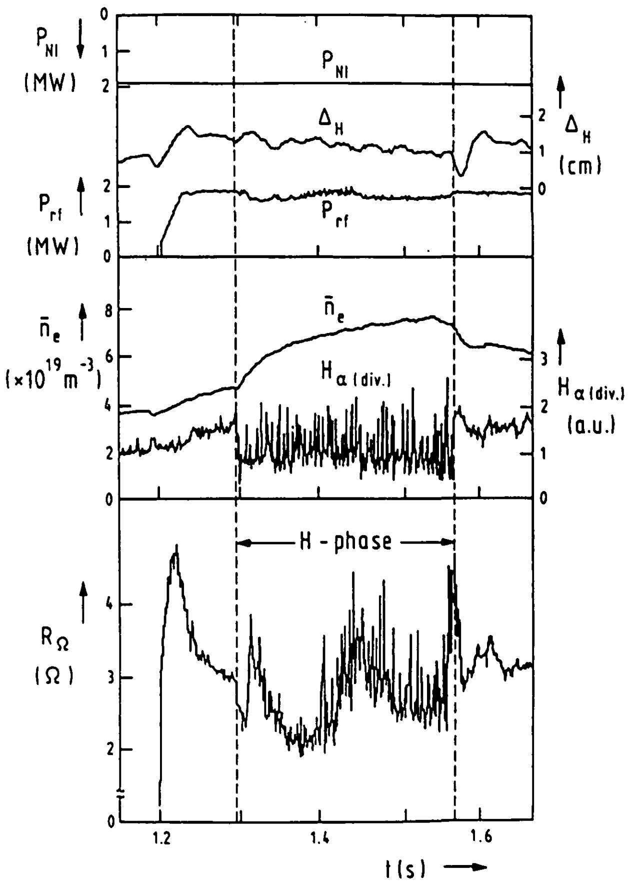

FIG. 66. H-mode discharge in experiments with 10% hydrogen minority heating (P_{NI} = 1.87 MW, P_{ICRH} = 1.9 MW).

5. USE OF OTHER HEATING AND REFUELLING TECHNIQUES FOR H-MODE PLASMAS

5.1. ICRF heating

Plasmas in the H-mode can also be operated with a combination of NI and ICRF, with either of them being the main heating method. It is also possible to produce an L-H transition with ICRF alone [67].

5.1.1. Hydrogen minority heating

We have succeeded in producing the L-H transition on ASDEX with hydrogen minority heating only, in the upper SN configuration (ion grad-B drift towards the X-point), at a coupled power of 1.8 MW. The drastic changes of the SOL (discussed in Section 2.5) give rise to a sudden change of the coupling conditions. In the experimental period from 1984 to 1986, one of the generators then invariably terminated the operation; this was due to voltage breakdown in one of the vacuum transmission lines, with the consequence that this H-mode was only transient [67]. Subsequently, the ICRF system was upgraded to withstand higher voltages and can now better cope with the changes in the SOL parameters at the L-H transition. Since the heating power required for attaining the H-mode is higher in the DV-II configuration than in the DV-I configuration (see Section 4.2), no H-phases were achieved with ICRH alone. The H-mode was only obtained with additional injection of deuterium into deuterium plasmas with a minimum power of >3.4 MW (P_{NI} = 1.87 MW, P_{IC} > 1.6 MW). Figure 66 shows an example of a 0.25 s long H-phase obtained with NI + ICRH. The L-H transition was clearly triggered by ICRH and ended because of the high density. The variation of the antenna resistance during the H-mode can be explained by the occurrence of eigenmodes due to the density increase [68]. The confinement time is degraded by frequent ELMs so that it is only 20-30% higher than for the best L-mode discharges. In some cases where the density rise is smaller owing to stronger ELM activity the H-mode can last for the whole ICRH pulse length (0.5 s).

5.1.2. Second-harmonic hydrogen heating

With second-harmonic hydrogen heating, the H-mode has so far only been achieved with the DV-I configuration and in combination with NI. It is of interest to note that it is easier to achieve the H-mode with the ion grad-B drift *away* from the X-point. This is thought to be due to the greatly reduced impurity radiation under this condition.

5.2. Lower hybrid heating and beam current drive in the H-mode

The combined operation of lower hybrid heating and NI has been studied on ASDEX in a wide parameter range [69, 70]. The use of lower hybrid current drive in combination with the H-mode, however, was limited to a very narrow density range. The upper density limit for lower hybrid current drive was at $\bar{n}_e = 2 \times 10^{13}$ cm^{-3} for the 1.3 GHz system. This value was only slightly above the lower density threshold of $\bar{n}_e \approx 1.7 \times 10^{13}$ cm^{-3} for the H-mode, which was regularly exceeded by the fast density rise immediately after the L–H transition. During the H-phase, lower hybrid powers of up to about 1 MW could be transmitted — the same level as was achieved in Ohmic target plasmas. The L–H transition never caused failures in the RF transmission. The power coupling remained comparable to that in the L-mode for the whole duration of the beam pulse, up to 0.4 s. Nearly half of the total plasma current in the target plasma was driven by lower hybrid heating. With neutral beam heating the loop voltage dropped to zero and the total current was driven non-inductively. The strong density rise during the H-phase, however, again led to an increase in the loop voltage. The electron temperature profile was peaking during lower hybrid current drive. The central temperatures rose to values comparable to those of the subsequent H-phase.

After the L–H transition, a pedestal in the electron temperature was formed close to the periphery and the radial profile of $T_e(r)$ assumed the same shape as in the case of an L–H transition from an Ohmic target plasma.

Under conditions without inductive current drive the plasma current could be kept constant at 150 kA by NI (otherwise it decays with its L/R time); with the beam driven current, regular H-phases could be achieved.

5.3. Pellet refuelling in the H-mode

Pellet refuelling of H-mode discharges was also possible on ASDEX with the use of a centrifuge for multi-pellet injection [71]. The small pellets contribute 1×10^{13} cm^{-3} each to the volume averaged density. Their penetration depth is small owing to the high electron temperature at the plasma edge. Nevertheless, the deleterious edge cooling of standard gas-puff refuelling could be avoided and the upper density limit for the H-mode was raised from $\bar{n}_e = (7\text{–}8) \times 10^{13}$ cm^{-3} to 1.2×10^{14} cm^{-3}. The density profiles are still broad and more characteristic of the standard H-mode than of pellet refuelled discharges. The high density pellet discharges, however, are plagued by frequent ELMs, which are probably responsible for the low confinement time of $\tau_E \approx 40$ ms (not corrected for radiation).

6. PHYSICS ASPECTS OF THE L–H TRANSITION

The L–H transition can be viewed as a bifurcation phenomenon in the sense that the properties of the final state (e.g. the confinement properties) differ widely, while the properties of the initial state (the plasma parameters of a discharge just before the L–H transition compared with those of a discharge remaining in the L-mode) can hardly be distinguished from each other experimentally [72]. Figure 67 compares a few typical diagnostic traces of two consecutive discharges — an L-discharge followed by an H-discharge. Operation close to the power threshold occasionally yields L- and H-discharges with identical external parameters for the plasma and the beam. The arrows indicate the moment of transition. The tableau of diagrams in Fig. 67 contains traces which document the variation of the external parameters, such as the current, the density and the horizontal plasma position, traces which illustrate the recycling conditions in the main plasma and in the divertor chamber, the impurity conditions (main plasma radiation, iron radiation and loop voltage) and the development of the energy content of the two discharges. Within the amplitude of the random fluctuations, the plasma parameters at the L–H transition are identical with those of discharges which remain in the L-mode throughout the pulse. This comparison shows that the search for the decisive parameter causing the plasma to carry out the L–H transition will not be easy. This search has to concentrate on the plasma conditions at the end of the L-phase. For an understanding of the physics of the L–H transition, only the L-phase should be considered and the structural elements of the fully developed H-phase (such as the changed profiles or the steep edge gradients) should not be included. For an understanding of the

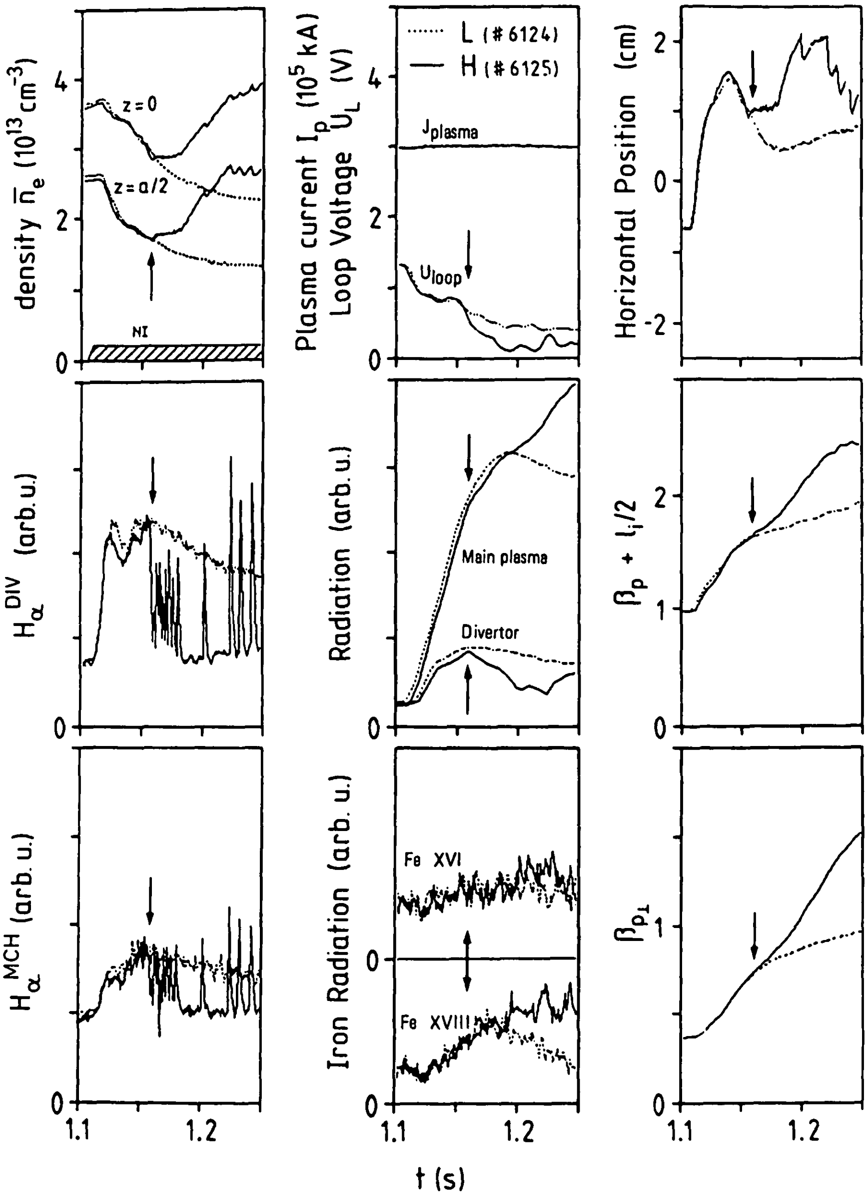

FIG. 67. Comparison of plasma parameter variations during the NI phases of two consecutive discharges, the first being an L-discharge and the second an H-discharge. The arrow indicates the L-H transition. (H_α^{MCH} (H_α^{DIV}) = H_α radiation in the main plasma vessel (divertor chamber).)

full extent of confinement improvement during the H-mode, however, these modifications may also be taken into account because the confinement continues to evolve and improve during the H-phase.

6.1. Role of the edge electron temperature

A minimal heating power is required for the L-H transition, and the H-phase develops after an L-phase. This behaviour points to the existence of a threshold which has to be surpassed for the H-mode to develop. In the initial phase, it takes some time before the plasma is sufficiently heated; if the power is too low, the threshold is not reached at all. These observations indicate that it may be the electron or the ion temperature, or a related quantity, such as pressure, temperature gradient, electrical conductivity or collisionality, which is responsible for the sudden change in confinement. The search for the crucial parameters first concentrated on the electron temperature because it was observed that no H-mode

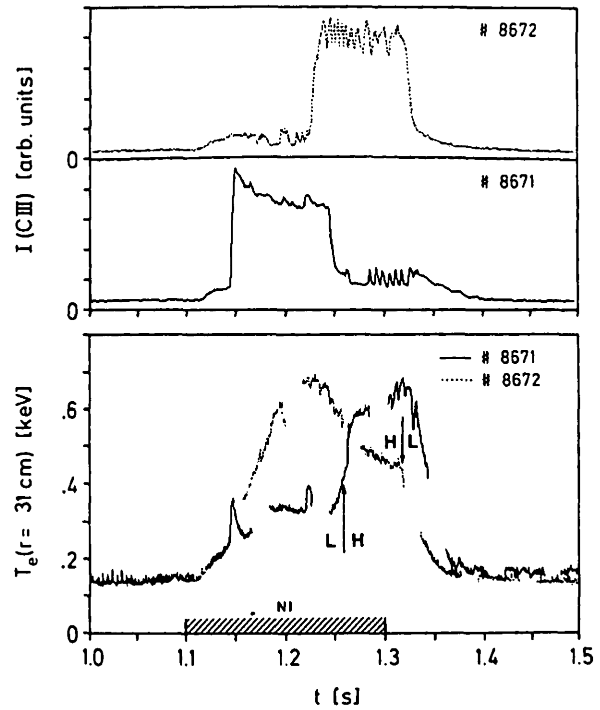

FIG. 68. C III line radiation and edge electron temperature of two discharges into which methane was injected during the NI phase from 1.14 s to 1.24 s (No. 8671) and from 1.22 s to 1.32 s (No. 8672). The impurity radiation cools the plasma edge and affects the L-H transition. I_p = 0.38 MA, $\bar{n}_e = 4 \times 10^{13}$ cm^{-3}, P_{NI} = 3.0 MW.

develops shortly after opening of the plasma vessel, when the walls have not yet been cleaned and the plasma suffers from excessive impurity radiation. We describe now some experiments which indicate the importance of the electron temperature (or a related quantity) for the L-H transition. In these experiments the electron temperature ECE diagnostic has been used since this is the only diagnostic which gives a continuous reading with sufficient time resolution. In the course of these experiments we came to the conclusion that it is probably the electron temperature of the plasma periphery which determines the development of confinement [72]. In the following diagrams we therefore plot the variation of T_e at the outermost channel, located at 31 cm in the midplane on the high field side, where measurement with the ECE diagnostic is possible. Because of the horizontal plasma shift during the discharge, the measuring point is about 7 to 8 cm away from the inner separatrix.

6.1.1. *Addition of impurities*

Artificial impurities have been introduced in discharges to study in detail their detrimental effect on the development of the L–H transition. Figure 68 compares two cases with methane injection into the discharge: at the beginning of the NI pulse (solid curve) and during the H-phase (dashed curve). When methane is injected at the beginning, the edge electron temperature is kept low and the L-phase is prolonged. When the impurity pulse is switched off, the electron temperature rises and the transition to the H-phase occurs. By contrast, when methane is injected during the H-phase, the edge temperature is reduced and the H–L transition occurs at about the same T_e value. (Without methane injection the H–L transition occurs 30 ms later at about the same temperature.) When neon (high Z) is used instead of methane, smaller amounts of it are sufficient to suppress the H-mode.

When one considers these results, one may be inclined to correlate the suppression of the H-mode in limiter discharges with excessive impurity (and recycling) cooling at the edge.

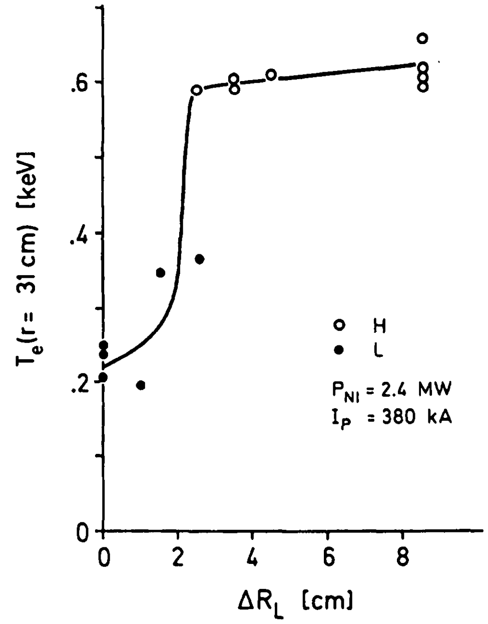

FIG. 69. Variation of the edge electron temperature when the outside poloidal limiter wing is moved to the plasma surface. The data points for ΔR_L = 0 are obtained from limiter discharges without energized divertor coils.

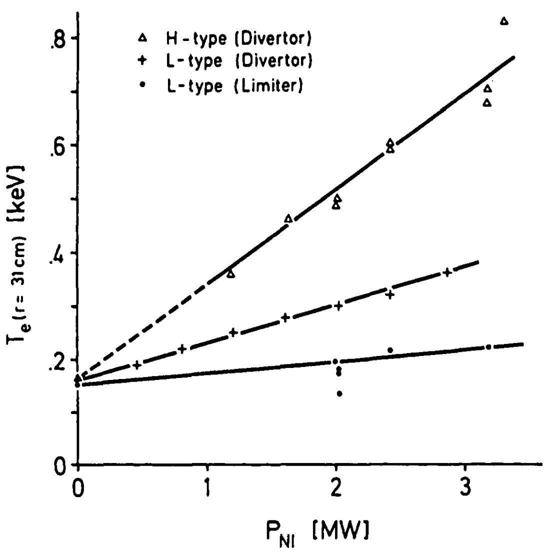

FIG. 70. Variation of the edge electron temperature with the beam power in limiter discharges and in L- and H-type divertor discharges. $I_p = 0.38$ MA, $\bar{n}_e \simeq 3 \times 10^{13}$ cm^{-3} (H), $\bar{n}_e \leq 2 \times 10^{13}$ cm^{-3} (L) and $\bar{n}_e \simeq 5 \times 10^{13}$ cm^{-3} (limiter).

6.1.2. Development of the electron temperature in limiter discharges

Different limiter configurations have been investigated, as discussed in the previous sections. All limiter discharges showed a deterioration of the energy confinement even in the parameter range of the H-mode. Exceptions were a few belt limiter discharges, as described in Section 4.3. Figure 69 shows the variation of the electron temperature at r = 31 cm when the outside limiter wing is moved towards the plasma surface. (The limiter position was changed from shot to shot; the divertor coils were deactivated only in $\Delta R_L = 0$ discharges.) At a plasma-limiter distance ΔR_L of ≤ 2.5 cm (roughly one to two density or temperature fall-off lengths in the SOL), the edge temperature decreases sharply and the H-regime is suppressed. The edge temperatures are a factor of about three lower in limiter discharges than in H-type divertor discharges. These results are also supported by Thomson scattering measurements at the edge, and a similar decrease of the edge ion temperature is observed.

In Fig. 70, the variation of the edge electron temperature (r = 31 cm) with the beam power in limiter discharges is compared with that in L- and H-type divertor discharges. A linear increase of T_e with P_{NI} is observed for the L- and H-type divertor discharges, while the limiter discharges show a very weak dependence on P_{NI}. The comparison indicates that the divertor configuration allows the edge temperature to evolve without constraints. In limiter discharges, however, there seems to be a mechanism (e.g. impurity erosion from the limiter, increasing with beam power) which keeps the edge electron temperature largely independent of the beam power, thus constituting an additional boundary condition. L-type divertor discharges (obtained by operating below the density threshold) also exhibit a linear increase of the edge electron temperature, but, even at the maximum available injection power, T_e remains below the threshold for the L-H transition. The low density case indicates that the H-mode might ultimately also be accessible but at a higher power.

6.1.3. Post-beam pulse H-phase

An interesting technique to unravel the crucial parameters for the L-H transition is to heat the plasma with a power just below the power limit. Operation under such marginal conditions increases the sensitivity because already small parameter changes, which hardly affect the global plasma conditions, have an impact on the

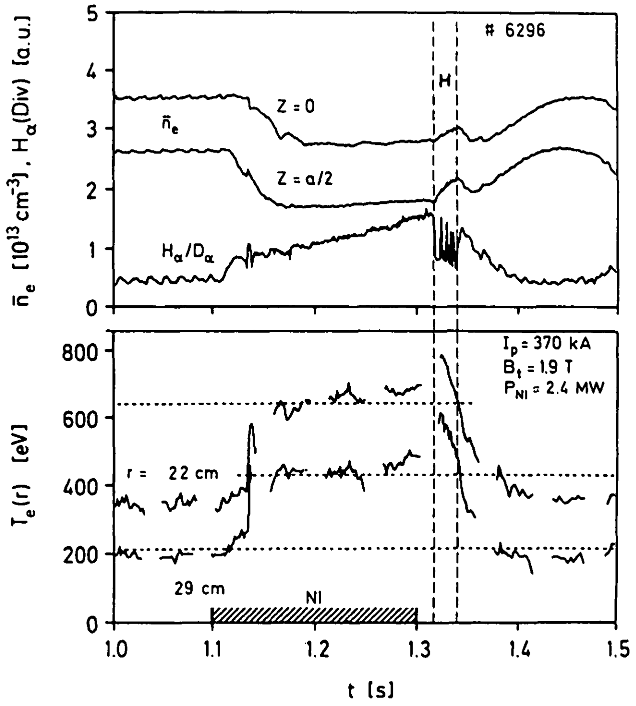

FIG. 71. Line averaged density at the plasma centre (z = 0) and along the chord z = a/2, H_α/D_α radiation in the divertor chamber, and electron temperature at two radial positions. The H-phase (between dashed lines) occurs after switching on the NI pulse during a phase of elevated temperature.

transition conditions. This technique has been successfully applied in different investigations.

For beam heated plasmas it is a common observation that the electron temperature rises transiently when the beams are switched off [73]. In the short phase following the beam pulse, when the orbiting beam ions still heat the plasma (slowing-down time ~ 15 ms), the heating per particle is suddenly improved when the flux of cold electrons injected with the beam atoms is terminated. This phenomenon has been dubbed 'post-beam pulse electron temperature rise' [73]. Figure 71 shows such a case with medium heating power where the H-phase develops shortly after the beam pulse is switched off. During beam heating the particle confinement is of the L-type. The H-phase is short because there is no auxiliary heating power, but it is long enough to be interrupted by a few ELMs.

6.1.4. Comparison of L-H and H-L transitions

Because of the confinement sequence OH-L-H-L-OH, the plasma properties at the L-H transition in the initial beam phase can be compared with the H-L transition after the beams are switched off. The comparison is only meaningful when the conditions for the two transitions are rather transparent, with a longer L-phase preceding the L-H transition and with an H-L transition that is not disturbed by ELMs. Such a case is shown in Fig. 72. The H-L transition occurs 40 ms after the beam pulse is switched off, in a phase where the plasma is cooling down. As indicated in Fig. 72, the transition back to the L-phase occurs roughly at the same peripheral electron temperature as the transition to the H-phase. All other plasma parameters and also the plasma profiles are widely different at these two moments. This observation indicates that it could be specifically the edge electron temperature which has to surpass a certain threshold for the L-H transition to occur.

6.1.5. Sawteeth as H-mode trigger

An interesting feature of the L-H transition is that it can be initiated by a sawtooth crash (see Section 2.3). Detailed measurements with good time resolution showed that the triggering of the H-mode by a sawtooth occurs when its thermal wave arrives at the plasma edge. This trigger mechanism, which has also been observed by other authors [5], is the most convincing evidence of the role of T_e at the plasma periphery (or of a parameter depending on it) in the L-H transition.

Generally, the transition to the H-mode occurs under non-stationary plasma conditions, when the edge electron temperature is still increasing. At low q and low injection power, the L-H transition can be triggered by a sawtooth. In Section 4.1, it is described how sawteeth can affect the dependence of the threshold power on the toroidal field. A sawtooth triggered L-H transition is shown in Fig. 12 in comparison with an L-type discharge. (The only difference between the two discharges is the vertical shift: the H-discharge is an upper SN discharge and the L-discharge is a lower SN discharge.) Figure 12 shows the edge temperature and the variation of the line averaged density $\bar{n}_e$ during the NI pulse for the two cases. Sawtooth disruptions appear as sharp drops in the density signal. As shown in Fig. 12 (arrows), the heat wave of a sawtooth increases T_e at the periphery, but, after its passage, T_e decreases again.

A sawtooth which causes the L-H transition also raises the temperature at the edge. Afterwards, however, the temperature does not decrease as in the case of a normal sawtooth but it remains at the high level and, in the course of the H-phase, it increases further as a consequence of the improved confinement. The heat pulse is dissipated in the plasma periphery. Actually,

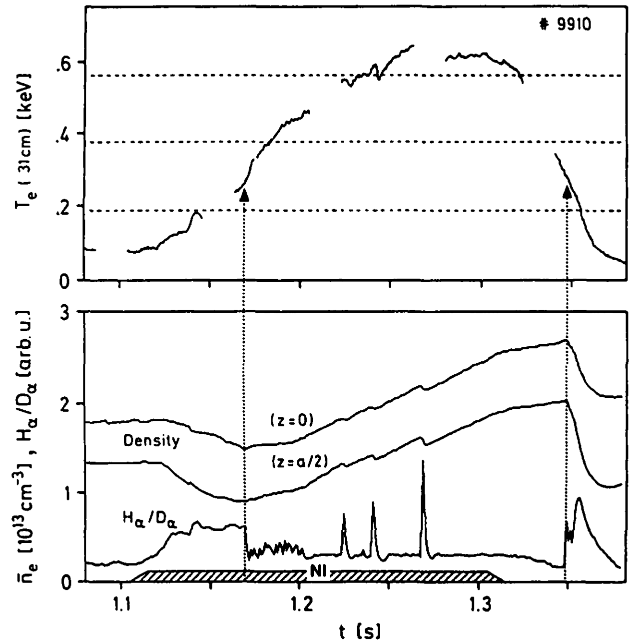

FIG. 72. Peripheral electron temperature, line averaged density along two chords, and H_α/D_α radiation in the divertor chamber during NI heating; the L-H and H-L transitions are indicated by arrows.

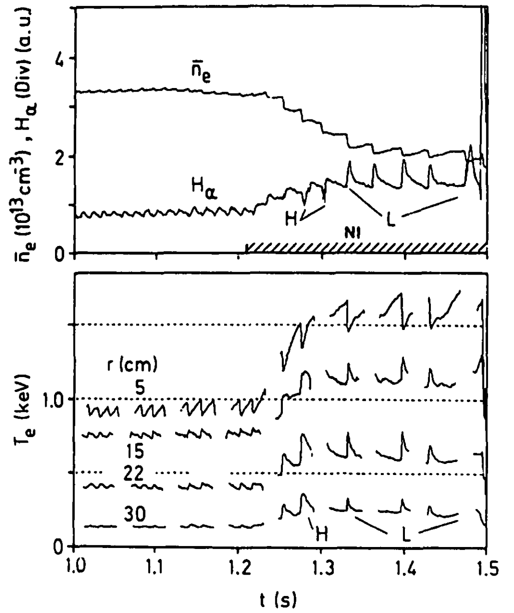

FIG. 73. Line averaged density, H_α radiation in the divertor chamber, and ECE electron temperature during an L-discharge with large sawteeth. Two sawteeth give rise to a short H-phase.

a sawtooth which triggers the L–H transition usually does not give rise to a thermal or particle pulse at the neutralizer plate as a normal sawtooth would do. Such a case is shown in Fig. 73, where the line averaged density $\bar{n}_e$, the H_α radiation in the divertor chamber and the electron temperature T_e are plotted at four different radii of an L-discharge with large sawteeth and a heating power close to the power threshold. The sawteeth modulate T_e in the known form of a reduction within the $q = 1$ surface and a pulse-like variation outside of it, caused by the thermal wave travelling to the plasma surface. The plasma density is modulated in a similar way. The sawteeth also modulate the H_α signal in the divertor chamber, causing a signal rise there which is very conspicuous during the beam heating phase. Two examples of sawteeth which behave differently are also shown in Fig. 73, namely large sawteeth (only one is documented by the T_e diagnostic) which cause an L–H transition. Comparison of the parameter variation caused by a sawtooth in the L-phase with that of a sawtooth triggering the H-phase reveals a distinct difference in the outer plasma zones but a rather similar behaviour in the plasma core. A regular sawtooth gives rise to a fast pulse-like temperature variation in the plasma periphery; the energy pulse travels across the separatrix, along the SOL into the divertor chamber and causes an increase of the H_α radiation there. A sawtooth correlated with an L–H transition leads to a slow decay of the temperature in the plasma periphery and a reduction of the divertor H_α radiation.

Although the results presented above indicate that the L–H transition is connected with the high edge electron temperature, it is not clear whether it is the temperature itself or a related quantity which causes the L–H transition. The different relative variations of T_e and n_e at the edge which depend on the recycling conditions (see Section 4.2) may indicate that a sufficiently high edge pressure is of importance.

6.2. Formation of a transport barrier at the plasma edge

In the previous section, the effect of a high electron temperature at the plasma edge has been discussed. At a sufficiently high T_e value, a transport barrier develops just inside the separatrix which impedes the outflow of energy and particles and initiates the H-phase [40]. The development of the transport barrier has been studied by applying the same techniques as described above, namely operation under marginal power conditions in the L-mode but with large sawteeth. The parameter changes in the plasma boundary have been monitored by the soft X-ray (SX) diode array* with high time and space resolution capabilities. As an example, two traces are shown in Fig. 74. Diode 1 views the SOL and diode 2 views mainly the plasma inside the separatrix. The distance between the two viewing lines is 2.5 cm. We compare the parameter changes due to two consecutive sawteeth — a regular one in the L-phase and a sawtooth which causes an L–H transition. The dynamics of the L–H transition becomes evident from Fig. 74 since the two events occur in sequence and only 50 ms apart. The thermal wave of a sawtooth during the L-phase causes T_e to increase first in the main plasma periphery and subsequently in the SOL, where the T_e variation modulates the SX signal. This signal variation after a sawtooth event is well known.

---

* The SX traces shown in Figs 74 and 75 are obtained with two SX cameras with different viewing geometries. The edge channels shown in Fig. 74 are vertical (see insert in Fig. 74) and those shown in Fig. 75 are tilted (see insert in Fig. 76). The advantage of this viewing geometry is that the actual position of the separatrix at the tangent point — obtained from equilibrium calculations — is known with higher accuracy (~0.5 cm instead of ~1 cm as in the midplane). The disadvantage of the tilted channels is that they measure the signals from both the plasma edge and the X-point (for the SN configuration it is the X-point formed by the outer separatrix) while the vertical chords are terminated at the vessel wall. This difference in viewing geometry may be the reason why the SOL signal is zero in Fig. 74 but decreases to a finite level in Fig. 75.

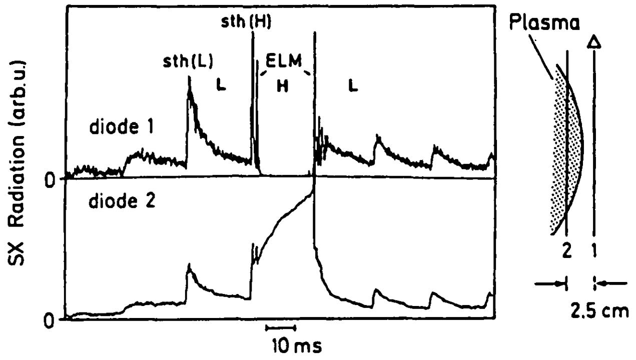

FIG. 74. Soft X-ray radiation during the L-phase with large sawteeth. Diode 1 views the SOL, diode 2 views mainly the plasma within the separatrix. One sawtooth, sth(H), gives rise to a transient H-phase.

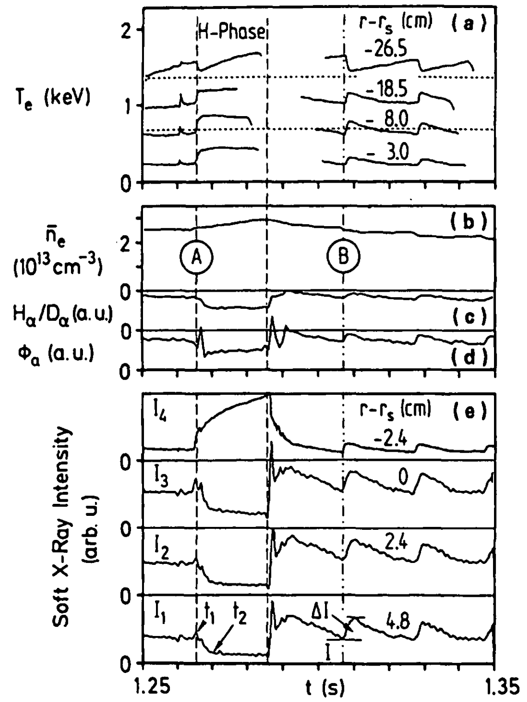

FIG. 75. Time evolution of (a) the ECE electron temperature (measured by electron cyclotron emission), (b) the line averaged density, (c) the D_α radiation in the divertor, (d) the reflected flux ϕ_a from the neutralizer plate, and (e) four SX traces from the plasma edge. (The ECE traces are interrupted by a chopper).

The large sawtooth which triggers an L–H transition, sth(H), gives rise to a totally different behaviour. The edge electron temperature does not show the transient variations caused by a passing thermal wave. The L–H transition occurs during the sawtooth rise, which is initially still measurable. At the instant of transition, the signal of the SX diode viewing the SOL sharply *decreases*. Within the separatrix, the sawtooth triggering the H-phase causes a continuously rising signal. Just after the transition an ELM occurs; an ELM also terminates the short H-phase.

Figure 75 illustrates the same sequence of sawteeth as shown in Fig. 74, with further SX channels. Also plotted are the electron temperature in the main plasma for four radial positions, the line averaged density $\bar{n}_e$, the H_α radiation in the divertor chamber and the atom flux ϕ_a emerging from the target plate. Supplementing the information of Fig. 74, Fig. 75 shows that the sawtooth triggering the L–H transition has a large T_e amplitude at the edge and the peripheral T_e value remains high throughout the H-phase, whereas the sawteeth in the L-mode show an evanescent behaviour. Also plotted in Fig. 75 are the power and particle fluxes into the divertor chamber which are due to a sawtooth and which modulate the H_α radiation and the atom flux ϕ_a in a pulse-like fashion. The different behaviour of these divertor signals is clearly indicated in the case of the sawtooth which triggers the L–H transition because now the power and particle fluxes into the divertor chamber associated with the sawtooth are blocked and H_α and ϕ_a decrease. The density during the H-phase rises.

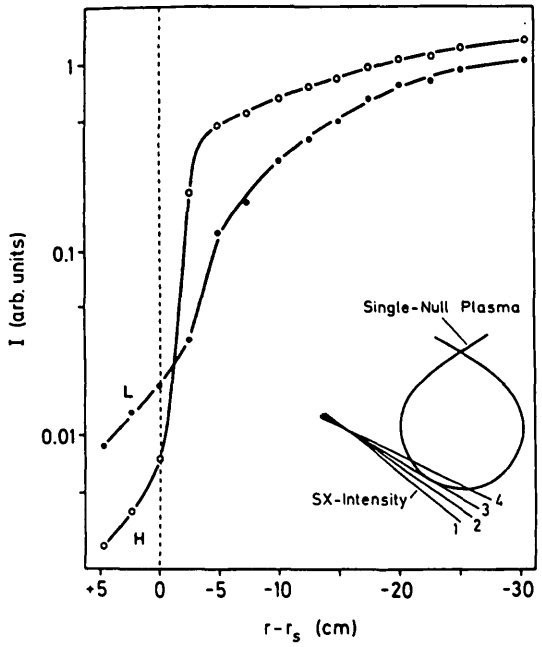

FIG. 76. Radial profiles of the SX radiation (2 μm Be filter) in the L-phase before the L–H transition and shortly afterwards at Δt = 20 ms. I_p = 375 kA, B_t = 2.2 T, $\bar{n}_e$ = 3.3 × 10^{13} cm^{-3}, P_{NI} = 0.8 MW. The insert depicts the observation geometry.

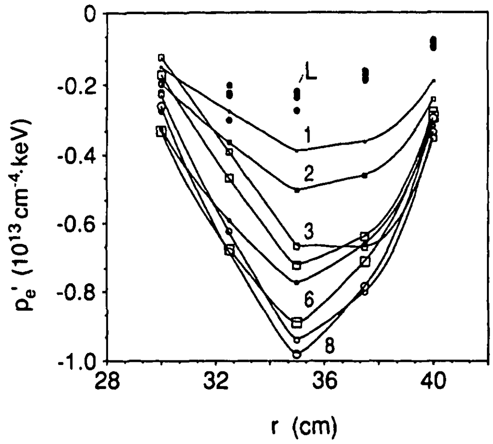

FIG. 77. Temporal development of the edge electron pressure gradient during the L-phase (circles) and during the quiescent H-phase (squares). The profiles are measured every 17 ms. After profile No. 8, the plasma transits back to a second L-phase.

The formation of a transport barrier, as discussed above, leads to reduced outflow of energy and particles into the divertor chamber, improved confinement properties of the the plasma and steep gradients at the plasma edge with subsequent occurrence of ELMs.

The drastic changes of the plasma profile at the edge as monitored by the SX diagnostic with the best spatial resolution are shown in Fig. 76. The SX radiation is given by the product of certain functions of n_e and T_e. A steep electron pressure gradient causes strong radial variation of the SX radiation. The profiles of Fig. 76 have been obtained just before the L–H transition and 50 ms thereafter.

The electron heat diffusivity in the edge transport barrier χ_e is about 5 × 10^3 cm$^2\cdot$s^{-1}, as calculated from the steep T_e gradient in Fig. 28 and the power outflux. This value is plotted in Fig. 40(b) together with χ_e as obtained from the transport analysis.

The radial extent of the edge transport barrier has been estimated from the rise in the edge pressure. Figure 77 shows the pressure gradient as it develops between the separatrix and 10 cm inside the separatrix. The pressure gradients during the preceding L-phase are shown for four time points (solid points). The first profile measured after the L–H transition is denoted by 1. The period between the succeeding profiles is 17 ms. The pressure gradient rises at the edge; the largest change occurs 5 cm inside the separatrix and there is no further change ~ 10 cm inside the separatrix. From these results and from similar observations in other quiescent H-phases it becomes obvious that the edge barrier first develops at the separatrix and subsequently expands inwards. The change in gradient caused by the transport barrier seems to reach typically 8 cm inside the plasma. This distance is longer than the shear length at the separatrix and also longer than the banana width of thermal particles at the edge.

6.3. Microscopic turbulence in H-phases

6.3.1. Density fluctuations

Neutral beam injection produces complex changes of the density turbulence, as observed by collective laser light scattering. The scattering system uses a 100 mW, 119 μm continuous wave CH_3OH laser and homodyne detection with a Schottky diode (for a detailed description see Refs [74, 75]). The wave number range is 2.5 cm^{-1} < $k_\perp$ < 25 cm^{-1}, with a resolution of ±1.25 cm^{-1}, and can be scanned in a single plasma discharge. Five chords with different distances from the plasma centre can be accessed per discharge (Fig. 78). The spatial resolution is ±1.6 cm perpendicular to the laser beam and chord averaged along the line of sight in the dominant wave number range $k_\perp$ < 10 cm^{-1}.

In the Ohmic phase the fluctuation spectra are found to be consistent with the assumption of a density gradient driven drift wave turbulence in a wide range of parameters [74, 75]. During NI heating the L-phase is in general characterized by an increase of the total scattered power compared with the Ohmic phase as well as a

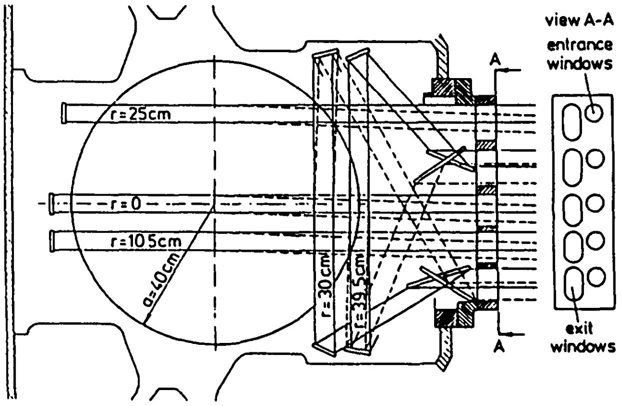

FIG. 78. Poloidal section of ASDEX, showing the beam paths inside the plasma vessel in the different chords and the window array. The distances from the plasma centre are 0 cm, 10.5 cm, 25 cm for the horizontal chords and 30 cm, 39.5 cm for the vertical chords. The scattered beams are schematically indicated by dashed lines.

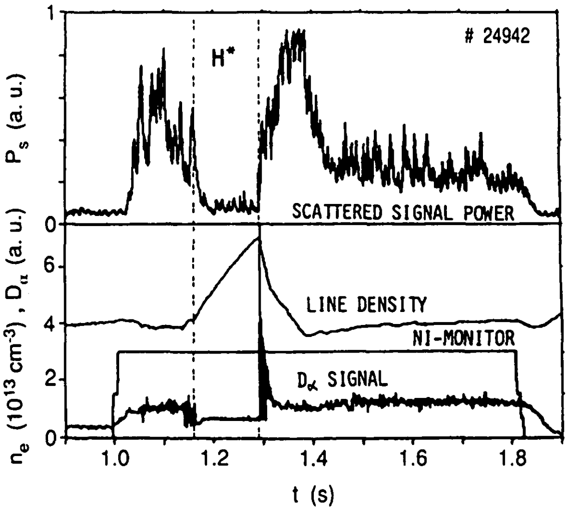

FIG. 79. Scattered signal power P_s measured in the equatorial channel for $k_\perp = 3\ \text{cm}^{-1}$. The frequency channel is 55-400 kHz. Also plotted in the lower part are the line density, the NI monitor and the D_α signal in the upper divertor chamber.

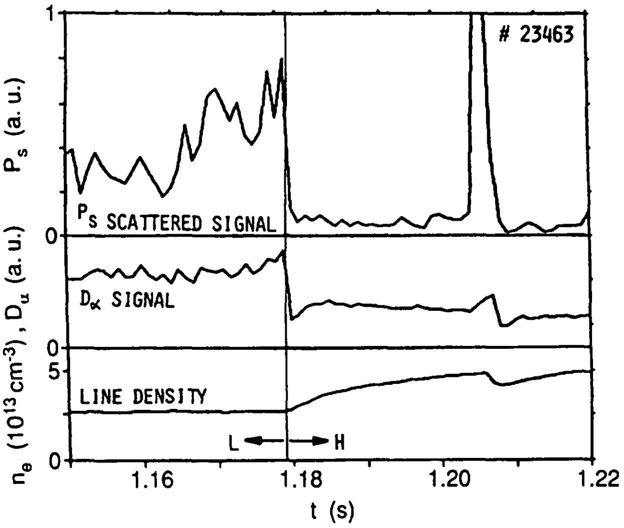

FIG. 80. Scattered signal power P_s measured close to the separatrix at the transition from an L-phase to a quiescent H-phase at $k_\perp = 3\ \text{cm}^{-1}$ (outer vertical chord). Also plotted are the D_α signal in the divertor and the electron line density 30 cm from the plasma centre.

dramatic broadening of the frequency spectra [74]. In addition, sawtooth activity strongly affects the scattering signals at low $k_\perp$ [75]. Coherent MHD modes during additional heating, as observed with Mirnov coils at frequencies up to 25 kHz, are obviously associated with low wave number density fluctuations, as observed on the FIR scattering signal.

In quiescent H-phases the total scattered power decreases significantly, to about the Ohmic level. This is illustrated in Fig. 79, which shows the temporal development of the frequency integrated scattering signal in a sequence of transitions, OH-L-H-L-OH, within one shot. The scattering signal of Fig. 79 was recorded at $k_\perp = 3\ \text{cm}^{-1}$. It was measured in the equatorial plane, where the scattering system views mainly poloidally propagating fluctuations. The low level of the scattered signal in the quiescent H-phase appears even more striking since it occurs during a pronounced increase of the mean electron density characteristic of this phase, which is also shown in Fig. 79. A similar behaviour was reported from a microwave scattering experiment on PDX [76]. On ASDEX, a clear decrease of the scattered power during transitions to quiescent H-phases was also observed at the plasma boundary near the separatrix, where the scattering system views mainly radially propagating fluctuations. This is illustrated in Fig. 80, which shows scattering signals measured when the scattering beam axis was located 1 cm inside the separatrix. A similar behaviour of the scattering signals was observed when the plasma position was shifted inside so that the scattering beam axis was located 0.5 cm outside the separatrix. A comparison with density profiles measured with the lithium beam probe in the separatrix region (see Fig. 81) rules out the possibility of explaining the reduced level of the scattering signals during the quiescent H-phase in Fig. 80 simply as the result of a density drop and/or a decrease in the density gradient length. In the sampling time interval of 1 ms the scattering signal power P_S decreases simultaneously with the drop

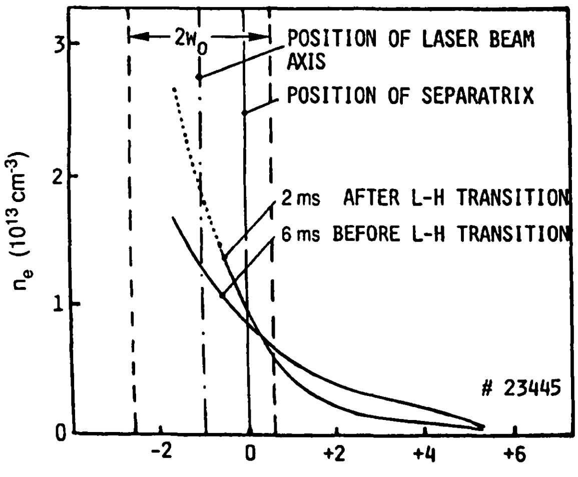

FIG. 81. Electron density profiles in the separatrix region before and shortly after the L-H transition (measured by a lithium beam probe).

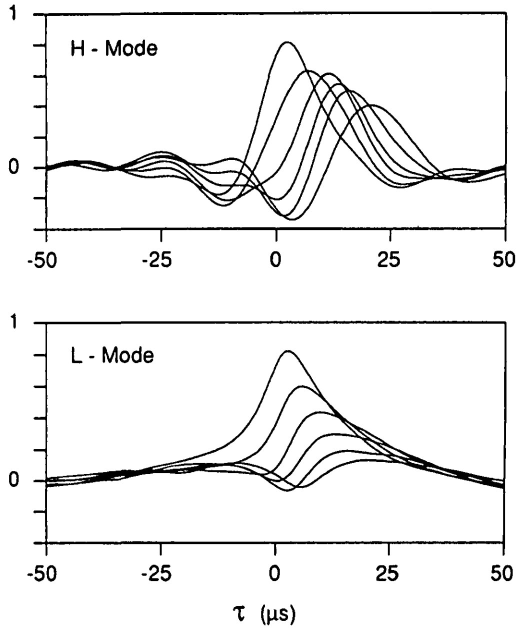

FIG. 82. Cross-correlation function of fluctuations in the H_α light between a signal channel and other channels at different separations, for L- and H-phases. The poloidal distance varies between 6 and 36 mm.

of D_α in the divertor chamber. The rapid drop of the fluctuation level at the edge is in clear contrast to the slower decrease of the core fluctuation level. At the L–H transition the frequency spectra broaden, showing a distinct increase at the high frequency end; this may be due to an increase in the poloidal rotation velocity of the plasma. In H-phases with ELMs the scattering signals are dominated by these modes and behave irregularly.

Further investigations are necessary to obtain a conclusive picture of the density fluctuation behaviour at the L–H transition. At present, it cannot be decided whether the lower fluctuation level during quiescent H-phases is the cause or the consequence of the improved confinement. It should be kept in mind that the density fluctuation level cannot be directly related to the transport since the potential fluctuations and phase angles are not known.

6.3.2. *Fluctuations of the H_α light emission*

Density fluctuations at the plasma edge have been investigated in regions of sufficient neutral hydrogen density by observation of fluctuations of the H_α light emission [77]. Cross-correlation functions and cross-power spectra have been calculated for pairs of channels separated in the poloidal direction by an integer multiple of 6 mm. A significant difference between L-mode and H-mode discharges is observed (see Fig. 82). While the cross-correlation functions for the L-mode are smooth and decay rapidly with increasing distance, those for the H-mode oscillate and decay much more slowly with increasing distance. Correspondingly, the cross-power spectra decrease monotonically in the L-mode and show a broad maximum (around 20 kHz) in the H-mode. The coherence between different channels in the frequency range of the maximum is much higher in the H-mode and decreases slowly with increasing poloidal distance. The phase difference between two channels increases rapidly with the distance, as expected for modes with short poloidal wavelength. These results also indicate that the key to the L–H transition may be found at the plasma edge.

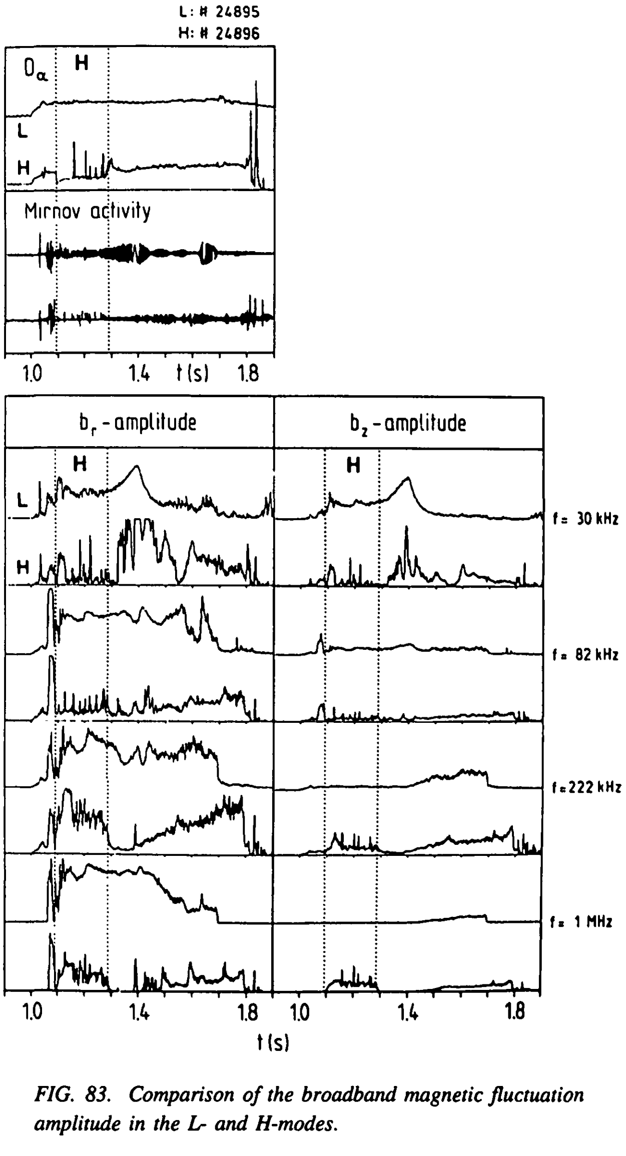

FIG. 83. Comparison of the broadband magnetic fluctuation amplitude in the L- and H-modes.

6.3.3. *Magnetic field fluctuations*

A set of coils, mounted on a pneumatically driven manipulator, has been installed on ASDEX. The manipulator can be used either to scan the probe over a distance of 8 cm in the radial direction within 150 ms during a discharge or to change the fixed position of the probe between discharges.

The radial, poloidal and toroidal components of the fluctuating magnetic field are measured simultaneously. A slotted graphite casing is fitted around the probe to provide electrostatic shielding of the coils, while magnetic fields can still penetrate. A passive high-pass filter is employed to attenuate the dominant coherent magnetic fluctuations due to Mirnov oscillations. The amplifier output is monitored by a frequency comb [78, 79] consisting of a splitter whose output is processed by a set of eight bandpass filters, each with $\Delta f/f = 0.1$. The RMS amplitude of the coil output is simultaneously measured at eight frequencies in the range of 30 kHz to 1 MHz.

From experiments involving sawtooth perturbation of the incoherent magnetic field fluctuation amplitude [80] it is concluded that the observed magnetic fluctuations are generated within a few centimetres of the separatrix. In addition, there is a significant increase in the ratio of the toroidal magnetic field fluctuation to the radial magnetic field fluctuation as the probe moves towards the separatrix. Further support for this conclusion is provided by recent experiments on TEXT, where magnetic field fluctuations measured outside the limiter radius have been found to be correlated [81].

Figure 83 shows the magnetic fluctuation amplitude in discharges with the same nominal conditions of I_p = 380 kA, B_0 = 2.17 T and $\bar{n}_e = 2.9 \times 10^{13}$ cm^{-3}, with 2.6 MW of H^0 injection into deuterium (Nos 24895 and 24896). The separation between the separatrix and the magnetic probe is 10 cm. Previously, broadband radial and poloidal magnetic field fluctuations during the H-mode were observed in ASDEX with probe coils located 17 cm from the separatrix [82].

The upper traces of Fig. 83 correspond to a discharge which remained in the L-mode and the lower traces correspond to a discharge which made a transition to the H-mode. The coherent magnetic fluctuations at t = 1.5 s are in the range of 15-25 kHz. These fluctuations have been identified with m/n = 4/1 Mirnov oscillations in the discharge which remained in the L-mode and with m/n = 3/2 Mirnov oscillations in the discharge which made a transition to the H-mode. At higher frequencies the broadband magnetic fluctuations are of smaller amplitude during the H-mode. After the L-H transition, a sharp decrease in amplitude of the f = 82 kHz component occurs (see Fig. 84), despite the increase in the amplitude of the coherent magnetic fluctuation as measured by the f = 30 kHz channel. This difference in behaviour suggests that the mechanism responsible for the generation of coherent fluctuations is not directly linked with the instability generating the fluctuations at higher frequency. Further investigations are required to determine whether the stabilization of fluctuations in the low frequency range is the cause or the consequence of the transition to the H-mode.

The observed amplitude increase of the radial and toroidal components of the magnetic field fluctuations in the higher frequency channels after the L-H transition suggests that a different mode has been destabilized. A comparison of the time dependence of the amplitudes at f = 30 kHz and f = 606 kHz (see Fig. 85) demonstrates that this process is independent of the presence of coherent magnetic fluctuations. Preliminary measurements with the probe positioned 4 cm from the separatrix show an even more dramatic increase of the toroidal component at high frequencies. The steep pressure

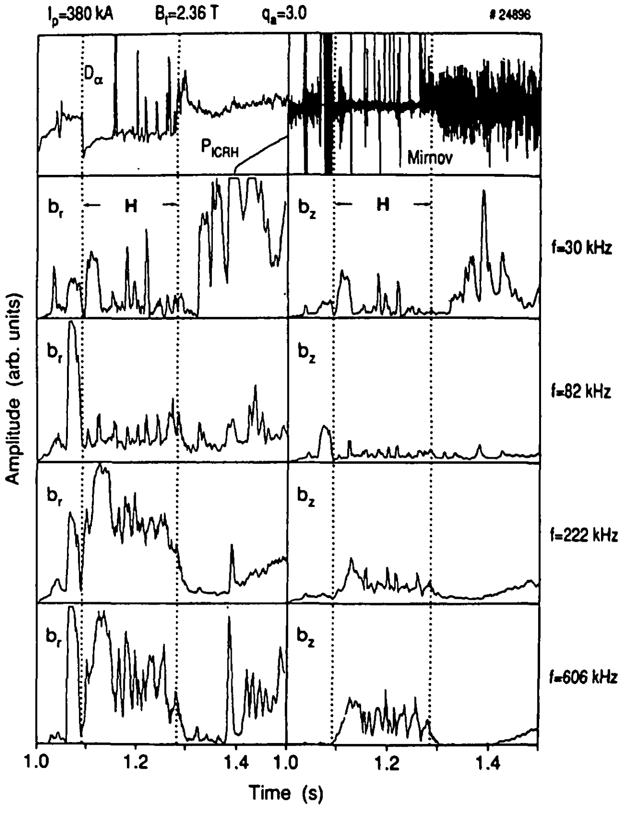

FIG. 84. Frequency dependence of the broadband magnetic fluctuation amplitude at the L-H transition.

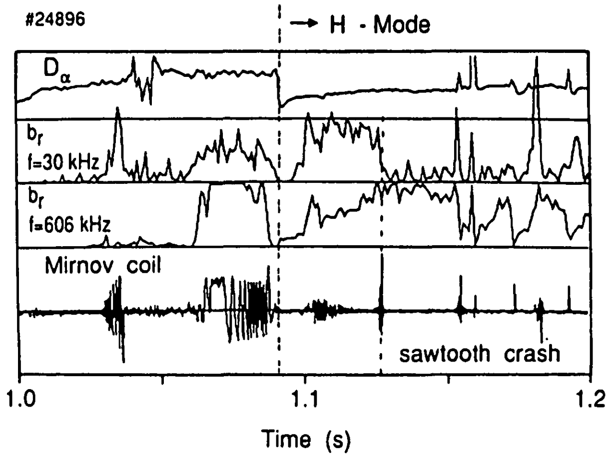

FIG. 85. Relation between the broadband magnetic fluctuation amplitude, the sawteeth and the emission of D_α radiation in the divertor.

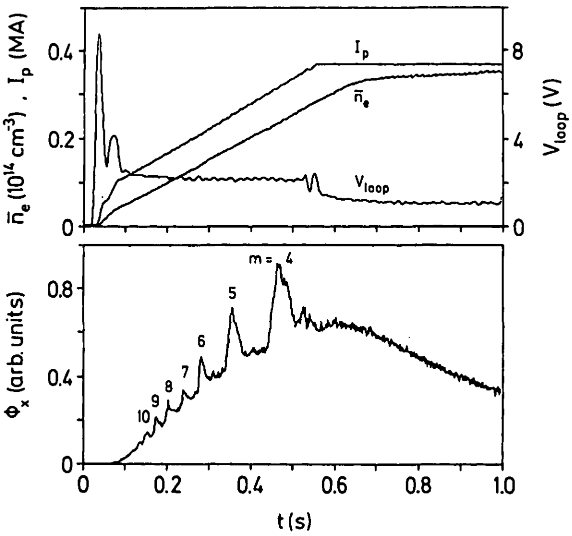

FIG. 86. Variation of the hard X-ray radiation ϕ_x during the initial discharge phase when the current is ramped up and rational q surfaces cross the plasma surface.

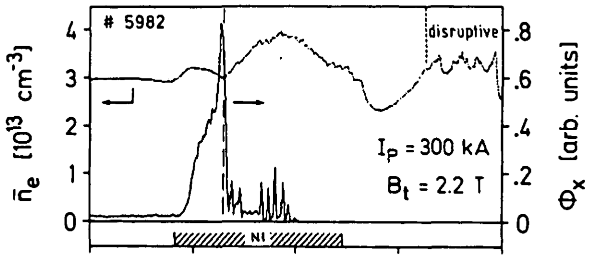

FIG. 87. Time evolution of the hard X-ray radiation with neutral injection and at the L-H transition. The line averaged density is given for reference.

gradient at the plasma boundary in the H-mode is thought to play a role in the generation of these fluctuations.

6.3.4. *Confinement of runaway electrons*

The confinement of runaway electrons depends sensitively on the quality of the magnetic configuration. They are measured via the hard X-radiation Φ_x which is emitted from a molybdenum target hit by runaway electrons. The target is placed outside the plasma in the midplane on the low field side. Runaway electrons are produced in ASDEX during the first 50 ms in the discharge breakdown phase; they are accelerated during the current ramp-up phase and are gradually lost during the plateau phase, thus defining a runaway confinement time τ_R from the exponential variation of Φ_x. The transient increase of Φ_x indicates increased runaway electron losses [83].

Figure 86 shows the variation of Φ_x during the current ramp-up phase. The transit of rational q-surfaces across the separatrix leads to increased runaway electron losses because the magnetic configuration is somewhat disturbed. The radial magnetic field component, which develops in the configurationally unfavourable situation of a rational q-surface at the plasma edge, is too small to affect the bulk plasma. When the plasma current and the toroidal magnetic field are chosen such that a rational low-q surface remains close to the plasma surface during the plateau phase, runaway electrons are quickly lost. The sensitivity of the runaway electron confinement to disturbances of the magnetic field configuration is highlighted by the fact that in such a case the sawteeth strongly couple to the runaway electron population, leading to strong sawtooth modulation of the hard X-radiation.

The confinement of runaway electrons is sharply degraded with auxiliary heating. At the L–H transition, however, the confinement of runaway electrons is again improved. The increase of the hard X-radiation in the L-mode and the sudden reduction at the L–H transition are plotted in Fig. 87 together with the line averaged density. According to this plot the L-phase is a state of high magnetic turbulence, while the L–H transition again leads to a quiescent phase.

Analysis of the runaway confinement time τ_R yields a radial correlation length of about 1 mm and a fluctuation level $\tilde{B}/B$ of $\sim 2 \times 10^{-4}$; together with the parameter dependence of τ_R, this indicates that resistive ballooning modes are the inherent turbulence. As a consequence of this analysis, we conclude that resistive ballooning modes can be stabilized under the specific edge conditions at the L–H transition.

7. MHD STABILITY ANALYSIS OF H-MODE DISCHARGES

It is of considerable interest to compare the measured MHD activity with theoretical calculations, since in this way more insight can be obtained into the physical mechanisms that govern the high poloidal beta phase of the H-mode. One tool for this investigation is the GA-3D-CART code [84], which is based on the large-aspect-ratio expanded MHD equations at finite poloidal beta, $\beta_p \approx R_0/a$, and is capable of treating the linear and non-linear evolution of ideal and resistive MHD instabilities (Section 7.1). Furthermore, free-surface instabilities related to the ELMs are studied in the framework of resistive MHD equations (Section 7.2).

Investigations of ideal and resistive ballooning modes have been stimulated by the observation of a 'hard' beta saturation near the maximum attainable beta, which is close to $\beta_c = 2.8\ I_p/a\ B_t$ [%, MA, m, T] [85, 86]. It is termed 'hard saturation' because it is distinguished by the absence of both sudden disruptions and gradual deterioration of the confinement over an extended range of beta. To explain this within the framework of MHD instabilities, ballooning mode stability analyses have been performed on ASDEX, which are discussed in Section 7.3.

7.1. Medium m-mode stability

The linear MHD equations of the CART code are solved for realistic ASDEX equilibria and plasma parameter profiles [87, 88, 89]. Before performing the stability calculations we determine the plasma and magnetic field configuration by solving the free-boundary equilibrium problem

$$R^2 \operatorname{div} \frac{\nabla\psi}{R^2} + \mu_0^2\, JJ'(\psi) + 4\pi^2\, \mu_0 R^2 p'(\psi) = 0$$

$$JJ'(\psi) = \frac{4\pi^2}{\mu_0} \langle 1/R^2 \rangle^{-1} \left(\frac{dI}{dV} - p'(\psi) \right)$$

for the poloidal fluxes of the magnetic induction (flux function ψ) and the current density on the basis of given profiles of pressure p and toroidal current I as function of $r/a = (V/V_p)^{1/2}$, embedding the plasma in the internal conductor system of ASDEX. Here, $\langle \ldots \rangle$ denotes the usual flux surface average and V_p is the total plasma volume. The magnetic field is then given by

$$B = \frac{1}{2\pi} (\nabla\psi \times \nabla\phi + \mu_0 J\, \nabla\phi)$$

Transport analyses (see Section 3.3) yielded profiles of the total plasma pressure $p(r,t) = p^{th} + 1/2\ (p_\parallel^{beam} + p_\perp^{beam})$, and — by solving the poloidal field diffusion equation — profiles of the current density $j_t(r,t)$.

We generally find that the global MHD activity is mainly caused by tearing modes or pressure driven modes. External kink contributions are weak for our cases ($\Delta\tilde{\gamma} < 10\%$), as can be shown by moving the conducting wall closer to the plasma surface. A change in the driving mechanism for the instability with increasing pressure is indicated by the η scaling of the growth rates, as shown in Fig. 88. It turns out that low β_p discharges scale as $\eta^{3/5}$, as expected for tearing modes, whereas for high β_p discharges an interchange mode scaling, $\tilde{\gamma} \sim \eta^{1/3}$, is found.

Usually, large poloidal mode numbers ($m \le 5$) are obtained which clearly exceed the q_a value at the boundary of an equivalent circular discharge at finite beta: $q_a \approx q_a^*(1 + \epsilon^2\ (1 + 0.5(\beta_{p\parallel} + \ell_i/2)^2))$, so that the resonant surface m = q should lie close to, but inside, the separatrix ($q_a^* = 5B_t\ r^2/(2\pi\ R_0 \int_0^r j_t\ rdr)$). An example is the high β_p discharge No. 18041 ($\beta_p \approx 1.92$) with $q_a = 3.4$ and a measured value of $m \approx 4$, $n = 1$. It turns out that a simulation of these results with constant vacuum resistivity η^* is impossible. This problem can be resolved by noting that small vacuum resistivities increase the effect of the perturbed

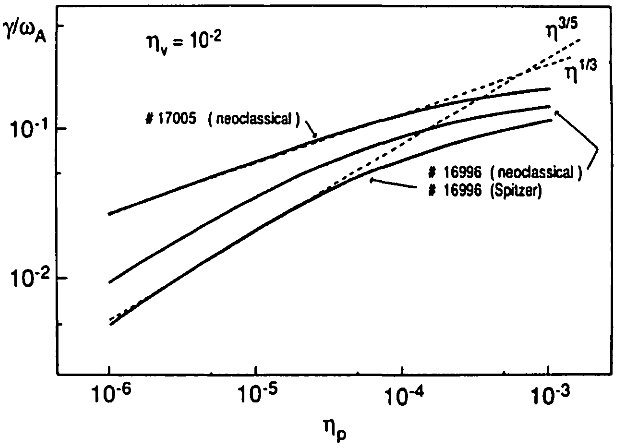

FIG. 88. Growth rates of medium-m resistive modes normalized to the Alfvén frequency as a function of the plasma resistivity η_p (the resistivity outside the separatrix is fixed at $\eta_v = 10^{-2}$) for a medium value of the poloidal beta, $\beta_p = 1.1$ (No. 16996), and a beta limit value, $\beta_p = 2.1$ (No. 17005). The influence of the plasma resitivity model is also indicated. The dashed lines represent the scalings $\gamma/\omega_A \sim \eta^{3/5}$ and $\eta^{1/3}$.

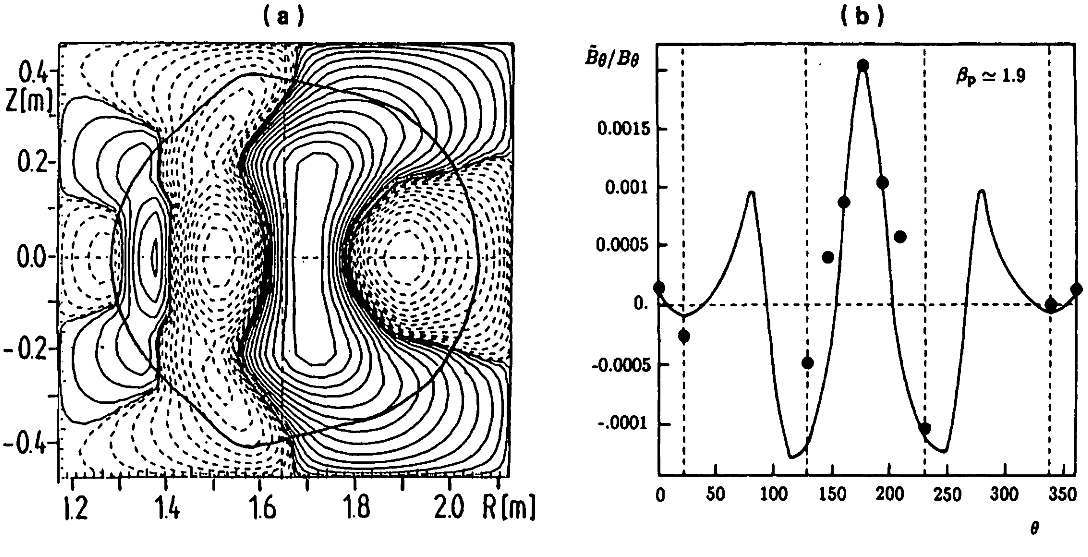

FIG. 89. (a) Perturbed magnetic flux contours for the unstable n = 1 mode of a discharge with $\beta/\beta_c = 1.0$. The solid line shows the magnetic separatrix.
(b) Comparison of the calculated magnetic fluctuation amplitude with measurements. The vertical dashed lines indicate the limited poloidal range covered by Mirnov probes.

current density on the evolution of the corresponding magnetic flux if we assume that the ratio of the convection term and the resistivity term depends only weakly on η_v^* ($\eta^* = (1/\tau_R\omega_A) \times (I/\pi r_p^2)/j$; $\omega_A = B_p/(r_p^2\ nm_i\ \mu_0)^{0.5}$; $\tau_R = \mu_0\ r_p^2/\eta$). Since

$$J = -\nabla_\perp^2 \psi \sim (m^2 + n^2)\psi_{m,n}$$

a stronger attenuation of the high-m contributions at the plasma surface than in the case with large η_v^* is expected. On the other hand, experimental data indicate a very effective insulation between the conducting wall and the plasma surface since high m-numbers persist close to the vacuum vessel. We have therefore increased η_v^* exponentially from its value at the plasma boundary to a high value near the wall ($\eta_{v,\mathrm{wall}}^* = 0.1$). This treatment naturally leads to stronger effects at the inner side of the torus, where the equilibrium magnetic flux is lower than at the outer side. As can be seen in Fig. 89(a) for discharge No. 18041 ($\beta_p \cong 1.9$), this procedure leads to the required large m-values as well as to the correct mode asymmetry, i.e. a smaller poloidal wavelength at the inner side of the torus.

For an even more detailed comparison with experiments, we have performed non-linear calculations, for which superposition of all Fourier components of the expansion in the toroidal direction is required. In practice, it turns out that three Fourier components are sufficient. The non-linear evolution is started with the corresponding linear n = 1 eigenfunction. Higher n-values are obtained by convolution with the n = 1 contribution. The amplitudes for the initial eigenfunctions have to be chosen such that the evolution remains in the linear phase for a few Alfvén times. Usually, since the Strauss equations in high beta ordering do not lead to true saturation in the non-linear phase, forced saturation by an effective pressure diffusion term has been used. The evolution is stopped as soon as the calculated perturbed magnetic field at the outboard side of the torus reaches the measured amplitude.

In Fig. 89(b), the numerical results for the perturbed magnetic field $\tilde{B}_\theta$ versus the poloidal angle at a fixed toroidal position after saturation in the non-linear phase are compared with the measured Mirnov signals. Because of the large outside–inside amplitude ratio, non-linear effects are stronger at the inner side of the torus. Comparison with data in the experimentally testable poloidal region shows reasonable agreement for the phases as well as the amplitudes.

The deviation of the observed soft X-ray wave forms from pure proportionality to sin ($n\phi$) can be regarded as a measure of non-linear effects. This gives the possibility of comparing the investigated saturation mechanism and the corresponding n > 1 contributions with the data. We have compared the measured time evolution of soft X-ray traces for discharge No. 18041 with calculations of the line integrated, squared, perturbed pressure. There is no frequency doubling in the central channel, indicating a weak $m = 1$ contribution, in agreement with experiment. Our results show that the phase differences of the various traces are reproduced with good accuracy. For this special case it turns out that the ratio of the $n = 2$ contribution to the $n = 1$ contribution is less than 10%. These effects turn out to be stronger at the inner side of the torus, mainly because of the large ratio of outside–inside amplitude.

In summary, global MHD stability calculations have been performed for H-mode, high poloidal beta discharges on ASDEX. It is shown that at high β_p the discharges are subject to a pressure driven tearing instability, whereas at low β_p the instability is mainly of the tearing type. When the vacuum resistivity is exponentially increased from its value at the plasma surface to a high value near the conducting wall, we find high poloidal mode numbers for the analysed high β_p discharges, in agreement with experimental observations. Non-linear calculations with forced saturation by an effective pressure diffusion term predict amplitudes of the non-linear contributions to the $n = 1$ eigenfunctions of the order of 10%. The calculations of $\tilde{B}_\theta$ versus poloidal angle and line integrated perturbed pressure are in reasonable agreement with experimental data from soft X-rays.

However, no clear correlation between the observed $n = 1$ mode activity and the beta limit or the beta decrease after maximum beta is reached can be found in the experiments [85]. The strong $m = 2$ mode sometimes observed during beta decay does not seem to be a prerequisite for this decay. If such a mode is present, its contribution to the beta decrease can be ascribed to the presence of magnetic islands (see Section 2.3.2). Finally, energy losses due to ELMs are also present in medium beta H-mode discharges without a beta decrease and are therefore not responsible for the additional losses at the beta limit.

7.2. Resistive MHD simulations of ELMs

The experimental evidence concerning ELM activity is described in Section 2.3.3 and can be summarized as follows:

- Only the outer part of the plasma is influenced by ELMs;
- The observed time-scale corresponds to the ideal MHD time-scale;
- There is no pronounced (m, n) precursor;
- ELMs are characteristic of H-discharges and are relatively independent of the value of the safety factor at the surface and of the poloidal beta.

Therefore, it seems necessary to begin a theoretical study by addressing the question of possible free-surface instabilities in the framework of resistive MHD. A small viscous term, $\mu\nabla^2\vec{v}$, is included in the momentum balance to obtain smooth profiles. For numerical convenience, the continuity equation is replaced by $\rho = \mathrm{ct}$. If the velocities are low, the corresponding error is quite small. The simulation is restricted to cylindrical geometry. Details of the numerical method and the code are found in Ref. [84].

The L- and H-discharge profiles displayed in Fig. 90 have been used as experimental data. The aspect ratio R/a is 4.0 and the resistivity is const. $\eta^* = 10^{-6}$. Typically, the value of the safety factor varies from unity on axis to 3 at the boundary. The parameters for the H-discharge are: $q_0 = 1.2$, $q_a = 2.8$ and $\beta_p = 1.8$.

The linear stability analysis yields a survey of possible instabilities related to ELMs. Clearly, a global ($m = 1$, $n = 1$) type mode is not involved ($q_0 > 1$). According to the analysis, there is a large number of unstable modes localized near the surface, such as ($m = 3$, $n = 1$), ($m = 8$, $n = 3$) and ($m = 15$, $n = 5$). The resonant surface at $r = r_s$ is defined by $q_s = m/n$. The growth rates scale as $\eta^{1/3}$ and hence these instabilities are basically pressure gradient driven. For the profiles of the H-discharges these modes are more pronounced owing to the large gradients near the surface.

Free-surface modes are studied in a system where the main plasma is surrounded by a force free

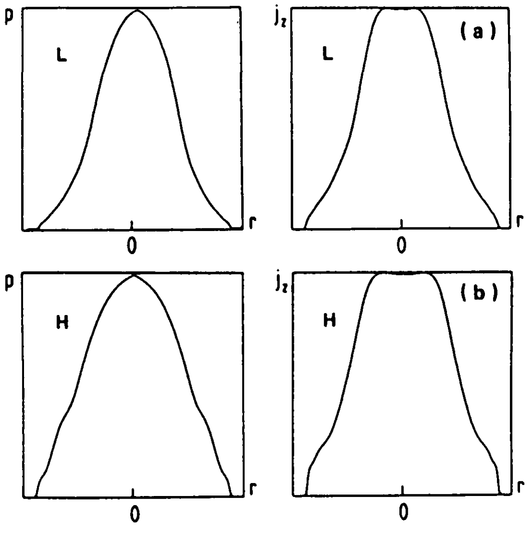

FIG. 90. Pressure and current profiles of (a) an L-discharge and (b) an H-discharge. The gradients are stronger at the surface.

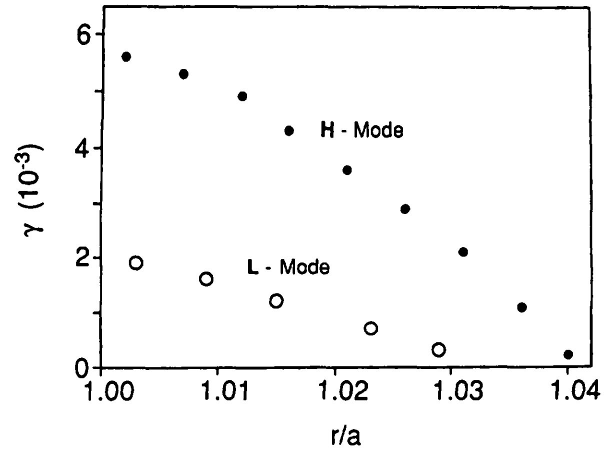

FIG. 91. Growth rate of an m = 8, n = 3 mode (normalized to the Alfvén time) versus the location of the resonant surface (r/a = 1 denotes the plasma boundary). The upper curve corresponds to the H-discharge and the lower curve to the L-discharge.

(currentless and pressureless) plasma with high resistivity η_v^* up to a perfectly conducting wall at $r = r_w$. This system has stability properties similar to those of a plasma–vacuum system but it yields a more realistic description. New instabilities are found when the resonant surface is outside the plasma. These modes are a mixture of kink modes and resistive interchange modes and are both current driven and pressure gradient driven. Their growth rates saturate for $\eta_v^* \sim 10^{-4}$ to 10^{-3}. It is emphasized that the ideal peeling mode is stable. Hence, these new instabilities can be considered as resistive peeling modes. If the resonant surface is too far outside the plasma, the mode becomes stable, as indicated in Fig. 91. Again, this surface mode is more pronounced in H-discharges. For a sufficiently close wall, $r_w/r_p < 1.1$, this free-surface instability is stabilized.

The non-linear evolution of the free-surface mode instabilities has been analysed by numerical simulation. It is of great importance to find out whether such localized modes are easily stabilized and saturate or whether they grow significantly when there are changes in the equilibrium. For this purpose, we have studied up to 36 modes corresponding to wave numbers m and n with resonant surfaces in the region $0.7 < r_s/r_p < 1.1$. Here the resistivity follows the temperature profile as $\eta \sim 1/j$, with $\eta^* = 10^{-6}$ on axis and $\eta^* = \eta_v^* = 10^{-3}$ outside the hot plasma ($r/r_p > 1$). The wall is placed at $r_w/r_p = 1.1$. It is found that for H-type profiles the surface modes interact and enhance each other; the plasma expands radially in about 20 μs ($150\tau_A \sim 20$ μs). This is shown in Fig. 92. The mode dominant in the linear phase amplifies other modes, such as the (m = 3, n = 1) mode, to make their contributions equal. A mixture of these modes yields the observed incoherent structure. In contrast, for L-discharges it is impossible to obtain the non-linear growth of the corresponding instabilities in a time-scale of up to 400 μs. The linear instabilities are too weak and too localized and are therefore easily suppressed by local changes in the equilibrium.

It is concluded that in H-discharges non-linear MHD modes may lead to an expansion of the plasma by about 4 cm radially, i.e. 10% of the plasma radius, and to a shift of an internal plasma ring to the separatrix, where the energy and particles are transported to the divertor. The experimentally measured energy which is transferred to the divertor plates during one ELM event corresponds to the energy in an outer plasma ring of 3–4 cm width. Thus, within this model, we arrive at the following scheme for repetitive ELMs: Strong pressure and current gradients near the plasma surface induce free-surface MHD instabilities. The plasma is enlarged by 4 cm (10% of the radius) in about 20 μs. A small plasma ring is shifted to the separatrix, and the energy and particles are carried into the divertor. Afterwards, flatter profiles lead to MHD stability, but the intrinsic H-mode transport again builds up strong gradients at the plasma edge.

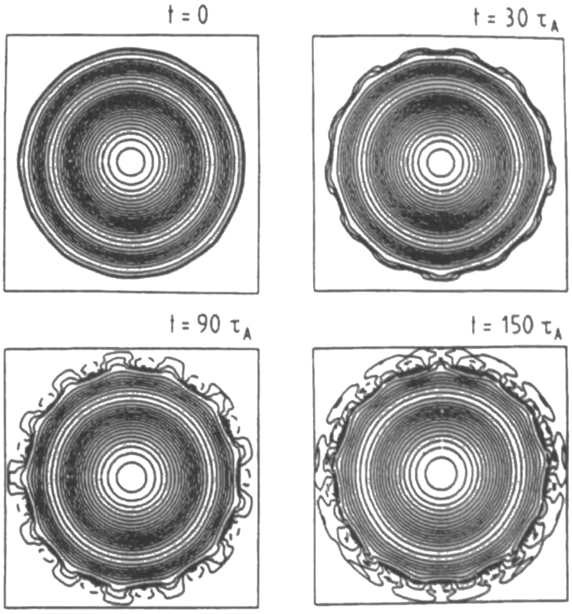

FIG. 92. Contour plots of the pressure for the non-linear evolution of free-surface modes.

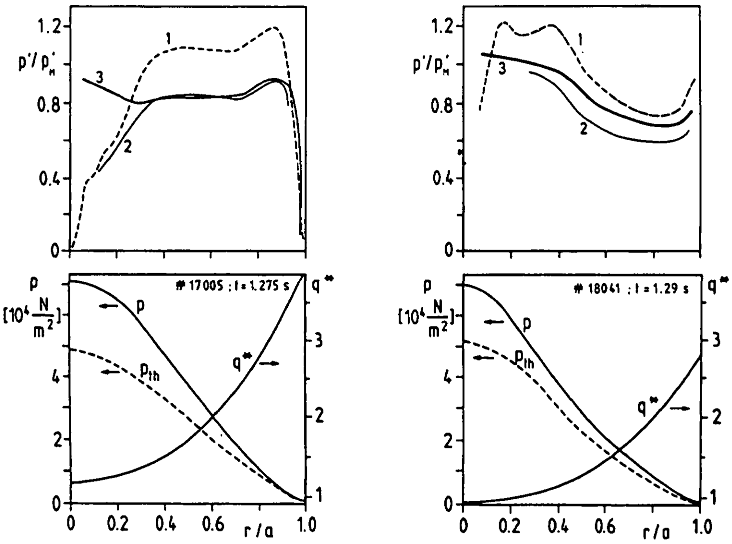

FIG. 93. Radial dependence of the pressure gradient p' normalized to the marginally stable gradient p_M' *due to the ideal ballooning modes, according to the* $\alpha(s)$ *criterion (1), a large-aspect-ratio expansion (2) and an exact solution (3), together with the pressure and q-profiles used for a* $D^0 \rightarrow D^+$ *discharge (No. 17005) and an* $H^0 \rightarrow D^+$ *discharge at* β_{max}.

This simulation has been performed in a straight, cylindrical geometry. The pressure gradient driven resistive instabilities, which combine with kink-type motions, stand for resistive ballooning modes with wave number m ~ 3–20. Similar instabilities can be expected to occur in toroidal geometry. Toroidal effects enhance the coupling, especially with kink modes (see Section 7.1). The divertor geometry of ASDEX has not been taken into account, i.e. the shear close to the separatrix is increased in relation to this model, but ergodization of the field lines near the separatrix may again diminish the effect of the X-points.

7.3. Ballooning stability calculations

As a first result of our calculations of ideal ballooning mode stability of MHD equilibria reconstructed from ASDEX experimental data [38], it is found that in a plasma configuration with a relatively small aspect ratio ($A \approx 4$) toroidal curvature, the large differential displacement of the magnetic surfaces at high poloidal beta, and the effects of local and global shear in the neighbourhood of the separatrix play an important role in the derivation of quantitative results. In general, accurately calculated MHD equilibria and a correspondingly careful treatment of the stability equations are required.

7.3.1. *Ideal ballooning modes*

In an ideal ballooning mode stability analysis of ASDEX equilibria the corresponding Sturm-Liouville problem has been solved for magnetic surfaces with volume values $0 < V < V_p$, where V_p is the total plasma volume. For a particular magnetic surface the ballooning equation for the unstable mode u depending on the poloidal angle θ can be written in the form

$$\frac{d}{d\theta}\left\{S(\theta)\frac{du}{d\theta}\right\} + \beta_p\,(C_1(\theta) + \beta_p C_2(\theta))\,u = 0$$

This ballooning equation is conceived as having an explicit dependence on the local poloidal beta and an implicit dependence (through the coefficients S, C_1 and C_2) on the total equilibrium. To obtain information on the presumably attainable marginal value, we have modified the explicitly appearing local poloidal beta on the basis of a given equilibrium configuration until a marginal solution of the ballooning equation with a poloidal beta value β_M was obtained.

Figure 93 shows the calculated beta ratio, $\beta_p/\beta_M = p'/p'_M$ (with the prime indicating $d/d\psi$), as a function of r/a for a $D^0 \rightarrow D^+$ discharge and an $H^0 \rightarrow D^+$ beta limit discharge ($\beta = \beta_c$) at the time of maximum beta. Besides a general evaluation of the

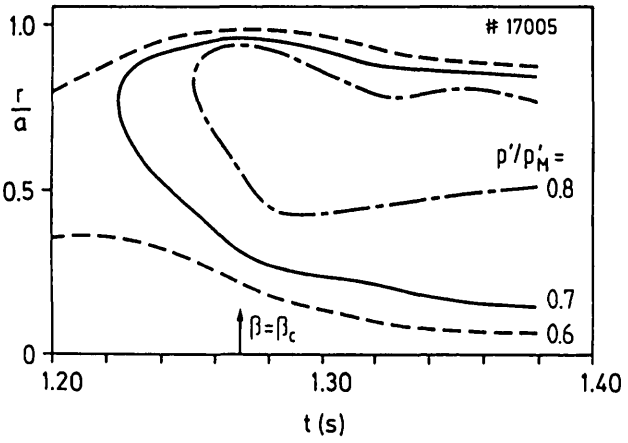

FIG. 94. Time evolution of the pressure gradient p' normalized to the marginally stable gradient p'_M due to ideal ballooning modes (large-aspect-ratio expansion) for $D^0 \rightarrow D^+$.

above ballooning equation, we have also performed a large aspect ratio expansion of the coefficients S, C_1 and C_2. Although we have assumed circular flux surfaces, we have taken into account the correct differential displacement of the magnetic surfaces due to the toroidal curvature, the poloidal beta and the internal inductance ℓ_i. This treatment is different from that discussed in Ref. [91], where the normalized pressure gradient α and the shear s are the only free parameters of the problem. Our treatment is also different from that discussed in Ref. [92], where a special functional form of the differential displacement was assumed. Except in the neighbourhood of the magnetic axis, we find that the results of our large aspect ratio expansion are in good agreement with those of the complete treatment; these refined approaches yields, however, β/β_M values about 20–30% lower than those given by the simple α–s criterion when $p' = dp/d\psi$ is in the vicinity of the marginal limit (see Fig. 93). Broader current density profiles with higher q_0 values are more susceptible to ballooning instabilities owing to their lower shear, and vice versa. For given q profiles, this can be demonstrated by variation of the β/β_M profile rather than by an increase of its maximum value, which is always below 0.9 for the range $0.8 \le q_0 \le 1.2$.

The time development of the ideal ballooning stability according to the large aspect ratio expansion in the $D^0 \rightarrow D^+$ beta limit discharge is illustrated in Fig. 94. At the time of maximum beta (about 1.26 s), the discharge reaches a normalized pressure gradient, $p'/p'_M = 0.8$, in the region $0.5 < r/a < 0.9$. This is also the region where additional increased plasma losses start according to the TRANSP analysis (see Section 3.3), causing a decrease of beta in the period 1.28–1.38 s. During this time the $p'/p'_M = 0.8$ region shrinks only slightly, but the maximum value of p'/p'_M stays below 0.9. When a general evaluation of the ideal ballooning equation is made for $0.15 < r/a < 0.85$, a region with p'/p'_M values between 0.7 and 0.85 is obtained for the period of the beta decrease.

To keep the plasma close to marginal ideal ballooning stability, the current profile has to flatten on a time-scale that is smaller than the resistive time-scale for current redistribution, assuming a time independent flat Z_{eff} profile. The computed internal inductance also decreases more slowly than the measured one. Better agreement of the time-scales has been obtained by using neoclassical resistivity together with a sawtooth model and with the measured or inferred Z_{eff} profiles (from consistency checks with radiation profiles and spectroscopic measurements) [38].

When bootstrap and beam driven currents are taken into account, it is found that only small changes in the current, the safety factor and the shear profiles occur on time-scales much shorter than the resistive time of 400 ms. It is found that ideal ballooning stability is left almost unchanged by the non-ohmically driven currents in the pre-transition L-phase, in the H-phase with and without ELMs and at the beta limit [10]. Figure 95 presents an example for the analysis of ideal ballooning stability in an H-discharge, with neoclassical resistivity

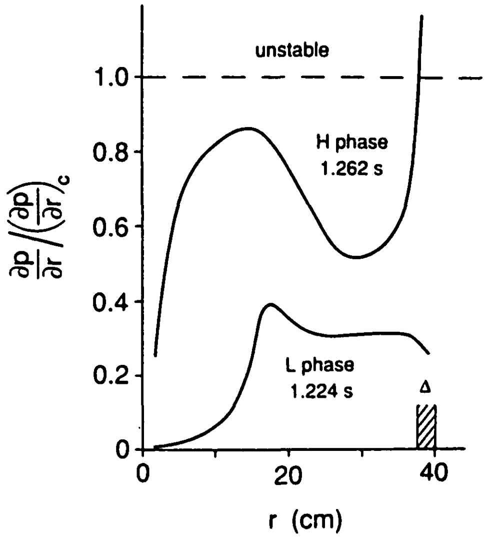

FIG. 95. Pressure gradient normalized to the critical value for ideal ballooning modes versus radius in L- and H-phases, with Ohmic, bootstrap and beam-driven currents included. Δ denotes the width of the steep gradient zone.

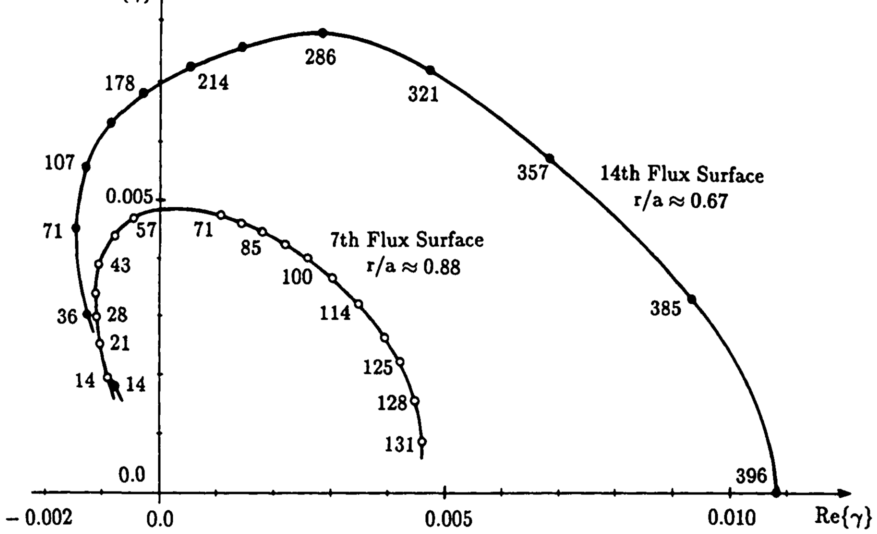

FIG. 96. Branches in the complex γ plane for the 14th flux surface (r/a ≈ 0.67) and the 7th flux surface (r/a ≈ 0.88). The latter surface corresponds to the one that is most unstable to ideal ballooning modes. The numbers at the curves label the various toroidal mode numbers.

and Ohmic, bootstrap and beam driven currents taken into account. During the L- and H-phases the plasma is stable, and even at the beta limit it is still marginally stable to ideal ballooning modes.

Finally, it should be remembered that, as noted in Section 3.3, in discharges with $\beta_{max} < 0.8\beta_c$ the p'/p'_M values remain significantly below unity, the maximum values being smaller than the corresponding global β/β_c ratio.

In ASDEX H-mode discharges the resistivity is very small but finite, so that actually the modes to be studied are resistive ballooning modes. In addition, the destabilizing potential of ideal ballooning modes turns out to be too small to account for the 'hard β_p saturation'. These circumstances motivated us to extend the investigations to resistive ballooning modes in the framework of the one-fluid MHD theory.

7.3.2. Resistive ballooning modes

In this approach we have assumed infinite parallel electron heat conductivity, i.e. constant temperature on a flux surface. However, as pointed out in Ref. [91], the mean free path of the electrons in ASDEX is of the order of 10^3 cm. The mean free path thus turns out to be much larger than the parallel wavelength of the resistive ballooning mode. Nevertheless, the ballooning modes cannot be stabilized by finite electron heat conductivity, as shown in Ref. [94] in the context of the Braginskij two-fluid model. In line with these arguments, we believe that electron heat conduction does not qualitatively change our results and so we postpone the investigation of extended dissipative/kinetic effects on ballooning modes.

On the basis of the resistive hydromagnetic equations we revisited the resistive evolution of velocity and magnetic fields in the high-m stability limit. For the Fourier approximation of this set, which leads to the resistive ballooning equations of Ref. [95], we then performed a numerical solution by applying a variational method to the corresponding boundary value problem in four dependent variables, with real and imaginary parts of the growth rate as parameters. The stationary values of the corresponding Lagrangian L are associated with the growth rates of resistive ballooning modes. Their actual values are uniquely determined by the experimental input of p(V), I(V) and η(V), and by the magnetic field configuration (see Section 7.1).

For purely growing modes, resistive effects are usually significant only if the parameter $n^2\tau_A/\tau_R$ is sufficiently large (τ_A is the Alfvén time). In regions close to the plasma centre the required values for n may exceed 100. If we allow overstable solutions, however, we find that much smaller values of n are associated with unstable modes. Our calculations show that the critical n-value strongly depends on the compressibility. Thus we find that for $n < n_c$ the compressibility term in the resistive ballooning equations dominates, whereas for n > n_c the resistivity terms take over.

Accordingly, we find that with decreasing c_p/c_v the critical n-value decreases. Figure 96 presents examples of the 14th flux surface ($r/r_p = 0.67$) and of the 7th flux surface ($r/r_p = 0.88$) which is most unstable to ideal ballooning modes; the corresponding branches in the complex γ-plane for discharge No. 17005 are plotted. The numbers specify the corresponding values of n. The bifurcation to overstability occurs at $n_c \approx 396$ for the 14th surface and at $n_c \approx 135$ for the 7th surface. Figure 96 demonstrates that for these flux surfaces the n values can be significantly decreased to $n \approx 140$ and $n \approx 60$, respectively, before the ballooning stability limit ($\mathrm{Re}\{\gamma\} = 0$) is reached. This result agrees well with our expectations for reasonable n-values in the context of a hydromagnetic approach.

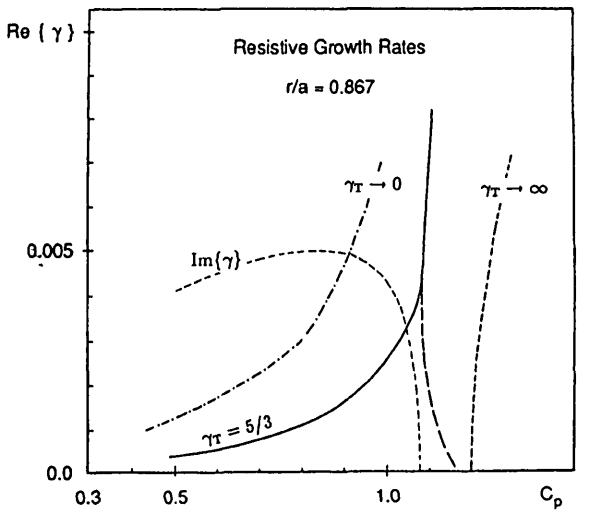

FIG. 97. Resistive growth rate (= Re(γ)) versus the pressure gradient scale factor C_p (= dp_M/dp). The curve relevant to ASDEX is the solid line.

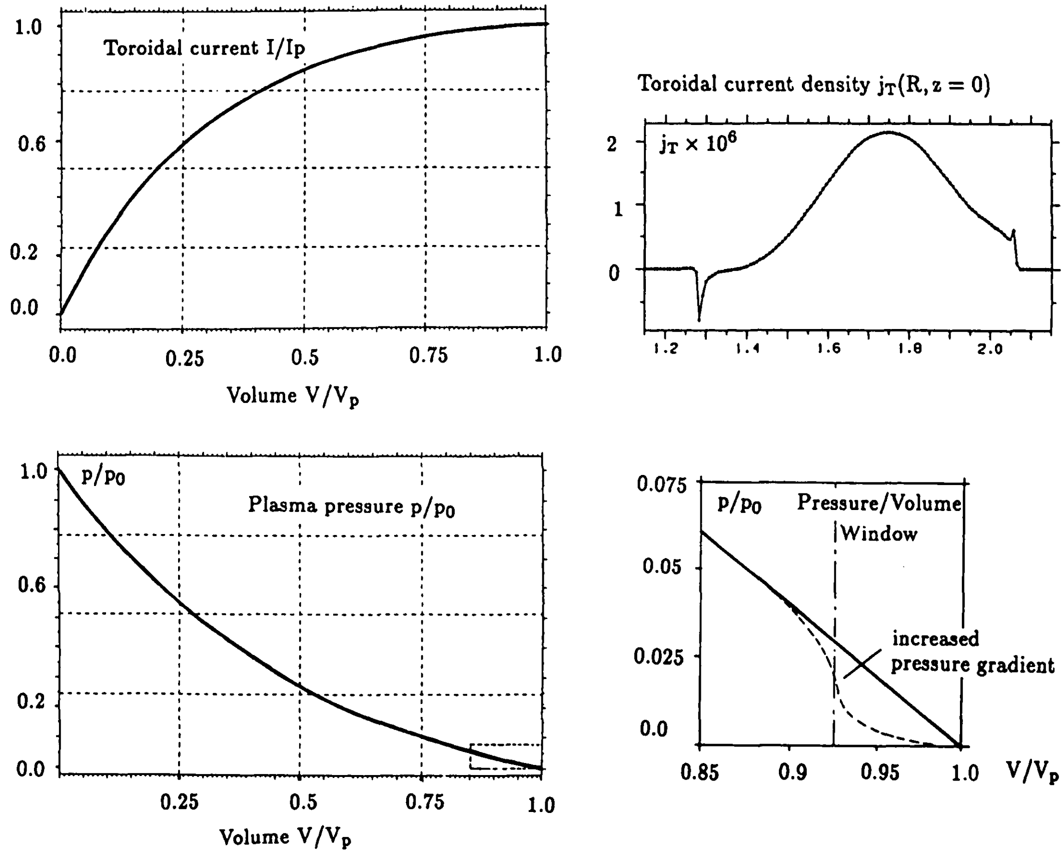

FIG. 98. Toroidal current and plasma pressure as functions of the normalized volume V/V_p, for discharge No. 17005 (I_p is the plasma current, p_0 is the pressure on the magnetic axis and V_p is the plasma volume). Pressure profile steepening in the plasma edge region, as indicated in the enlarged pressure volume window, results in the radial current density distribution shown in the upper right corner.

To investigate the signatures from resistive ballooning modes, we calculated the normalized growth rate γ as a function of the pressure gradient scale factor $C_p = dp_M/dp$ ($\nabla p_M = (dp_M/dp)\nabla p$, with $p_M(p)$ being the modified pressure profile), which was chosen such that $C_p = 1$ reproduces the equilibrium values at the global maximum poloidal beta [96]. Results for $\mathrm{Re}\{\gamma\}$ versus C_p are shown in Fig. 97 for $n = 100$; all curves refer to the 7th flux surface. The effect of compressibility can be seen in Fig. 97 by comparing the dotted curve and the short-dashed curve, which are for the totally compressible case ($\gamma_r \rightarrow 0$) and the incompressible case ($\gamma_r \rightarrow \infty$), respectively. In agreement with theoretical expectations, the incompressible plasma is more stable; furthermore, a pressure gradient threshold appears.

There is a strong increase of the growth rate when the poloidal beta approaches its maximum, i.e. $C_p \simeq 1$ (see Fig. 97). This is due to the transition from a region where resistivity effects dominate ($C_p < 1$) to a region where the growth rate is essentially controlled by the pressure gradient ($C_p > 1$). These regions are separated by the 'knee' in the dotted curve, which, furthermore, defines the transition points from purely growing modes to overstable modes.

All results discussed above refer to Δ'-like solutions which can be approximated by invoking the Δ' criterion of resistive ballooning modes [97, 98], i.e. these modes are fed by energy from the ideal region. In addition to these solutions we also find electrostatic branches [99].

Dispersion relations for such modes can be derived in a limit where the growth rate is much larger than the sound frequency. Since these modes are driven by energy from the resistive layer, we expect them to be of importance in regions of large resistivity or close to the plasma edge. There, the corresponding growth rates for these modes are comparable with those of the Δ' branch. Inspection of the dispersion relation reveals that the growth rate of these modes decreases with increasing plasma pressure (β); therefore, in regions where the plasma pressure is low but the pressure gradient is large (H-mode) we expect electrostatic modes to be important.

To prove these statements, we have performed calculations with a modified, increased pressure gradient in the plasma edge region. Figure 98 shows on the left side the unmodified profiles of the toroidal current, I/I_p, and the plasma pressure, p/p_0, as functions of the normalized volume, V/V_p. The small pressure-versus-volume window on the p/p_0 profile near the plasma boundary is shown enlarged on the bottom right side. This insert illustrates how the pressure gradient is successively steepened on the particular magnetic surface with $V/V_p = 0.925$. Growth rate calculations based on a correspondingly scaled sequence of plasma equilibria are shown in Fig. 99. The results demonstrate that, despite an increased pressure gradient, ASDEX is unstable but is far from the second region of stability, that the Δ'-like modes and the electrostatic modes have comparable growth rates, and that for even smaller beta values electrostatic modes may dominate Δ'-like modes.

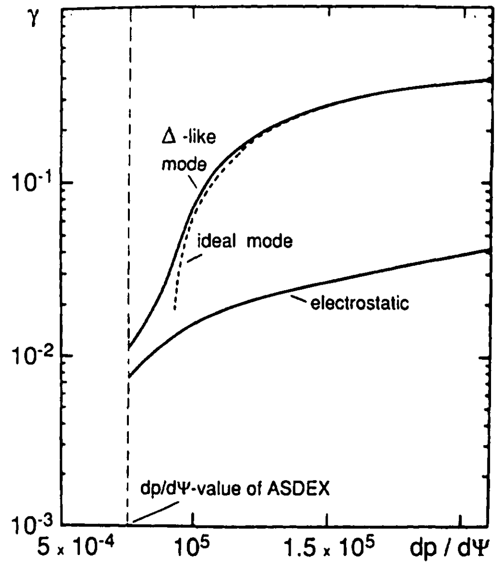

FIG. 99. Ideal and real resistive ballooning growth rates in ASDEX obtained by applying an increased pressure gradient in the plasma edge region.

To summarize, the increased energy losses at the beta limit are connected with resistive ballooning instabilities, but the anomalous losses observed far below the beta limit are caused by other instabilities.

8. COMPARISON OF H-MODE PROPERTIES ON ASDEX WITH THOSE FOR OTHER EXPERIMENTS

The H-mode has also been observed in divertor experiments on JET [8], DIII-D [6], PDX [5], PBX [100] and JFT-2M [7]. A very important point is that the divertor on JET, DIII-D and JFT-2M has an open, expanded boundary configuration and the plasma cross-sections are elliptic. These are the topological characteristics envisaged for reactor-grade tokamaks regarding power exhaust, ash removal and high current capability. The accessibility of the H-mode, even in a not fully optimized geometry, has been demonstrated on JET, which was originally not designed as a magnetic limiter configuration.

H-mode operation under limiter conditions has been demonstrated on JFT-2M [7], TFTR [101], DIII-D [102] and JIPP-T2 [103]. These studies clearly show that the high edge shear specific to the divertor configuration is not the determining factor for L–H transition and improved confinement. However, it is found that the improvement of confinement is poor for a circular limiter plasma. Only with an elliptic cross-section is the energy confinement time of limiter discharges clearly improved, as shown on JFT-2M and DIII-D. These experiments indicate that the magnetic configuration and the enhanced shear may, nevertheless, be of importance. On the other hand, results for limiter discharges in the H-mode also indicate the importance of recycling control for good confinement (recycling control is a necessity in other good confinement regimes, such as the supermode [104], the IOC regime [54] and the improved regime with counter-NI [105]).

The phenomenology of the H-mode development is the same in all cases [106]. With the exception of the occurrence of the Ohmic H-mode in DIII-D, a short L-phase succeeds the H-phase, and the transition is rapid and distinct. In the H-phase, both particle and energy confinement improve, leading to a rise in density and beta. The transition to the H-phase is clearly indicated by a sudden drop in the H_α radiation emitted from the high recycling zone (in the divertor chamber, around the X-point or in front of the limiter).

We now compare the H-mode results from ASDEX with those from DIII-D. (The plasma geometry parameters of DIII-D are: $R = 169$ cm, $a = 64$ cm and $\kappa \leq 2.0$.) In some aspects, the DIII-D results are complementary to those of ASDEX, for example regarding the discovery of the Ohmic H-mode [102] and of the H-mode initiated by ECRH [107] on DIII-D. From these results (together with the H-mode obtained with NI or ICRF heating) it is clear that the development of the H-mode is connected with the plasma properties and is rather independent of the characteristics of the heating technique.

8.1. Agreement between the observations on ASDEX and DIII-D

In the H-mode of DIII-D, energy confinement times of up to 160 ms have been obtained in pure D^+ plasmas ($I_p = 1$ MA, $P_{NI} \sim 5$ MW); in the L-mode, $\tau_E \sim 70$ ms. As in the regular H-mode of ASDEX with ELMs, no distinct scaling of τ_E with power (for $D^0 \rightarrow D^+$), $\bar{n}_e$ and B_t was observed on DIII-D; no power dependence was found in the range $3 \leq P_{NI} \leq 6$ MW. For the Ohmic H-mode discovered on DIII-D, however, a degradation of τ_E with heating power was also observed; τ_E increased linearly with I_p (for $q_{95} \geq 3$). The operational range for this H-mode is large, but a power threshold and a density threshold have to be exceeded. For $I_p = 2.1$ T, the critical heating power is 3 MW (on ASDEX 1.2 MW); the critical density is $\sim 2 \times 10^{13}$ cm^{-3}, which is similar to that of ASDEX single-null plasmas. As on ASDEX, the power threshold is larger in the double-null configuration than in the single-null configuration. It is also observed that the ion grad-B drift to the X-point reduces the power threshold (this important aspect has also been observed on JFT-2M and JET). The power threshold is increased by operating with hydrogen or helium plasmas instead of deuterium. Furthermore, on DIII-D the power threshold with counter-NI is 20% lower than that with co-NI.

Another interesting common observation is that the H-mode is quenched when the plasma current is ramped up (although it can be obtained at any constant current level). This observation is not yet understood.

The transition to the H-phase is frequently triggered by a sawtooth; after the L–H transition, steep pressure gradients develop at the edge. Although some uncertainty remains because the gradient length is comparable to the accuracy with which the separatrix location can be determined, it is concluded that the steep pressure gradient is inside the separatrix because of the development of an edge transport barrier. On DIII-D, furthermore, a decrease of the density fluctuation level inside the separatrix is observed (by microwave reflectometry). At the L–H transition, the SOL and also the power deposition profile at the target plates shrink. The power deposition profile is reduced and — as on ASDEX — the degree of power accountability is worse than under OH- and L-mode conditions. After the L–H transition, the plasma profiles broaden and the electron temperature develops an edge pedestal of approximately 300 eV.

On DIII-D it is found by transport analysis that not only does the confinement improve at the very edge but also the heat diffusivity (single-fluid treatment because of high density) in the zone $0.5 \leq \rho \leq 1$ decreases by a factor of three after the L–H transition and agrees approximately with the Ohmic diffusivity values.

ELMs are also observed on DIII-D in the H-phase. The power and particle losses are 10–20% of the particle and energy content — somewhat higher than on ASDEX. There is clear evidence on DIII-D that ELMs are pressure driven instabilities which occur when the edge pressure gradient reaches the limit of the first stability regime. Because of the circular topology of the ASDEX plasma, the critical pressure for ballooning instabilities may be lower on DIII-D, resulting in lower ELM amplitudes.

8.2. Disagreement between the observations on ASDEX and DIII-D

An important difference between ASDEX and DIII-D is the parameter dependence of the threshold power for the H-mode. On DIII-D, $P_{thr} = 0.6\,\bar{n}_e B_t$ (MW, 10^{13} cm^{-3}, T, $H^0 \rightarrow D^+$). On ASDEX, only a weak dependence on these parameters is observed. The density dependence may be the result of the sensitivity of the H-mode to recycling control (because the recycling flux increases with $\bar{n}_e$) and this dependence may be different in the expanded boundary configuration and in the closed divertor configuration.

A dependence of the threshold power on the toroidal magnetic field is also observed on JET. No reason for the different observations on ASDEX can be given. Configurational and machine-specific effects cannot be ruled out: On JFT-2M, the threshold power is found to depend on the plasma current, which is not seen on any other experiment.

Contrary to the observations on ASDEX, the development of an extremely broad density profile has been observed on DIII-D which can even become very hollow. The edge density rises strongly and the edge plasma remains collisional even in the H-phase. This difference does not seem to be of a fundamental nature. On ASDEX, the density profile shape is found to depend on the recycling and the wall conditions and becomes broader with a more open divertor structure and a higher recycling rate (see Section 4.2).

The differences in the impurity development during the H-phase may be a consequence of the different density profile shapes in the two devices. On ASDEX, the electron density profile is peaked and there is a strong increase of the central impurity radiation. On DIII-D, the impurities are concentrated in the edge region where the density profile peaks. Impurities seem to be carried to the radial zone of maximal density by neoclassical effects. Furthermore, central impurity accumulation may be prevented by sawteeth, which are generally present in the centre of DIII-D H-mode plasmas but are absent on ASDEX. On DIII-D, the magnetic turbulence as measured by probes outside the plasma clearly decreases after the L–H transition. This decrease is generally used to signal the transition. A rather sophisticated variation of the magnetic fluctuation level at the L–H transition has been seen on ASDEX; the signal can decrease but also increase, depending on the frequency range, the field component and the behaviour of the coherent MHD phenomena.

9. DIFFERENT THEORETICAL MODELS FOR THE H-MODE

In this section we discuss some of the theoretical models put forward to explain the L–H transition and the good confinement in the H-mode, and we compare the predictions with experimental data from ASDEX. The comparison is mainly qualitative; this is partly due to the nature of the models, but it also reflects the difficulties in carrying out edge measurements of sufficiently high spatial resolution to match the steep gradients forming in the H-mode.

The transition to the H-mode clearly begins at the plasma periphery, where the most pronounced parameter changes occur. The first task of relevant theories is therefore to explain how the conditions for the H-mode can lead to changes in the linear or non-linear stability behaviour of transport inducing modes in the boundary zone. These theories ought to provide explanations for: (1) the abruptness of the transition, (2) the possibility of two different equilibrium solutions for the same values of the externally controllable parameters, at least over a limited parameter range, and (3) the hysteresis observed in the comparison of the L–H transition with the H–L transition.

Historically, in all these models the poloidal divertor geometry was considered first; often, however, they do not strictly depend on this geometry. A class of these models starts from the high-q, high-shear region in the vicinity of the separatrix, which also exists — to a smaller extent — at the boundary of non-circular limiter tokamaks. Other models involve particle loss orbits or the predominant direction of the poloidal heat flux in the SOL and would also hold if the first plasma-wall contact were with an appropriately located limiter. For a quantitative comparison, we also have to take into account that the shear conditions of the actual ASDEX geometry significantly differs from the simple model equilibria used in some of these calculations and also from the equilibria in 'open divertor configurations'. ASDEX was designed so that deviations from a circular cross-section geometry are localized as much as possible at the plasma boundary; therefore, ASDEX has a much smaller spatial region where the flux surface averaged shear and the safety factor q_ψ are visibly influenced by the presence of the stagnation points.

In addition to the formation of a density and temperature pedestal, the H-mode on ASDEX gives rise to a reduction of the electron diffusivity in the plasma interior. This has been demonstrated both by TRANSP-type analyses and by simulations in which explicit switching to different diffusivity was used to model the L–H transition in the plasma interior. From the standpoint of a purely local transport theory, however, it should be possible to explain this reduction of the electron diffusivity as a consequence of the dependence of the diffusivities on the plasma parameters. Some such models have indeed been proposed, albeit generally only in a qualitative form.

9.1. H-regime theories involving SOL physics

The behaviour of the SOL of divertor tokamaks is distinctly different from that of conventional limiter devices. Thus, for given energy and particle flow, multiple solutions may exist for the density and temperature distributions along the field lines intersecting the target plates. Thus, it would seem to be promising to study the SOL physics in order to find the origin of the L/H-mode bifurcation. It is not possible, however, that the steep radial gradients in the edge region are caused only by a modification of the transport along the field lines, since even complete suppression of parallel losses will only produce conditions equivalent to those prevailing anyway on closed flux surfaces.

The first, and most detailed, model was suggested by Ohkawa et al. [108]. It consists of two elements. Radial transport in the SOL is assumed to be reduced (below the transport across closed field lines) by the electrical contact of the open field lines with the target plates and the consequent suppression of weakly unstable electrostatic and electromagnetic modes. On the other hand, energy losses along the field lines can be suppressed by the formation of a potential distribution with a local minimum, giving rise to a thermal barrier similar to the one proposed for mirror machines. For the formation of a potential minimum, the plasma density has to increase strongly towards the target plate. The L–H transition would thus coincide with a strong increase of the ionization rate in the vicinity of the target plate. According to this model, the steep gradient zone would lie outside the separatrix, and the midplane electron temperature in the SOL would be increased during the H-phase.

In experiments, however, a drop of the H_α radiation in the divertor chamber is clearly observed. The validity of a theoretical model also depends crucially upon whether the observed steep gradient zone lies inside or outside the separatrix. The required accuracy of the experimental results can be questioned because the location of the separatrix in the plasma midplane is deduced from equilibrium calculations, which gives the separatrix position in the midplane to no better than ±1 cm (corresponding to one density e-folding length λ_n in the SOL). Nevertheless, the experimental results from ASDEX indicate that the high temperature zone and the steep gradients are located inside the separatrix (see Section 2.5); this also leads to more consistency between the various SOL and divertor plasma measurements. Other experiments in the H-mode also confirm the location of the steep gradient zone inside the separatrix [5, 109].

Even a simple gas dynamic model combined with Spitzer heat conductivity is capable, however, of yielding two solution branches for the SOL parameters [110]. The high density branch [111] as well as the low density branch [112] have been identified as the regions corresponding to the H-regime. The predominant experimental evidence, however, is that a zone of high radial thermal resistance is located inside the separatrix. An outstanding feature of the L–H transition in the SOL as a consequence of this edge barrier is the sudden reduction of the power flow into the SOL, with a consequent decrease of the plasma parameters in the SOL and in the divertor region.

9.2. Models of high shear zone effects

In a poloidal divertor configuration, the safety factor q_ψ diverges logarithmically, and the flux surface averaged shear diverges inversely linearly, with the distance from the separatrix. This is expected to have consequences for the linear stability and the saturation amplitude of ideal and resistive MHD instabilities.

In particular, the stability of ideal MHD ballooning modes in the vicinity of a separatrix has been thoroughly investigated for a simplified model geometry [113, 114]. In this model, the parameters determining the permissible pressure gradients are the proximity to the separatrix, the location of the stagnation point in the poloidal plane, and the normalized current density Λ, parameterized in the form $\Lambda = rV_l/2\pi \, RB_p \, \eta$ (η is the electrical resistivity), in the separatrix region. For X-points located more on the high field side of the separatrix centre (as is the case for ASDEX, PDX, Doublet III, JET, JFT-2M), the limiting pressure gradient of the first stable region shows relatively little dependence on the current density and the separatrix

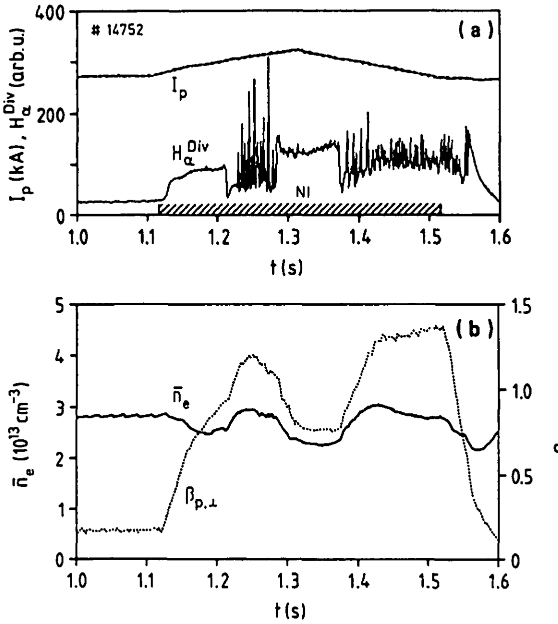

FIG. 100. (a) Forced L–H and H–L transitions by current ramp-up and decay. The H_α radiation in the divertor chamber indicates the regime transitions.
(b) The density and $\beta_{p\perp}$ are plotted for reference.

distance. The lower limit of the second stable regime, on the other hand, strongly decreases with increasing current density and decreasing separatrix distance, ultimately leading to a coalescence of this limit with the first stable regime for sufficiently large values of Λ. For stagnation points situated closer to the low field side (as in the old JT-60 configuration), on the other hand, even interchange modes can become unstable, and the first stability limit of ballooning modes becomes sensitive to the current density near the separatrix. In particular, this stability limit passes through zero as a function of Λ before reaching the point of possible coalescence with the second stable regime.

On the basis of these theoretical results, Bishop [115] developed a scenario for an L–H transition in which the pressure gradient of the one solution branch, corresponding to a low edge temperature (and hence low edge current density), is limited to the first stable regime, and the second branch, corresponding to a high edge temperature, passes through the coalescence point into a pressure gradient regime that is not limited by ballooning modes.

For a complete explanation of the L–H transition with this model, the pre-transition L-mode phase would have to be close to the ballooning limit. The measured electron pressure gradient at the edge (normalized in the form of $\alpha = -2\mu_0$ Rq $2p'/B_t^2$) is $\alpha = 0.07$ in the L-mode and $\alpha = 0.35$ in the H-mode. The pressure gradient at the edge may be close to the ideal ballooning mode stability limit in the H-mode, but it is far from this limit in the preceding L-mode. The required edge current density Λ would have to be above 0.7 near the X-point to reach the second stability regime. For $Z_{eff} = 1.8$, an edge electron temperature of 500 eV would be required (see for comparison Fig. 27), which is close to the upper limit of the experimental error bars for H-regime conditions (an additional contribution to it could, however, come from the bootstrap current).

In a dynamic model of the L–H transition, the high edge current density would, however, have to be established before the L–H transition, which is not supported by experimental measurements. The MHD behaviour, as described in Section 2.3, indicates a broadening of the current density profile, but only after the L–H transition when the m = 1 activity slowly disappears (see Fig. 13). It is also not clear whether the change of the current density profile can happen fast enough in the case of a sawtooth-initiated L–H transition.

Specific experiments have been performed on ASDEX to study the effect of current profile changes on the H-mode. Figure 100 shows the plasma current, which was ramped up and down in the beam phase, the line averaged density, and the H_α radiation in the divertor chamber used to monitor the confinement regimes. When current is added in the edge region, the H-mode is suddenly quenched; when current is removed from the edge region, the H-mode reappears. Under steady state conditions the H-mode can be maintained at a current level well above the critical one, indicating that the results in Fig. 100 are not due to a current limit for the development of the H-mode. Thus, the favourable effect of the edge current density on the development of the H-mode is not confirmed, although the interpretation of the dynamic experiments as presented in Fig. 100 is not unambiguous.

Even if the model of Ref. [113] cannot quantitatively explain the L–H transition on ASDEX, it still contains some valuable elements. For example, the observed ballooning stability of separatrix bound equilibria with the X-point in the bad curvature (low field) region could provide an explanation for the difficulties experienced on JT-60 in connection with the H-regime, and better agreement between theoretical studies and experiments might be obtained if resistive ballooning modes were taken into consideration. Also, the increasing confidence in the existence of the bootstrap current may bring a substantial new element into this model, since in this case the high edge current density (which is a prerequisite for high pressure gradients in this model) can be due not only to the increased electron temperature but also to the increased pressure gradient itself.

The high edge temperatures and the bootstrap effects in the H-regime give rise to uncommonly high edge current densities and hence steep current density gradients. These are conditions known to drive, in conventional geometries, tearing or kink modes with resonant surfaces in or just beyond the steep gradient zone (see also Section 2.3). It has been shown in an analysis by Hahm and Diamond [116] that, at least for a linear model of highly localized, high-m, high-n modes, the consequences will be different in a scenario in which the shear introduced by the geometry of the flux surfaces strongly dominates that originating from the current density distribution. In this case, the modes are found to be strongly stabilized — a point which we shall further discuss in connection with models for confinement changes in the plasma interior.

The authors of Ref. [116] also studied the possible impact of the separatrix geometry on resistive fluid turbulence, which is possibly the cause of Ohmic and L-mode transport in the outer plasma zones. They specifically considered incompressible resistive ballooning modes and impurity gradient driven rippling modes as the reasons for anomalous electron heat conduction and particle transport, respectively. In both cases the main effect of the separatrix geometry is a reduction of the characteristic radial scale length of the resulting fluid turbulence due to the high shear and consequently a reduction of the contributions to the electron heat diffusivity, the diffusion coefficient and the runaway loss rate. It has been shown recently by Burrell [117] that the specific stabilization mechanism of resistive ballooning modes (the increase of the diamagnetic drift frequency) suggested by the authors of Ref. [116] cannot be responsible for the L–H transition, since the associated diffusivity would actually increase during the formation of the temperature and density pedestal. Since, however, expressions suggested by Callen et al. [118] for resistive ballooning mode driven turbulence yield reasonable agreement with the magnitude and profile shape of the electron heat diffusivity in the outer plasma zones of L-discharges, the search for other stabilizing mechanisms should be continued.

9.3. Effects of the discontinuity between open and closed flux surfaces on plasma transport

In the proximity of the plasma boundary, the radial particle and energy transport can be modified through losses of charged particles to the target plates. Models based on this effect have been stimulated by the discovery of the H-regime and they frequently refer specifically to the axisymmetric divertor geometry. However, for the flux surface structures used in these models to be applicable, it is only necessary that the contact between the plasma and the target plates be axisymmetric, with the contact located on the top or the bottom, or at the high field side of the plasma boundary. These theories therefore are not invalidated by the discovery of the limiter H-mode.

The first theory of this type, and the one that has had the best experimental verification [119], is the work by Hinton [120], who showed a strong dependence of the Pfirsch–Schlüter ion energy transport across the separatrix on the location of the X-point. The sink constituted by the target plates induces an additional heat flow along field lines, adding to or subtracting from the parallel Pfirsch–Schlüter flow and therefore also increasing or decreasing the radial heat flux for a given radial ion temperature gradient. For a given heat flux through the separatrix, parallel fluxes give rise to flat ion temperature gradients, while anti-parallel fluxes cause steep gradients. Since the direction of the parallel Pfirsch–Schlüter heat currents depends on the ion grad-B drift, steeper gradients will develop if the latter is in the direction to the X-point. In the symmetric DN configuration with two X-points, these geometric effects should cancel each other. At high heating power these aspects also play no role because the heat transport under collisionless conditions is not affected by the X-point topology.

Ion heat conduction is not considered to be the dominating energy transport process across the separatrix, but it will contribute to the power balance at the edge and its strength may be decisive for the attainment of the high edge temperature values associated with the H-regime. In a more recent work, Hinton and Staebler [121] showed the existence of a similar effect on particle transport, which could be even more significant, because convective energy losses may indeed be a dominating term in the power balance.

Unlike the stability conditions of ideal ballooning modes, which also introduce geometric constraints, the neoclassical transport effects described above predict the kind of up–down asymmetries for which there is strong experimental evidence.

In experiments, the H-mode can be obtained both in the SN and the DN configurations. The SN configuration is achieved by vertically displacing the toroidal plasma column a few centimetres, utilizing a radial magnetic field. The SN topology has major advantages, such as lower power and density thresholds (see

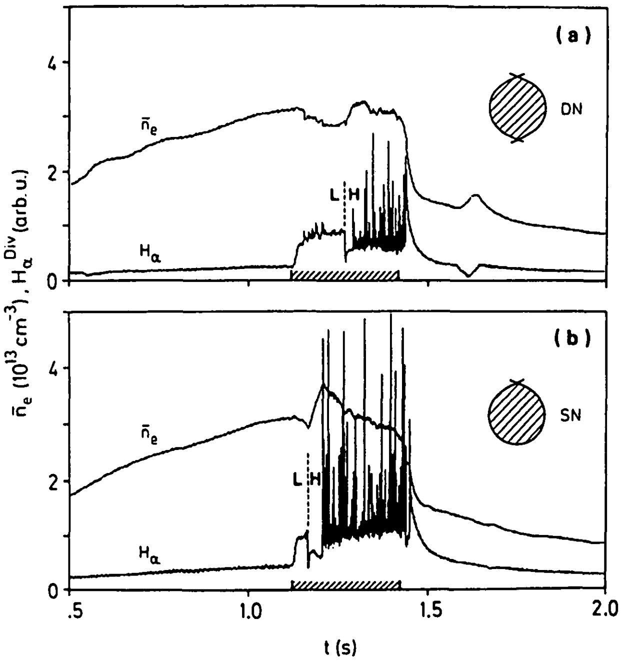

FIG. 101. L–H transitions of two consecutive shots (Nos 15564 and 15565), for a DN discharge (a) and an SN discharge (b). The vertical displacement of the SN discharge is 1 cm. I_p = 0.31 MA, B_t = 2.2 T, P_{NI} = 3.5 MW.

Section 4); in the SN configuration, with hydrogen injection into a hydrogen plasma and $P_{NI} \geq 2.5$ MW, the H-phase can be achieved by refuelling into the main plasma vessel (in the DN topology the refuelling must be done in the dome). Furthermore, with the SN configuration the H-mode can be achieved even in a 'dirty' plasma (for example when operation is resumed after the vessel has been vented), in which case the development of the edge electron temperature is impeded by impurity radiation and the available heating power is insufficient to produce the H-mode in the DN geometry.

In the SN configuration, the L-phase preceding the L–H transition is always observed to be shorter than the DN configuration, at the same plasma and beam parameters. Two subsequent discharges — one in the DN configuration and the other in the SN configuration — are compared in Fig. 101. The vertical displacement is 1 cm in the case shown in Fig. 101(b) and corresponds to a typical (density or temperature) density e-folding length in the SOL. Plotted are the line averaged density and the H_α/D_α radiation in the divertor chamber. The drop in the H_α/D_α radiation and the simultaneous rise in density (until ELMs set in) mark the transition to the H-phase. In the DN topology the pre-transition L-phase is 150 ms and in the SN topology it is only 45 ms.

The most important aspect of Hinton's theory is the expected impact of the ion grad-B drift direction on the L–H transition, which is indeed observed experimentally [119]. Figure 102 shows an operational diagram of the H-mode regarding the power and the vertical plasma position (which determine the plasma configuration). Centred (z = 0) plasmas are DN discharges, while plasmas shifted upward (downward) are upper (lower) SN discharges (open circles indicate L-discharges and arrows indicate the ion grad-B drift direction). As predicted in Ref. [120], at high beam power the H-regime can be obtained irrespective of the symmetry of the stagnation points or the direction of the ion grad-B drift, even when the plasma edge becomes collisionless. Figure 102 gives the same information as Fig. 60(a), illustrating that in the DN configuration more power than in the SN topology (e.g. the cases at z = 4 cm) is required to produce the H-mode, provided the ion grad-B drift direction is correct. For positive vertical displacements, when the ion grad-B drift direction is towards the stagnation point, H-discharges are obtained, while in the lower SN topology, with the ion grad-B drift direction away from the stagnation point, only L-discharges are obtained at medium heating power levels.

When the toroidal field is reversed (with the direction of the plasma current being the same to maintain the co-injection geometry), plasmas in the upper SN configuration are L-discharges, while plasmas in the lower

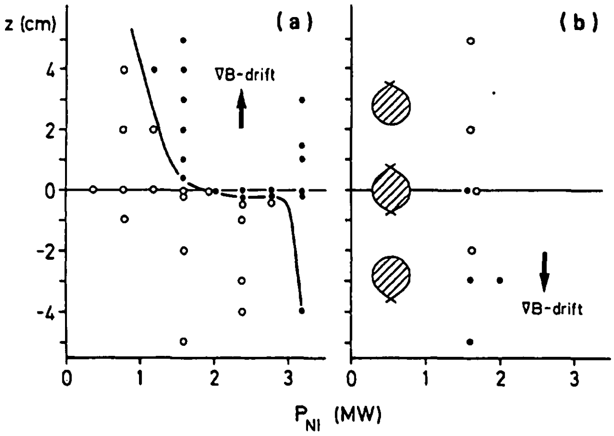

FIG. 102. Operational diagram for L- and H-discharges (H^0 injection into D^+ plasmas). z is the vertical plasma position; z > 0 in the upper SN configuration, z = 0 in the DN configuration and z < 0 in the lower SN configuration. P_{NI} is the beam power injected into the vessel. The arrows indicate the ion grad-B drift direction. The curve in (a) denotes the operation boundary between L- and H-discharges and (b) indicates the plasma configuration. The solid points are for H-discharges and the circles for L-discharges.

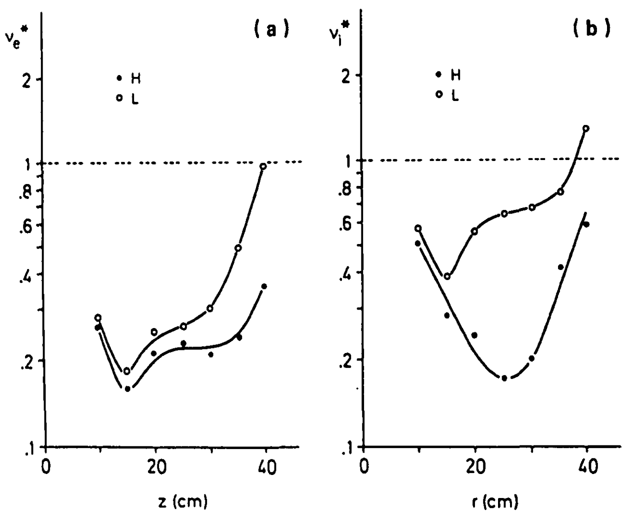

FIG. 103. Electron and ion collisionality parameters deduced from the measured profiles. The transition from the plateau to the collisionless regime is indicated; P_{NI} = 3.3-3.5 MW; B_t = 2.2 T; (a) I_p = 0.31 MA; (b) I_p = 0.38 MA.

SN configuration — with the ion grad-B drift towards the (lower) stagnation point — mostly turn out to be H-discharges. (Only a few discharges with a reversed field have been carried out, since the reversed magnetic forces pose an additional risk for the machine.)

As mentioned above, besides ion heat conduction also convection and charge exchange cause losses in the boundary zone. Only if the edge neutral density is kept low — which is probably the case in the divertor configuration where recycling occurs predominantly within the divertor chamber — can neoclassical or only moderately increased ion heat conduction be prevalent in the region adjacent to the separatrix.

The detrimental role of increased recycling and gas puffing has indeed been observed experimentally. In both PDX [5] and ASDEX it is found that gas fuelling from the divertor dome instead of from the main plasma vessel facilitates the L-H transition. Excessive gas puffing could quench the H-phase in PDX, which would lead to low confinement.

In ASDEX the H-mode is obtained with hydrogen neutral injection into hydrogen plasmas if the source of the external gas flux that is required to maintain constant density is moved from the main plasma into the divertor chamber. Results obtained with various divertor geometries, as summarized in Section 4.2, further revealed that at low power with a closed divertor configuration the H-phase can only be obtained when the molecular hydrogen backflow from the divertor into the main plasma is reduced. The detrimental effect of the proximity of a material limiter is discussed in Section 6.1.2. The transition to the H-phase is prevented by a poloidal limiter placed at a distance corresponding to about two SOL e-folding lengths. At this distance, impurity erosion may still be low, while the local neutral density at the limiter is already increased (in the Ohmic phase by a factor of approximately five). As in the case of the electron temperature, the ion temperature increases after the L-H transition (see Fig. 7); at r = 35 cm, T_i rises further, from 0.7 keV in the L-phase to 1 keV in H-phase. A steep T_i gradient develops at the edge. Figure 103 shows the ion and the electron collisionality parameters ν_i^* and ν_e^* deduced from the electron and ion temperature profiles, measured just before the L-H transition and 100 ms after it. The results are obtained in the closed divertor configuration DV-I. The ion collisionality parameter at the plasma edge is slightly above unity in the L-phase and clearly drops below unity after the L-H transition. The electron collisionality parameter at the plasma edge is about unity in the L-phase and about 0.4 in the H-phase.

These measurements indicate that the electrons and ions are nearly collisionless even at the plasma edge. In the pre-transition L-phase the collisionality parameters are close to unity. In the various divertor configurations studied (with different relative changes of $n_e(a)$ and $T_e(a)$ after the L-H transition), $\nu_e^*(a)$ is >1 in all cases in the L-phase. At r = 0.95a, ν_e^* is <1 in all cases. In the closed divertor configuration, ν_e^* drops to below 0.5 after the L-H transition even at the plasma edge. In the open configuration, $\nu_e^*(a)$ remains between 1 and 2 in the H-phase, while $\nu_e^*(0.95a)$ is about 0.5. Neither the rise of q at the plasma edge in the separatrix configuration nor the very likely increase of Z_{eff} near the plasma edge have been considered in the calculation of the collisionality. The quoted ν_e^* values are therefore lower boundaries. Despite these uncertainties, it is possible that the collisionality regime at the plasma edge changes at the L-H transition.

Many features of the L-H transition are in qualitative agreement with Hinton's theoretical model: for the L-H transition, low recycling conditions are required and — as long as the plasma periphery is still collisional (at low beam power) — an asymmetric topology of the SN configuration. In an SN discharge, the H-mode develops at low heating power, shortly after the NI pulse is switched on, in hydrogen plasmas, and even under 'dirty' operational conditions, if the direction of the ion grad-B drift is towards the stagnation point. If the L-H transition occurs at a critical gradient (which also requires a critical ion temperature gradient), Hinton's model predicts the existence of a power threshold.

Particle transport across magnetic flux surfaces is linked with the momentum balance of the different species and is intrinsically ambipolar in the inner regions of axisymmetric devices. This is not true in the near-boundary zone, where electrons and ions can exchange momentum not only with each other but also with neutrals and with waves escaping from the plasma or with material walls (for particles on 'loss orbits'). In this situation, quasi-neutrality is enforced by the appearance of a radial electric field which modifies the transport of one or both species so that the net charge loss out of the plasma is stopped. Thus, there is some analogy to collision induced transport in the interior of stellarators, in which case there are sometimes two solution branches for particle transport which differ in the sign of the radial electric field.

The possible influence of electric fields on the L–H transition was first pointed out in Ref. [122], where a model of particle losses for the boundary zone is presented. In this model it is assumed that the ions are lost through neoclassical orbit effects and that the electrons are lost when they stream along braided field lines. Both forms of transport depend on the radial electric field; the quasi-neutrality condition of radial flow is expressed by a relation between the gradient parameter λ (weighted sum of logarithmic density and temperature gradients) and the particle flux Γ_p. In general, the relation has three roots for $\Gamma_p(\lambda)$, but, at low values of λ, only the high flux branch exists (with Γ monotonically increasing with λ) and, at high values of λ, only the low flux branch exists. For the L–H transition scenario it is assumed that during the pre-transition L-phase the gradients increase until the high flux branch of the solution is no longer valid and a sudden transition to the low flux branch takes place. The S-shape of the $\Gamma_p(\lambda)$ relation also leads to a hysteresis effect in the transition, with the H–L transition occurring at lower values of λ compared with the L–H transition.

At least in a qualitative sense, this L–H transition model reproduces many experimental observations very well. The transition in the boundary region is sudden and exhibits hysteresis character. Its primary effect is a drop in the charged particle flux crossing the separatrix. Before the transition, sufficiently steep gradients are required (these will become even steeper after the transition) and thus the transition is certainly sensitive to the magnitude of additional power losses, such as charge exchange or ion heat conduction losses, as discussed by Hinton. As energy transport mechanism, the model considers only convection, which, however, may indeed be dominant in this zone during the L-phase. After the L–H transition, because of the reduction of the particle flux and, in particular, the form of its further dependence on λ (Γ_p decreases with increasing λ) the plasma cannot regain thermal equilibrium only through convection effects. In fact, we observe a reduction of the power flux into the separatrix and a loss of power accountability, indicating that in the edge region the parameters indeed reach values at which new loss channels may open up (one of them being ELMs).

The critical element of the model presented in Ref. [122] is that it identifies (as for stellarators) the good confinement branch as the branch having positive radial electric fields (E_r). However, limiter bias experiments on ISX-B (the relevance of which for the L–H transition can, of course, be questioned) have shown that particle confinement is improved by a negative bias. Recent measurements of the poloidal rotation of the plasma in the separatrix region of DIII-D [123] also give results which are in contrast to those predicted by the model of Ref. [122], since they show that the H-phase is associated with more negative E_r values. In this model, no changes of the turbulent fluctuation level are required for better confinement, contrary to experimental observations (see Section 6.3). On ASDEX, no measurements of the E_r field at the plasma edge have yet been made. The only indication of a change of E_r comes from the asymmetric broadening of the scattering spectra, as described in Section 6.3.

A different approach to incorporating E_r fields into an L–H transition model was made by Shaing et al. [124], who used a neoclassical model of turbulence driven transport. In this case, the sensitivity of the results to E_r arises from the shear in the $\vec{E} \times \vec{B}$ induced toroidal velocity, which can affect the frequency spectrum of the transport producing turbulence. In particular, for the resistivity gradient driven turbulence it is explicitly shown that a negative E_r branch would correspond to a narrower spectrum and a reduced saturation level. The resulting turbulence induced ion and electron fluxes are intrinsically ambipolar, so that they, by themselves, do not determine the value of E_r. In the region near the edge, E_r is determined by the necessity of balancing the non-ambipolar ion losses, induced by momentum exchange with neutrals, and the E_r field modified orbit losses. For low neutral density and an ion collisionality parameter $\nu_i^* < 1$, this leads to a more negative E_r field which reduces the amount of ambipolar losses. With both $\nu_i^* \gg 1$ and $\nu_i^* \ll 1$, E_r becomes less negative. Shaing et al. [124] identify the two E_r regimes with the H-mode and the L-mode, respectively. The observed improvement in confinement would then be primarily due to the change in the anomalous transport contributions, which are necessarily ambipolar but depend on the prevailing E_r field. This theoretical model is in line with the existing evidence of the E_r field behaviour in other devices; another point in favour of this model is that the L–H transition indeed reduces the type of anomalous losses that are probably responsible for the transport in the L-phase. So far, however, no catastrophe-type transition scenario has been demonstrated with this model. On the basis of our experimental evidence, we consider such a proof to be essential in any theory on the L–H transition in the plasma periphery.

9.4. H-mode transport in the plasma interior

Transport analysis indicates that the overall improvement of the confinement in the H-mode probably takes place in two steps: a sudden increase correlated with the development of an edge barrier and then a gradual improvement which is determined by diffusive processes that may lead to profile changes in the plasma interior. The processes can perhaps be explained in terms of a continuous parameter dependence of the diffusivities throughout the OH-, L- and H-phases. Since there is no first-principle transport model which correctly reproduces both the global parameter scaling and the temperature profiles, only qualitative investigations have been made so far.

The general trends of confinement at the L–H transition in the inner plasma zones are, however, not inconsistent with the predictions of the standard model of strong electrostatic turbulence driven by drift waves [125, 126] and by η_i modes [127]. As discussed in Section 3.3, the ion heat transport in all confinement regimes of ASDEX can be well described by a combination of neoclassical contributions and η_i mode driven contributions to the heat diffusivity. A conspicuous feature of the H-regime is the flattening of the density profiles in the plasma interior, where, actually, no improvement of the ion energy confinement has been observed. An increase of η_i would actually lead to an enhancement of this transport channel, which is, however, limited by the approach of $L_n = (d \log n/dr)^{-1}$ to the major plasma radius R_0, according to recent theories [128, 129]. On the other hand, an increase of L_n would reduce the contributions of dissipative and collisionless trapped electron modes to the electron heat transport, in agreement with experimental observations. While the agreement between ion heat transport and predictions for the η_i mode is satisfactory even quantitatively, the above statements concerning the electron heat diffusivity have been verified only in a qualitative sense. The most serious objection to this electrostatic turbulence model concerns its implied unfavourable isotope dependence, which is in contrast to the observed trend of χ_e.

In the H-mode, the steep gradients of the pressure, particle density and current density are moved to the region directly at the edge; thereby the free energy in the bulk plasma is reduced, which may lead to an improvement of the transport conditions there. The specific edge structure in the H-mode may thus permit the formation of a type of plasma profiles with better confinement aspects. One profile which will clearly show a significant change after the L–H transition is that of the current density. The most direct contribution to this change comes from the associated high edge temperatures: the electrical conductivity in the plasma periphery in the H-mode is about the same as it is in the plasma centre during the OH-phase. Added to this should be the bootstrap current that is associated with the steep pressure gradients in this zone (possibly modified by the presence of the plasma boundary; see Ref. [130]). The calculations of Hahm and Diamond, discussed in Section 9.2, indicate that the plasma should indeed be capable of accommodating a higher current density gradient in the high shear region, so that a displacement of the current to the edge region has a generally beneficial effect upon the stability to current driven modes. Improved MHD stability in the bulk plasma is indeed observed in the H-mode because the $m = 1$ mode and the sawteeth disappear without being replaced by $m = 2$ mode activity. What is unclear is how the improved stability to macroscopic modes is connected with the microscopic turbulence. Many studies of this subject have been published. This problem is also discussed in conjunction with the degradation of confinement in the L-mode and the observed resistance of the electron temperature profile to any changes by auxiliary heating [130]. A controversial point in this respect is the problem of the associated time-scales, because the penetration of current density perturbations should proceed on the resistive skin time, whereas the observed adjustments of the electron heat diffusivity seem to proceed on a much shorter time-scale.

In general, resistive-type fluid turbulence, as considered in Ref. [116], should be reduced by giving the plasma profile a temperature pedestal. The confinement could thus improve, at least in the outer zones of the bulk plasma (corresponding approximately to the region $q > 2$) where this type of transport has sometimes been postulated to dominate. A further mechanism by which resistive fluid turbulence (but possibly also other modes) might be reduced was suggested by Shaing et al. [124] in the context of his neoclassical model of turbulence driven transport (see Section 9.3), namely that the radial field changes associated with the L–H transition propagate inward owing to viscous damping of the resulting velocity shear in the corresponding flow.

Two attemps made to test some of these ideas by simulation calculations have been reported in the literature. One investigation [111] started from semi-empirical expressions that were, however, chosen to reflect the basic dependences expected from different types of turbulence in different plasma parameter regimes. The calculations were carried out in an attempt to obtain a quantitative fit of discharges on PDX and on ASDEX. By assuming an external trigger for the H-mode (argued to correspond to a sudden plugging of the divertor and acting through a rise in the respective edge densities), it was indeed possible to follow in time a complete experimental discharge scenario with a fair fit to the profiles and the average plasma parameters. The main effect of the L–H transition on the interior plasma could be reproduced by applying a transport that had a favourable density and temperature dependence and which was introduced to simulate the Ohmic confinement behaviour over the whole plasma cross-section. With additional heating, the Ohmic transport characteristics are assumed to dominate the outer zones.

Similar results were obtained in calculations of Sheffield [131]; these were made without reference to specific discharges, but took into account in a quantitative way the best present knowledge of local transport coefficients. From these studies it follows that modes of the resistive fluid turbulence type may account for the improvement in transport beyond the immediate edge zone after an L–H transition.

10. SUMMARY

In ASDEX, the H-mode develops during the auxiliary heating pulse after a preceding L-phase. At the L–H transition, both the particle content and the energy content rise; the divertor H_α radiation decreases within 1–2 ms, indicating an improvement of the confinement. During the H-phase, the plasma profiles broaden and steep pressure gradients develop at the edge. A new instability develops in the H-phase which is dubbed edge localized mode (ELM) because it affects the plasma periphery; it leads repeatedly to particle and energy losses. ELMs can be suppressed by moving the plasma closer to the outer wall. In this way, a quiescent H-mode (H^*-mode) is achieved, which has even better confinement properties than the H-mode with ELMs but which is very susceptible to impurity accumulation. After termination of the auxiliary heating pulse, the plasma remains in the H-phase for a short time (~30 ms); then it returns to the L-mode and gradually (within ~100 ms) again to Ohmic conditions.

The neutral heating efficiencies for both electrons and ions are better in the H-phase. In the case of thermal neutrons the fluxes are higher by a factor of three to four in the H-phase. Bootstrap and beam driven currents amount to nearly 50% of the total current.

Typically, NI heating is applied to sawtoothing OH target plasmas. In this case the sawtooth period increases and the duration of the $m = 1/n = 1$ precursor is prolonged. If L–H transitions are triggered by sawteeth, their period increases further. During the H-phase the sawteeth often disappear. At higher power (~1.5–2 MW), after the first sawtooth crash, the $m = 1$ mode remains at a quasi-stationary level without giving rise to sawtooth relaxation processes. If the L–H transition occurs during such a phase, the $m = 1$ amplitude is drastically reduced, but then it may again appear in fishbone-like bursts. In all scenarios the $m = 1$ mode provokes an $m \geq 4/n = 1$ satellite Mirnov oscillation (of the same frequency).

During the L-phase, also an $m \geq 3/n = 1$ mode is often observed. It propagates in the opposite direction compared with the $m = 1$ mode and at a lower angular velocity (lower frequency). The $m \geq 3/n = 1$ mode is located inside and near the separatrix and vanishes after the L–H transition within a few milliseconds.

The ELMs are a new MHD phenomenon of a disruption type; so far, they have been observed only in H-type plasmas. The most prominent manifestations of ELMs are the sudden change of the equilibrium position due to the loss of energy and a spike in the H_α emission from the divertor chamber, indicating increased power loss. During ELMs, the edge localized $m \geq 3$ mode reappears; it does not, however, have the character of a precursor.

The impurity development in the H-phase is determined by reduced plasma-wall interaction, improved particle confinement and, possibly, ELMs which represent an additional loss mechanism. When ELMs are present, quasi-steady state conditions regarding the plasma particle and energy content and impurity concentration can be established in the H-phase. Without ELMs, no steady state develops and in this case the

H-phase is already terminated during the beam phase by a transition to the L-phase. Accumulation of high-Z impurities can be described on the basis of classical impurity accumulation theory.

Various edge and divertor diagnostics are available on ASDEX to analyse the plasma parameters before and during the H-mode.

The transition from Ohmic heating to neutral injection generally leads to an L-mode which at the edge is characterized by a significant increase of the radial e-folding lengths in the SOL, an increase of the power and particle fluxes into the SOL and the divertor and, hence, a substantially intensified divertor recycling and power load. These changes are consistent with standard models of the SOL and the divertor when the increased fluxes are properly taken into account and when the values of the radial anomalous transport coefficients are taken to be twice as high as before, which is qualitatively in keeping with the worsening of the bulk confinement.

At the L–H transition the midplane edge gradients steepen significantly, causing a reduction of the radial decay lengths by a factor of more than two. The H_α signals drop everywhere, indicating a global reduction of hydrogen recycling. In the divertor, the recycling and power load are strongly reduced to roughly Ohmic values; the plasma profiles in the divertor chamber are narrower, in accordance with the reduced SOL width of the main plasma. Obviously, the power and particle inputs into the SOL and the divertor are decreased by a significant factor and the edge cross-diffusion coefficients are reduced to a fraction of the Ohmic value in the quiescent H-phase. Because of the steep gradients and the narrow profiles, the error in the determination of the separatrix position in the midplane and divertor (of the order of ± 1 cm), which is already a problem in the OH- and L-modes, becomes severe in the H-mode since the SOL width is of the same order. In the divertor, the profile maxima sometimes seem to move to the side of the separatrix where the field lines are not connected with the main plasma vessel — in contradiction to standard edge models. Furthermore, in the H-mode the position of the thermal barrier relative to the separatrix has to be considered. The following points seem to be relevant in this context: An independent determination of the position of the separatrix in the divertor which relies on the observed very narrow negative dip (caused by fast electrons) in the floating potential always gives a separatrix position that is approximately the expected one and that is sometimes in contradiction to the position determined magnetically. In the midplane, an independent measurement of the separatrix position on the basis of the soft X-ray emission from a radially moving target, again relying on fast electron dynamics, gives a radial position of the separatrix that is at the end of the error bars from the magnetic determination. In addition, the assumption of approximate pressure constancy along field lines between the midplane and the divertor (which may be questioned for the H-mode but is probably correct for the OH- and L-modes) also requires that the true separatrix position be outside that calculated from magnetic signals for all three phases. This is true without exception in all cases that have been studied in detail.

It is therefore concluded that during the H-mode the edge region is well described by the standard SOL theory if significant reductions of the anomalous radial transport and of the instantaneous power and particle fluxes across the separatrix are taken into account. No specific thermal barrier along open field lines (apart from a weak, standard flux limit) is required. Thus, it should be noted that the region of strongly increased 'edge' electron temperature is clearly inside the correct separatrix, in accordance with a perpendicular thermal barrier in the adjacent high shear region, while the separatrix temperature itself remains at moderate values. The quiescent H-mode is frequently interrupted by sudden increases of the energy and power flux into the SOL and the divertor that are produced by ELMs and that cause temporarily extreme recycling and power load conditions in the divertor. The radial width of the SOL during an ELM is even larger than in the L-mode. The time averaged power loss approaches the level of the input power, but the amount of missing power is higher than in other regimes. Detailed analyses seem to be impossible because the process is highly dynamic and shows obvious deviations from simple fluid behaviour. In addition, time averaged target plate calorimetry shows an approximate toroidal symmetry in the OH- and L-phases, but a pronounced toroidal asymmetry during ELM activity, making local ELM measurements questionable. This asymmetry also implies that ELMs always occur with roughly the same toroidal phase angle, probably as a consequence of mode locking to small resonant external magnetic field perturbations. In fact, a sideward shift or tilting of the divertor triplet coils within the mechanical tolerances of several millimetres already causes the formation of magnetic islands of several centimetres width at rational surfaces near the edge and ergodization around the separatrix. Except for the observed phase locking, there is as yet no clear indication of a direct influence of the edge perturbation on the H-mode physics.

After the L–H transition the power flow pattern changes. The power flux into the divertor chamber is reduced approximately to the OH-level; no satisfactory power accountability is possible. The energy confinement time increases after the L–H transition by a factor of about two. The linear current scaling of the energy confinement time remains during the H-phase; no clear dependence on B_t or $\bar{n}_e$ is observed. No power dependence of the energy confinement time is observed during the regular H-phase with ELMs. The analysis indicates that the lack of power dependence is due to a combination of power losses via ELMs, which decrease with increasing power, and via the intrinsic transport losses, which increase with increasing power. In the H-phase the energy confinement time increases linearly with the isotope mass.

The main results of the local transport analysis are that the electron heat diffusivity and the particle diffusion coefficient increase from the OH-phase to the L-phase and decrease after the L–H transition, changing typically by a factor of two in both cases. The L–H transition obviously starts near the plasma boundary, where the electron heat diffusivity and the diffusion coefficient are even more reduced than in the plasma centre. In ohmically heated and additionally heated plasmas with flat density profiles, having $\eta_i > 1$ over the entire plasma, the ion heat diffusivity is increased by a factor of two to four compared with the neoclassical values. This increase is in agreement with the theoretical expectations for η_i mode driven ion heat diffusivities. At high ion temperatures, convective losses have to be taken into account. Scaling relations for the diffusivities have been given and the parameters critical for the L–H transition have been identified and compared with theoretical models.

The operational range for the H-mode is large; however, it is necessary to have a density and a heating power above a certain threshold; i.e. $\bar{n}_e > 1.7 \times 10^{13}$ cm^{-3} and $P_{tot} > 1.1$ kW. The threshold conditions depend on the plasma configuration (for the DN configuration higher density and power are required than for the SN configuration) as well as on the drift direction of the ions (less power is required when it is towards the X-point) and on the ion species of the plasma and the beam. The power threshold shows a weak dependence on the density, the toroidal field and the current. A decisive factor for the development of the H-mode is the control of recycling gas. Backflow of molecular hydrogen out of the divertor chamber should be prevented. The H-mode can be achieved with ICRH in the minority mode, under lower hybrid (with NI) and beam current drive conditions, with additional pellet refuelling and, in the limiter configuration, with a bottom rail limiter.

Because of the L-phase preceding the transition and the existence of a power threshold, efforts to explore the mechanisms for the L–H transition have concentrated on parameters which are affected by auxiliary heating. There is experimental evidence that the electron temperature at the edge (or a related quantity such as pressure, resistivity or collisionality) plays an important role. Most convincing is the observation that the H-phase can be triggered by a sawtooth event. Detailed studies with good time resolution show that the L–H transition occurs when the thermal wave reaches the periphery.

At the L—H transition, an edge transport barrier develops which impedes the flow of particles and energy across the separatrix. The location of the steep gradients leads to the assumption that the edge barrier develops at the separatrix but inside of it.

At the instant of the L–H transition, the density fluctuation level at the edge suddenly decreases; the decrease of the bulk fluctuation amplitude proceeds more slowly. The confinement of runaway electrons also strongly increases at the L–H transition. The increased runaway losses in the L-phase are ascribed to the effects of resistive ballooning modes. The magnetic fluctuation level can decrease after the L–H transition. There are, however, a number of unexplained observations and no direct connection has been found so far between the magnetic turbulence as measured from the outside and the confinement properties of the bulk plasma.

The MHD stability of ASDEX H-mode discharges has been investigated with respect to both the linear and the non-linear evolution of ideal and resistive MHD stabilities as well as ideal and resistive ballooning modes, using free-boundary equilibria. The existence of pressure driven resistive modes at $\beta_p > 1$ may explain the fact that the $m \leq 5$ MHD modes observed in the H-mode have large inside-outside asymmetries of $\tilde{B}$, resonant surfaces close to the separatrix and m values increasing with beta. Because of the location of pressure and current gradients near the plasma edge it can be assumed that ELM instabilities are caused by pressure driven resistive modes with resonant surfaces near the separatrix but outside of it. These modes can lead to transport of plasma across the separatrix by kink-type motions so that energy and particles are transported to the divertor.

For calculations of ballooning mode stability on ASDEX, detailed informations on toroidal displacements of the magnetic surfaces and on local and global shear near the separatrix are needed. Ideal ballooning modes are not unstable even at the beta limit, where a sudden saturation of beta is followed by a slow decrease. During this decrease of beta there is a broad region of p'/p'_M values between 0.7 and 0.9. When the values of the pressure gradient p′ decrease, the current profile also becomes flat, which can be explained by the broadening of the T_e profile, by the increasing Z_{eff} (due to impurity accumulation) and by the effect of the bootstrap current. The growth rate of resistive ballooning modes strongly increases near the beta limit, and these modes may lead to the observed increased energy losses in this region. Compressibility and resistivity are the dominating destabilizing processes, depending on the mode number; overstable solutions are also observed. 'Electrostatic' ballooning modes are of similar importance near the plasma boundary of H-discharges, where the plasma pressure is small but p′ is large. Our calculations show that — despite the increased shear in this region — p′ is high enough for resistive ballooning modes to become unstable but it is far from the second region of stability.

Comparison of ASDEX results with those from other experiments, in particular those from DIII-D, shows agreement between them in many respects, for example the general occurrence of an L-phase before the L–H transition, the simultaneous improvement of the confinement times of energy and particles, the possibility of triggering the H-phase with a sawtooth, the development of a transport barrier at the separatrix but inside of it, the sharp reduction of the edge density fluctuation level and the importance of the ion grad-B drift direction. The H-mode is achieved in both limiter and divertor configurations and with various heating methods.

Compared with the ASDEX results, a stronger dependence of the power threshold on B_t and $\bar{n}_e$ is found on DIII-D, and a clear correlation between magnetic fluctuations and bulk plasma confinement is observed.

The comparison of experimental observations with theoretical models of the H-mode can only be qualitative. Theoretical explanations are needed for the suddenness of the L–H transition, to prove the simultaneous existence of two equilibrium states for the same set of external parameters and to explain the observed hysteresis in the L–H transition.

The general agreement on the location of the transport barrier — at the separatrix but inside of it — seems to rule out bifurcating solutions for the parallel transport in the SOL. The achievement of the H-mode in the limiter configuration seems to indicate that the increased shear in the edge region does not have a strong impact. The hypothesis that the L–H transition is triggered by the plasma edge entering the second stability regime seems to contradict the L-phase stability analysis. Even close to the L–H transition, the L-mode plasma is far from the first stability limit.

Theories based on mechanisms arising from the discontinuity between open and closed flux surfaces and plasma transport reproduce some salient H-mode features, such as the role of the ion grad-B drift direction, the suddenness of the transition and the observed hysteresis effects. In one of these theories the effect of a change in the radial electric field on turbulent transport is considered to reconcile the neoclassical transport effects with the observed sharp drop in the fluctuation amplitude.

Generally, the improvement of the bulk plasma confinement is connected with the reduction of free energy in the bulk plasma when the steep gradients are shifted to the edge region. The role of the modified plasma current profile has also been studied and it is found that the higher edge current density (due to the higher electrical conductivity and the bootstrap effect) provides better stability against current driven modes.

REFERENCES

[1] WAGNER, F., BECKER, G., BEHRINGER, K., et al., Phys. Rev. Lett. **49** (1982) 1408.

[2] WAGNER, F., BECKER, G., BEHRINGER, K., et al., in Plasma Physics and Controlled Nuclear Fusion Research 1982 (Proc. 9th Int. Conf. Baltimore, 1982), Vol. 1, IAEA, Vienna (1983) 43;
WAGNER, F., Confinement Studies on ASDEX, Rep. IPP-III/131, Max-Planck-Institut für Plasmaphysik, Garching (1988).

[3] KEILHACKER, M., BECKER, G., BERNHARDI, K., et al., Plasma Phys. Controll. Fusion **26** (1984) 49.

[4] GRUBER, O., JILGE, W., BERNHARDI, K., et al., in Controlled Fusion and Plasma Physics (Proc. 12th Eur. Conf. Budapest, 1985), Vol. 9F, Part I, European Physical Society (1985) 18.

[5] KAYE, S.M., BELL, M.G., BOL, H., BOYD, D., BRAU, K., J. Nucl. Mater. **121** (1984) 115.

[6] LUXON, J., ANDERSON, P., BATTY, F., et al., in Plasma Physics and Controlled Nuclear Fusion Research 1986 (Proc. 11th Int. Conf. Kyoto, 1986), Vol. 1, IAEA, Vienna (1987) 159.

[7] ODAJIMA, K., FUNAHASHI, A., HOSHINO, K., et al., ibid., p. 151.

[8] TANGA, A., BARTLETT, D.V., BEHRINGER, K., et al., ibid., p. 65.

[9] WAGNER, F., Confinement and β_p-Studies in Neutral Injection Heated ASDEX Plasmas, Rep. IPP-III/86, Max-Planck-Institut für Plasmaphysik, Garching (1983).

[10] BECKER, G., Nucl. Fusion **29** (1989) 1291.

[11] BURRELL, K.H., EJIMA, S., SCHISSEL, D.P., BROOKS, N.H., CALLES, R.W., Phys. Rev. Lett. **59** (1987) 432.

[12] KLÜBER, O., ZOHM, H., BRUHNS, H., et al., MHD Mode Structure and Propagation in the ASDEX Device, Rep. IPP-III/140, Max-Planck-Institut für Plasmaphysik, Garching (1989).

[13] TOI, K., GERNHARDT, J., KLÜBER, O., KORNHERR, M., Phys. Rev. Lett. **62** (1989) 430.

[14] KLÜBER, O., GERNHARDT, J., GRASSIE, K., et al., in Controlled Fusion and Plasma Heating (Proc. 13th Eur. Conf. Schliersee, 1986), Vol. 10C, Part I, European Physical Society (1986) 136.

[15] TROYON, F., GRUBER, R., SAURENMANN, H., et al., Plasma Phys. **26** (1984) 209.

[16] STAMBAUGH, R., GERNHARDT, J., KLÜBER, O., WAGNER, F., and the ASDEX Group, Investigations of MHD Activity in ASDEX Discharges, Rep. IPP-III/103, Max-Planck-Institut für Plasmaphysik, Garching (1985).

[17] VON GOELER, S., KLÜBER, O., FUSSMANN, G., GERNHARDT, J., KORNHERR, M., "MHD activity during ELMs", submitted to Nucl. Fusion.

[18] NEUHAUSER, J., CARLSON, A., FUSSMANN, G., HAAS, G., RAPP, H., TSOIS, N., and ASDEX Team, Bull. Am. Phys. Soc. **32** (1987) 1839;
NEUHAUSER, J., BESSENRODT-WEBERPALS, M., BRAAMS, B.J., et al., Tokamak edge modelling and comparison with experiment in ASDEX, submitted to Plasma Phys. Controll. Fusion.

[19] RAPP, H., NIEDERMEYER, H., KORNHERR, M., ASDEX Team, in Fusion Technology (Proc. 14th Symp. Avignon, 1986), Vol. 1, Pergamon Press, Oxford (1987) 595.

[20] KEILHACKER, M., FUSSMANN, G., GIERKE, G. von, et al., in Plasma Physics and Controlled Nuclear Fusion Research 1984 (Proc. 10th Int. Conf. London, 1984), Vol. 1, IAEA, Vienna (1985) 71.

[21] MÜLLER, R., JANESCHITZ, G., SMEULDERS, P., FUSSMANN, G., Nucl. Fusion **27** (1987) 1817.

[22] FUSSMANN, G., HOFMANN, J., JANESCHITZ, G., et al., J. Nucl. Mater. **162–164** (1989) 14.

[23] FUSSMANN, G., GRUBER, O., NIEDERMEYER, H., et al., in Plasma Physics and Controlled Nuclear Fusion Research 1988 (Proc. 12th Int. Conf. Nice, 1988), Vol. 1, IAEA, Vienna (1989) 145.

[24] LACKNER, K., DITTE, U., FUSSMANN, G., et al., in Plasma Physics and Controlled Nuclear Fusion Research 1984 (Proc. 10th Int. Conf. London, 1984), Vol. 1, IAEA, Vienna (1985) 319.

[25] McCORMICK, K., Rev. Sci. Instrum. **56** (1985) 1063.

[26] McCORMICK, K., PIETRZYK, Z.A., ASDEX Team and NI Team, J. Nucl. Mater. **162–164** (1989) 264.

[27] WAGNER, F., Variation of the Particle Confinement during Neutral Injection into ASDEX Divertor Plasmas, Rep. IPP-III/78, Max-Planck-Institut für Plasmaphysik, Garching (1982).

[28] TSOIS, N., HAAS, G., LENOCI, M., et al., Europhys. Conf. Abstr. **11D** (1987) 658.

[29] WÜRZ, H., BEIN, B.K., NEUHAUSER, J., et al., in Fusion Technology (Proc. 15th Symp. Utrecht, 1988), Vol. 1, Pergamon Press, Oxford (1989) 867.

[30] GOLDSTON, R.J., McCUNE, D.C., TOWNER, H.H., DAVIS, S.L., HAWRYLUK, R.J., SCHMIDT, G.L., J. Comput. Phys. **43** (1981) 61.

[31] BECKER, G., ASDEX Team, NI Team, Nucl. Fusion **22** (1982) 1589.

[32] BECKER, G., CAMPBELL, D., EBERHAGEN, A., et al., Nucl. Fusion **23** (1983) 1293.

[33] BECKER, G., Nucl. Fusion **24** (1984) 1364.

[34] GRUBER, O., JILGE, W., BERNHARDI, K., et al., in Controlled Fusion and Plasma Physics (Proc. 12th Eur. Conf Budapest, 1985), Vol. 9F, Part I, European Physical Society (1985) 18.

[35] GRUBER, O., JILGE, W., BOSCH, H.S., et al., in Controlled Fusion and Plasma Heating (Proc. 13th Eur. Conf. Schliersee, 1986), Vol. 10C, Part I, European Physical Society (1986) 248.

[36] LACKNER, K., GRUBER, O., GRASSIE, K., in Theory of Fusion Plasmas (Proc. Workshop Varenna, 1987), Editrice Compositori, Bologna (1987) 377.

[37] CHANG, C.S., HINTON, F.L., Phys. Fluids **25** (1982) 1493.

[38] GRUBER, O., BECKER, G., GIERKE, G. von, et al., in Plasma Physics and Controlled Nuclear Fusion Research 1986 (Proc. 11th Int. Conf. Kyoto, 1986), Vol. 1, IAEA, Vienna (1987) 357.

[39] GRUBER, O., FAHRBACH, H.U., GEHRE, O., et al., Plasma Phys. Controll. Fusion **30** (1988) 1611.

[40] WAGNER, F., FUSSMANN, G., GRAVE, T., et al., Phys. Rev. Lett. **53** (1984) 1453.

[41] BECKER, G., MURMANN, H., Nucl. Fusion **28** (1989) 2179.

[42] BECKER, G., ASDEX Team, NI Team, Local Energy and Particle Transport in Burst-free H-Phases of ASDEX, Rep. IPP-III/99, Max-Planck-Institut für Plasmaphysik, Garching (1984).

[43] BECKER, G., Nucl. Fusion **28** (1988) 1458.

[44] BECKER, G., Nucl. Fusion **27** (1987) 11.

[45] BECKER, G., Nucl. Fusion **26** (1986) 415.

[46] BECKER, G., in Basic Physical Processes of Toroidal Fusion Plasmas (Proc. Course and Workshop Varenna, 1985), Vol. 1, CEC, Luxembourg (1985) 217.

[47] BECKER, G., ASDEX Team, NI Team, Nucl. Fusion **28** (1988) 139.

[48] BECKER, G., GIERKE, G. von, KEILHACKER, M., et al., Nucl. Fusion **25** (1985) 705.

[49] BECKER, G., ASDEX Team, NI Team, Nucl. Fusion **27** (1987) 1785.

[50] STROTH, U., FAHRBACH, H.U., HERRMANN, W., MAYER, H.M., Nucl. Fusion **29** (1989) 761.

[51] KALLENBACH, A., MAYER, H.M., FUSSMANN, G., et al., Improvement of angular momentum confinement with density peaking on ASDEX, submitted to Nucl. Fusion.

[52] STÄBLER, A., WAGNER, F., BECKER, G., et al., in Heating in Toroidal Plasmas (Proc. 4th Int. Symp. Rome, 1984), Vol. 1, ENEA, Rome (1984) 3.

[53] GRUBER, O., in Plasma Physics (Proc. Int. Conf. Lausanne, 1984), Vol. 1, CEC, Brussels (1985) 67.

[54] SÖLDNER, F.X., MÜLLER, E.R., WAGNER, F., et al., Phys. Rev. Lett. **61** (1988) 1105.

[55] KAYE, S.M., GOLDSTON, R.J., Nucl. Fusion **25** (1985) 65.

[56] NIEDERMEYER, H., WAGNER, F., BECKER, G., et al., in Plasma Physics and Controlled Nuclear Fusion Research 1986 (Proc. 11th Int. Conf. Kyoto, 1986), Vol. 1, IAEA, Vienna (1987) 125.

[57] KEILHACKER, M., BISHOP, C.M., CORDEY, J.G., MUIR, D.G., WATKINS, M.L., in Controlled Fusion and Plasma Physics (Proc. 14th Eur. Conf. Madrid, 1987), Vol. 11D, Part III, European Physical Society (1987) 1339.

[58] WAGNER, F., GRUBER, O., GEHRE, O., LACKNER, K., MÜLLER, E.R., STAEBLER, A., in Controlled Fusion and Plasma Heating (Proc. 15th Eur. Conf. Dubrovnik, 1988), Vol. 12B, Part I, European Physical Society (1988) 207.

[59] GOLDSTON, R., Plasma Phys. Controll. Fusion **26** (1984) 87.

[60] KAYE, S.M., GOLDSTON, R., Nucl. Fusion **25** (1985) 65.

[61] TANGA, A., BARTLETT, D., BURES, M., et al., in Controlled Fusion and Plasma Heating (Proc. 15th Eur. Conf. Dubrovnik, 1988), Vol. 12B, Part I, European Physical Society (1988) 235.

[62] BURRELL, K.H., ALLEN, S.L., BRAMSON, G., et al., in Plasma Physics and Controlled Nuclear Fusion Research 1988 (Proc. 12th Int. Conf. Nice, 1988), Vol. 1, IAEA, Vienna (1989) 193.

[63] FONCK, R.J., BEIERSDORFER, P., BELL, M., et al., in Heating in Toroidal Plasmas (Proc. 4th Int. Symp. Rome, 1984), Vol. 1, ENEA, Rome (1984) 37.

[64] GRUBER, O., BECKER, G., GIERKE, G. von, et al., in Plasma Physics and Controlled Nuclear Fusion Resarch 1986 (Proc. 11th Int. Conf. Kyoto, 1986), Vol. 1, IAEA, Vienna (1987) 357.

[65] GIERKE, G. von, KEILHACKER, M., BARTIROMO, R., et al., in Controlled Fusion and Plasma Physics (Proc. 12th Eur. Conf. Budapest, 1985), Vol. 9F, Part I, European Physical Society (1985) 331.

[66] NIEDERMEYER, H., BECKER, G., BOMBA, B., et al., Plasma Phys. Controll. Fusion **30** (1988) 1443.

[67] STEINMETZ, K., NOTERDAEME, J.-M., WAGNER, F., et al., Phys. Rev. Lett. **58** (1987) 124.

[68] OGAWA, Y., HOFMEISTER, F., NOTERDAEME, J.-M., et al., in Controlled Fusion and Plasma Physics (Proc. 16th Eur. Conf. Venice, 1989), Vol. 13B, Part III, European Physical Society (1989) 1085.

[69] STEINMETZ, K., SÖLDNER, F.X., ECKHARTT, D., et al., in Plasma Physics and Controlled Nuclear Fusion Research 1986 (Proc. 11th Int. Conf. Kyoto, 1986), Vol. 1, IAEA, Vienna (1987) 461.

[70] LEUTERER, F., SÖLDNER, F.X., ECKHARTT, D., et al., Plasma Phys. Controll. Fusion **27** (1985) 1399.

[71] KAUFMANN, M., BÜCHL, K., FUSSMANN, G., et al., Nucl. Fusion **28** (1988) 827.

[72] WAGNER, F., KEILHACKER, M., ASDEX and NI Teams, J. Nucl. Mater. **121** (1984) 193.
WAGNER, F., In Basic Physical Processes of Toroidal Fusion Plasmas (Proc. Course and Workshop Varenna, 1985), Vol. 1, CEC, Luxembourg (1985) 65.

[73] EUBANK, H., GOLDSTON, R.J., ARUNASALAM, V., et al., in Plasma Physics and Controlled Nuclear Fusion Research 1978 (Proc. 7th Int. Conf. Innsbruck, 1978), Vol. 1, IAEA, Vienna (1979) 167.

[74] DODEL, G., HOLZHAUER, E., in Controlled Fusion and Plasma Heating (Proc. 15th Eur. Conf. Dubrovnik, 1988), Vol. 12B, Part I, European Physical Society (1988) 43.

[75] DODEL, G., HOLZHAUER, E., Annual Report 1987, Max-Planck-Institut für Plasmaphysik, Garching (1987).

[76] CROWLEY, T., MAZZUCATO, E., Nucl. Fusion **25** (1985) 507.

[77] RUDYJ, A., BENGTSON, R.D., CARLSON, A., et al., in Controlled Fusion and Plasma Physics (Proc. 16th Eur. Conf. Venice, 1989), Vol. 13B, Part I, European Physical Society (1989) 27.

[78] HOLLENSTEIN, C., KELLER, R., POCHELON, A., et al., Broadband Magnetic and Density Fluctuations in the TCA Tokamak, Rep. CRPP, LRP 306, Centre de recherches en physique des plasmas, Lausanne (1986).

[79] McGUIRE, K., ARUNASALAM, V., BELL, M.G., et al., Coherent and Turbulent Fluctuations in TFTR, Rep. PPPL-2435, Princeton Plasma Physics Laboratory, Princeton, NJ (1987).

[80] GIANNONE, L., Experimental Observations of Broadband Magnetic Fluctuations in ASDEX, Rep. IPP-III/138, Max-Planck-Institut für Plasmaphysik, Garching (1988).

[81] KIM, Y.J., GENTLE, K.W., RITZ, C.P., RHODES, T.L., BENGTSON, R.D., Nucl. Fusion **29** (1989) 99.

[82] DODEL, G., HOLZHAUER, E., MASSIG, J., in Controlled Fusion and Plasma Physics (Proc. 14th Eur. Conf. Madrid, 1987), Vol. 11D, Part I, European Physical Society (1987) 249.

[83] KWON, O.J., DIAMOND, P.H., WAGNER, F., et al., Nucl. Fusion **28** (1988) 1931.

[84] LEE, J.K., Nucl. Fusion **26** (1986) 955.

[85] McGUIRE, K., BEIERSDORFER, P., BELL, M., et al., in Plasma Physics and Controlled Nuclear Fusion Research 1984 (Proc. 10th Int. Conf. London, 1984), Vol. 1, IAEA, Vienna (1985) 117.

[86] KEILHACKER, M., GIERKE, G. von, MÜLLER, E.R., et al., Plasma Phys. Controll. Fusion **28** (1986) 29.

[87] GRASSIE, K., BECKER, G., GRUBER, O., et al., in Turbulence and Anomalous Transport in Magnetized Plasmas (Proc. Int. Workshop, Cargese, 1986), Editions de Physique, Orsay (1987) 279.

[88] GRASSIE, K., GRUBER, O., KLÜBER, O., et al., in Controlled Fusion and Plasma Physics (Proc. 14th Eur. Conf. Madrid, 1987), Vol. 11D, Part I, European Physical Society (1987) 226.

[89] JAKOBY, A., Non-Linear Resistive MHD-Code in Cylindrical Geometry, Rep. IPP-6/269, Max-Planck-Institut für Plasmaphysik, Garching (1987).

[90] CONNOR, J.W., HASTIE, R.J., TAYLOR, J.B., Phys. Rev. Lett. **40** (1987) 396.

[91] CHOE, W.H., FREIDBERG, J.P., Phys. Fluids **29** (1986) 1766.

[92] NEUHAUSER, J., SCHNEIDER, W., WUNDERLICH, R., Nucl. Fusion **26** (1986) 1679.

[93] CONNOR, J.W., HASTIE, R.J., MARTIN, T.J., Plasma Phys. Controll. Fusion **27** (1985) 1509.

[94] CORREA-RESTREPO, D., Z. Naturforsch., A **37** (1982) 848.

[95] ZEHRFELD, H.P., GRASSIE, K., Nucl. Fusion **28** (1988) 891.

[96] GRASSIE, K., ZEHRFELD, H.P., Nucl. Fusion **28** (1988) 899.

[97] CONNOR, J.W., HASTIE, R.J., MARTIN, T.J., SYKES, A., TURNER, M.F., in Plasma Physics and Controlled Nuclear Fusion Research 1982 (Proc. 9th Int. Conf. Baltimore, 1982), Vol. 3, IAEA, Vienna (1983) 403.

[98] DRAKE, J.F., ANTONSEN, T.M., Phys. Fluids **28** (1985) 544.

[99] HENDER, T.C., CARRERAS, B.R., COOPER, W.A., et al., Phys. Fluids **27** (1984) 1439.

[100] OKABAYASHI, M., ASAKURA, N., BELL, R., et al., in Plasma Physics and Controlled Nuclear Fusion Research 1988 (Proc. 12th Int. Conf. Nice, 1988), Vol. 1, IAEA, Vienna (1989) 97.

[101] MANICKAM, J., ARUNASALAM, V., BARNES, C.W., et al., ibid., p. 395.

[102] SCHISSEL, R., in Controlled Fusion and Plasma Physics (Proc. 16th Eur. Conf. Venice, 1989), Vol. 13B, Part I, European Physical Society (1989) 115.

[103] TOI, K., ADATI, K., AKIYAMA, R., et al., ibid., p. 221.

[104] STRACHAN, J.D., BITTER, M., RAMSEY, A.T., et al., Phys. Rev. Lett. **58** (1987) 1004.

[105] GEHRE, O., GRUBER, O., MURMANN, H.D., et al., Phys. Rev. Lett. **60** (1988) 1502.

[106] KEILHACKER, M., Plasma Phys. Controll. Fusion **29** (1987) 1401.

[107] LOHR, J., STALLARD, B.W., PRATER, R., et al., Phys. Rev. Lett. **60** (1988) 2630.

[108] OHKAWA, T., CHU, M.S., HINTON, F.L., LIU, C.S., LEE, Y.C., Phys. Rev. Lett. **51** (1983) 2101.

[109] HOSHINO, K., YAMAMOTO, T., KAWASHIMA, H., YAMANCHI, T., UESUGI, Y., J. Phys. Soc. Jpn. **56** (1987) 1750.

[110] SUGIHARA, M., SAITO, S., HITOKI, S., et al., J. Nucl. Mater. **128&129** (1984) 114.

[111] SINGER, C.E., REDI, M.H., BOYD, D.A., et al., Nucl. Fusion **25** (1985) 1555.

[112] SHIMADA, M., Bull. Am. Phys. Soc. **32** (1987) 1898.

[113] BISHOP, C.M., KIRBY, P., CONNOR, J.W., HASTIE, R.J., TAYLOR, J.B., Nucl. Fusion **24** (1984) 1579.

[114] BISHOP, C.M., Nucl. Fusion **26** (1986) 1063.

[115] BISHOP, C.M., in Theory of Fusion Plasmas (Proc. Workshop Lausanne, 1988), Editrice Compositori, Bologna (1988) 123.

[116] HAHM, T.S., DIAMOND, P.H., Phys. Fluids **30** (1987) 133.

[117] BURRELL, K.H., ALLEN, S.L., BRAMSON, G., et al., in Plasma Physics and Controlled Nucler Fusion Research 1988 (Proc. 12th Int. Conf. Nice, 1988), Vol. 1, IAEA, Vienna (1989) 193.

[118] CALLEN, J.D., QU, W.X., SIEBERT, K.D., et al., in Plasma Physics and Controlled Nuclear Fusion Research 1986 (Proc. 11th Int. Conf. Kyoto, 1986), Vol. 2, IAEA, Vienna (1987) 157.

[119] WAGNER, F., BARTIROMO, R., BECKER, G., et al., Nucl. Fusion **25** (1985) 1490.

[120] HINTON, F.L., Nucl. Fusion **25** (1985) 1457.

[121] HINTON, F.L., STAEBLER, G.M., in Plasma Physics and Controlled Nuclear Fusion Research 1988 (Proc. 12th Int. Conf. Nice, 1988), Vol. 2, IAEA, Vienna (1989) 327.

[122] ITOH, S.-I., ITOH, K., Phys. Rev. Lett. **60** (1988) 2276.

[123] BURRELL, K.H., "Physics of enhanced confinement, H-mode discharges in DIII-D", presented at Workshop on Enhanced Confinement Regimes, Nice, 1988.

[124] SHAING, K.C., LEE, G.S., CARRERAS, B.A., HOULBERG, W.A., CRUME, E.C., Jr., in Plasma Physics and Controlled Nuclear Fusion Research 1988 (Proc. 12th Int. Conf. Nice, 1988), Vol. 2, IAEA, Vienna (1989) 13.

[125] PERKINS, F.W., in Heating in Toroidal Plasmas (Proc. 4th Int. Symp. Rome 1984), Vol. 2, ENEA, Rome (1984) 977.

[126] DOMINGUEZ, R.R., WALTZ, R.E., Nucl. Fusion **27** (1987) 65.

[127] MATTOR, N., DIAMOND, P.H., Phys. Fluids **3** (1988) 1180.

[128] DOMINGUEZ, R.R., WALTZ, R.E., Phys. Fluids **31** (1988) 3147.

[129] ROMANELLI, F., Plasma Phys. Controll. Fusion **31** (1989) 1535.

[130] FURTH, H., Plasma Phys. Controll. Fusion **28** (1986) 1305.

[131] SHEFFIELD, J., Nucl. Fusion **29** (1989) 1347.

(Manuscript received 21 August 1988
Final manuscript received 21 July 1989).